

Characterization of Sensors for CMS Phase II Forward Pixel Detector

by

Wilber Ortiz Lago

A thesis submitted in partial fulfillment of the requirements for the degree of

MASTER OF SCIENCE

in

PHYSICS

UNIVERSITY OF PUERTO RICO

MAYAGÜEZ CAMPUS

2018

Approved by:

Juan Eduardo Ramírez, Ph.D.
President, Graduate Committee

Date

Sudhir Malik, Ph.D.
Co-President, Graduate Committee

Date

Ángel M. López, Ph.D.
Member, Graduate Committee

Date

Samuél Santana Colón, Ph.D.
Member, Graduate Committee

Date

Rocío Zapata Medina, MA.
Representative of Graduate Studies

Date

Rafael A. Rámos, Ph.D.
Chairperson of the Department

Date

ABSTRACT

The HL-LHC conditions of instantaneous peak luminosities up to $7.5 * 10^{34} cm^{-2} s^{-1}$ and an integrated luminosity of the order of $300 fb^{-1}/year$ would result in 1 MeV neutron equivalent fluence of $2.3 * 10^{16} n_{eq}/cm^2$ and a total ionizing dose (TID) of 12MGy (1.2 Grad) at the center of CMS, where its innermost component, the Phase-2 Pixel Detector will be installed. The detector should survive the above radiation dose, handle projected hit rates of $3GHz/cm^2$ at lowest radius, be able to separate and identify particles in extremely dense collision debris, deal with a pileup of 140-200 collisions per bunch crossing and have high impact parameter resolution. This along with physics goals translates into requiring a detector design that is more highly granular, has thinner sensors and smaller pixels, and a faster and radiation hard electronics. Sensors of planar type with pixel sizes six times smaller than currently used and 3D pixel types are being proposed to handle the above scenario. 3D sensors offer several improvements compared to the planar sensors like faster charge collection, radiation hard, lower depletion voltage but have higher noise (lower signal to noise ratio). Thin sensors yield smaller signals but offer less material budget. The work presented is based on the test-beam program at Fermilab designed to test sensors for the Phase-2 Pixel Detector. These sensors are bump bonded to PSI46dig readout chip (used currently with Phase-1 Detector) as these are the only ones available at the time of studies. The sensors are tested with a $120 GeV/c$ proton beam at the Fermilab Meson Test-Beam Facility with a telescope made of eight planes of pixel modules to reconstruct tracks of the charged particles passing through the sensors tested (referred to as Detector Under Test (DUT)).

RESUMEN

Las condiciones de la Alta Luminosidad del Gran Colisionador de Hadrones (HL-LHC, por sus siglas en inglés) de luminosidades máximas instantáneas de hasta $7.5 * 10^{34} cm^{-2} s^{-1}$ y una luminosidad integrada del orden de $300 fb^{-1}/año$ daría como resultado una fluencia equivalentes de neutrones de $1 MeV$ de $2.3 * 10^{16} n_{eq}/cm^2$ y una dosis total de ionización (TID, por sus siglas en inglés) de $12 MGy$ ($1.2 Grad$) sobre la parte central del solenoide de muón compacto (CMS, por sus siglas en inglés), donde se instalará los componentes más internos del detector de pixeles de la fase-2. El detector debería ser capaz de resistir a la dosis de radiación anterior, aguantar la razón de golpes proyectadas de $3 GHz/cm^2$ en el radio más inferior, ser capaz de separar e identificar partículas en colisiones extremadamente densas, tratar con una cantidad de 140-200 colisiones por cruce de grupo y que tenga una resolución de parámetro de alto impacto. Esto en base a los objetivos de la física se traduce en la necesidad de que el diseño del detector sea más granular, tenga sensores más delgados y pixeles más pequeños, y una electrónica más rápida y resistente a la radiación. Los sensores de tipo planar con tamaño de pixeles seis veces más pequeños que los actualmente utilizados y los tipos de pixeles 3D que se están proponiendo para encargarse del escenario anterior. Los sensores 3D ofrecen varias mejoras en comparación con los sensores planares, como en la recolección de carga más rápida, resistencia a la alta radiación, menor tensión de agotamiento pero un mayor nivel de ruido (menor relación señal/ruido). Los sensores delgados generan señales más pequeñas pero requieren de menor presupuesto del material. El trabajo presentado se basa en el programa de haz de prueba en Fermilab diseñado para probar sensores para la fase-2 del detector de pixeles. Estos sensores están conectados al chip de lectura digital PSI46dig (actualmente están siendo utilizados en el detector de la fase 1) ya que son los únicos disponibles en éstos momentos de los estudios. Los sensores se prueban a $120 GeV/c$ en el haz de protones en *Fermilab Meson Test-Beam Facility* con un telescopio compuesto por ocho planos de módulos de pixeles para reconstruir las trayectorias de las partículas cargadas que pasan a través de los detectores bajo prueba (DUT, en sus siglas en inglés).

Copyright © 2018

by

Wilber Ortiz Lago

To everybody, who inspired me everyday.

ACKNOWLEDGMENTS

This work is dedicated to God, my parents Epifania Lago and Pascual Ortiz, and my sisters and brothers who always motivated me at every moment so that I can achieve my goals for this project in the field of physics.

I also thank my thesis advisor and co-advisor, Dr. Juan Eduardo Ramirez and Dr. Sudhir Malik, as well as a member of my thesis committee, Dr. Ángel López for sharing their knowledge and experiences in the complex field of high energy physics. I would also like to thank Dr. Scarlet Norberg for always helping me in very challenging situations, when I started my first experience at Fermilab. Despite the difficulties in our language communications, she always kept her interest in my work. Thanks to them, this research about Characterization of Sensor for CMS Phase II Forward Pixel Detector has been made a reality.

I would also like to thank Dr. Caterina Vernier and Dr. Lorenzo Uplegger for allowing me to be part of their research group in the CMS Phase-2 Pixel Detector upgrade project and the opportunity to share experience at the test-beam telescope at Fermi National Accelerator Laboratory. I would also like to extend my heartfelt gratitude to Irene Zoi, PhD student (University of Florence, Italy) for always answering my questions that helped clear all my doubts about the research.

“I would like to thank National Science Foundation (NSF Award ID 1506168) for supporting my several trips to Fermilab to work on test-beam and collect data for the work presented here”.

Finally, I am happy about the experience in the development of this topic, it has been a great joy and satisfaction to share a unique experience in the field of Pixel Detectors.

TABLE OF CONTENTS

| | <u>Pages</u> |
|---|--------------|
| ABSTRACT | ii |
| RESUMEN..... | iii |
| ACKNOWLEDGMENTS | vi |
| LIST OF FIGURES | ix |
| Introduction..... | 1 |
| 1.1 The Large Hadron Collider (LHC) | 2 |
| 1.2 Physics Beyond Standard Model | 3 |
| 1.2.1 Discovery of Higgs Boson | 3 |
| 1.2.2 Supersymmetry Searches | 4 |
| 1.2.3 Dark Matter | 5 |
| 1.3 The LHC proton beam | 6 |
| 1.4 CMS Experiment..... | 7 |
| 1.4.1 CMS Detector | 8 |
| 1.4.2 Magnet | 9 |
| 1.4.3 Muon System | 9 |
| 1.4.4 Calorimeter..... | 10 |
| 1.4.5 Tracker | 11 |
| Previous Work..... | 14 |
| 2.1 The Phase-0 Pixel Detector | 14 |
| 2.1.1 Sensor and Readout Chip..... | 16 |
| 2.1.2 The detector layout..... | 18 |
| 2.2 Phase-1 upgrade of Pixel Detector | 19 |
| 2.2.1 Sensor and Readout Chip..... | 22 |
| Objectives (Current Work)..... | 27 |
| 3.1 Requirements for the Phase-2 Pixel Detector | 28 |
| 3.2 Detector Layout..... | 30 |
| 3.2.1 The Pixel modules..... | 31 |
| 3.2.2 Pixel sensor | 32 |
| 3.2.3 3D Sensors studied for characterization..... | 36 |

| | |
|---|----|
| Semiconductor detectors | 39 |
| 4.1 Silicon | 39 |
| 4.2 Thermal energy | 39 |
| 4.2.1 Energy band model | 40 |
| 4.3 The <i>pn</i> -junction | 42 |
| 4.4 Charged particle interaction with silicon | 48 |
| 4.5 Working Principle of an AC – coupled silicon as a Tracking Device | 51 |
| 4.6 Radiation Damage in Silicon Detector Devices..... | 52 |
| Material and Methods | 54 |
| 5.1 Silicon Pixel Telescope | 55 |
| 5.2 Data Acquisition Apparatus | 57 |
| 5.3 Tracking Software..... | 58 |
| 5.3.1 Track reconstruction..... | 59 |
| 5.3.2 Alignment Procedure and Results | 61 |
| Test beam results..... | 68 |
| 6.1 Sensor efficiency..... | 68 |
| 6.2 Cell efficiency | 70 |
| 6.3 Charge collection | 72 |
| 6.4 Cluster size | 74 |
| 6.5 Spatial Resolution | 75 |
| Conclusions..... | 79 |
| References..... | 81 |

LIST OF FIGURES

| | |
|--|----|
| Figure 1.1: It is shown four main detectors that are 100 metres below the ground at the CERN on the French-Swiss border, north of Geneva. | 2 |
| Figure 1.2: CMS, ATLAS, ALICE and LHCb detectors are shown. These are located around 27 kilometers in circumference. The beams of particles formed by protons or lead ions are moved through a succession of machines as: Linac 2, Linac 3, PS, PSB, SPS, etc. | 7 |
| Figure 1.3: The CMS detector at the LHC designed to study proton – proton (pp) collision. | 8 |
| Figure 1.4: The schematic r - z-view of one quarter of the silicon strip tracker is shown. Single sided silicon modules are indicated in red (solid lines) while double sided modules is shown in blue (dashed lines). | 12 |
| | |
| Figure 2.1: The phase 0 of the pixel detector with 3 barrel layers and 4 disks. | 15 |
| Figure 2.2: Forward and Barrel pixel sensor of the CMS detector. | 16 |
| Figure 2.3: The silicon sensor and readout chip of CMS pixel detector-phase 0. | 17 |
| Figure 2.4: Pixel tracking performance measurements from 2010 and 2011 data. Left: Average module hit efficiency per layer/disk in the pixel detector once modules excluded from the readout are excluded from the measurement. Right: Average module hit efficiency as a function of the instantaneous luminosity. | 18 |
| Figure 2.5: Cluster charge distribution in the barrel pixel detector normalized to a 285 μ m path in silicon. The distribution shows the Landau like shape and peaks at about 21000 electrons as expected for full charge collection. | 19 |
| Figure 2.6: Performance of the Phase-0 pixel detector in simulated tt events: a) efficiency; b) fake rate. | 21 |
| Figure 2.7: Performance of the phase-1 Pixel detector in simulated tt events: a) efficiency, b) fake rate. Results are shown for the upgraded pixel detector with zero pile-up (blue squares), an average pile-up of 25 (red dots), an average pile-up of 50 (black diamonds), and an average pile-up of 100 (magenta triangles). | 21 |
| Figure 2.8: The amount of material in the pixel detector shown in units of radiation length (left), and in units of nuclear interaction length (right) as a function of η is given for the Phase-0 (green histogram), and the Phase-1 upgrade detector (black point). The shaded region at high $ \eta $ is outside the region for track reconstruction. | 22 |
| Figure 2.9: A comparison of layout of Phase-1 and Phase-0 Pixel Detector Layout. | 23 |
| Figure 2.10: The pixel module for the CMS phase I upgrade. All the surface components are mounted at Fermilab (FNAL) at the Silicon Detector Laboratory (SiDet). | 24 |
| Figure 2.11: The upgrade detector of the 3 disks of FPIX module construction. | 25 |
| Figure 2.12: The bump bonded between sensor and electronic chip are illustrated. | 25 |
| Figure 2.13: The pixel unit cell (PUC) of the ROC and the chip pixel cell. | 26 |

| | |
|--|----|
| Figure 3.1: Integrated particle fluence in 1MeV neutron equivalent per cm^2 , for the Phase-2 tracker. The estimates shown correspond of pp collisions $s = 14TeV$ and to a total integrated luminosity of $3000 fb^{-1}$ | 28 |
| Figure 3.2: Sketch of one quarter of the pixel detector layout in the r-z view. Green lines correspond to modules made of two readout chips and orange lines represent larger modules with four chips. | 29 |
| Figure 3.3: Phase-2 Pixel Detector Layout is shown. | 30 |
| Figure 3.4: a) 1x2 pixel modules, b) 2 x 2 pixel modules for the barrel configuration. . | 31 |
| Figure 3.5: Drawing of two adjacent pixel cells for sensors from the HPK submission with pixel size $25 \times 100 mm^2$ (left) and $50 \times 50 mm^2$ (right). The n+ implants are shown in green, the metal layers in blue, the p-stop areas in red, the contacts in orange, and the bump bond pads in purple. | 33 |
| Figure 3.6: In 3D sensor process deep holes are etched into the silicon to achieve holes, these are used as electrodes to span the depletion zone in the horizontal, instead of the standard vertical one. The electrons and holes are moved shorter, which means they are less sensitive to trapping. | 34 |
| Figure 3.7: A schematic illustration between planar and 3D sensors, where $L = 130 \mu m$ is the active thickness and $d \approx 50 \mu m$ is the collection distance. | 35 |
| Figure 3.8: Shows the manufacturing details of layout of 3D sensor produced using “6” Si-Si wafer. | 36 |
| Figure 3.9: The columnar implant n+ and p+ are illustrated both signal and field. | 37 |
| Figure 3.10: 2E and 3E module types of standard size with cluster size of 2 and 3. | 37 |
| Figure 3.11: 3D Pixel First Batch Wafer Layout. | 38 |
| | |
| Figure 4.1: Schematic representation of Si bonds a) T=0K, b) thermal generation of electron-hole | 39 |
| Figure 4.2: The valence band and conduction band separated by the energy gap (E_g). . | 40 |
| Figure 4.3: The p- and n-type unions with the energy levels of conduction and valence | 43 |
| Figure 4.4: The mathematical representations of the semiconductor material under the equilibrium state. There is no external voltage. | 45 |
| Figure 4.5: The polarity in the potential barrier of the pn -junction. | 46 |
| Figure 4.6: Behavior of the electric field in the bulk silicon. The strips and the backplane are on Ground potential and on high voltage potential. | 47 |
| Figure 4.7: The plot shows the current-voltage for a silicon diode in the reverse bias directions. The expanded view between 0 to 100 V shows that $I \propto V$, while from 0 to 500 V shows the full scan and the breakdown at high voltage. | 48 |
| Figure 4.8: The average stopping power $\langle dE/dx \rangle$ for muons traversing on copper material is shown; likewise, the correction to the Bethe-Bloch formula is illustrated. Therefore, it can be said that is the general principle of all ionizing detectors. | 49 |
| Figure 4.9: The Landau distribution for an ionized charge over $500 \mu m$ silicon from a cosmic particle (\sim MIP) arriving at an incident angle with 3.8 T magnetic field. | 50 |
| Figure 4.10: The working principle of an AC-coupled silicon microstrip detector. The holes are collected by $p +$ strips implants in a $n - bulk$ silicon. | 51 |
| Figure 4.11: Displacements in silicon lattice after collision with traversing particles. ... | 52 |

| | |
|--|----|
| Figure 5.1: 3-dimensional schematic of the pixel telescope. | 55 |
| Figure 5.2: The experimental set up at Fermilab. | 56 |
| Figure 5.3: The telescope readout system based on CAPTAN hardware. | 57 |
| Figure 5.4: Data visualization the telescope. | 58 |
| Figure 5.5: Graphical User Interface (GUI) of Monicelli. The left top shows all the components that allows all alignment operations while on the right side shows a histogram navigator used to view the different control histograms created during the alignment phases. | 59 |
| Figure 5.6: Beam spot on 2x4 detector plane of the telescope..... | 60 |
| Figure 5.7: The picture below shows the geometrical arrangement of the considered clusters (1, 2, 2x2 pixels). | 61 |
| Figure 5.8: The x and y residual distributions of the telescope detector after having obtained a good alignment are shown. a) A narrow shape along the tilted that corresponds to a pitch of $100 \mu m$. b) A non-Gaussian shape along the non-tilted coordinate for a pitch of $150 \mu m$ | 64 |
| Figure 5.9: The x and y pull distributions for one station and plane of the telescope detectors. | 64 |
| Figure 5.10: It is illustrated for one of the telescope detector the correlation between unconstrained residuals and impact point coordinate in one of the telescope detector. ... | 65 |
| Figure 5.11: χ^2/DoF distribution after performing a complete alignment. | 66 |
| Figure 5.12: The plots show the slope distribution of the 120 GeV proton tracks for a small angular dispersion ($\sim 10 - 4 rad$). | 66 |
| Figure 5.13: It is illustrated the error distribution on track fit at DUT Z position after performing alignment. The discrete peaks are due to the combinations of different hit resolution which may be associated to the tracks. | 67 |
| | |
| Figure 6.1: The efficiency map of 56D (Dut0, efficiency 99.43%) and 56B (Dut1, efficiency 99.42%) sensors at a 0-degree rotation angle and a bias voltage of 10V..... | 69 |
| Figure 6.2: Sensor efficiency as a function of the bias voltage at 0-degree rotation. | 70 |
| Figure 6.3: Cell efficiency: Top is 56D (3E) and Bottom is 56B(2E) sensors, both at 0-degrees and bias voltage of 20V. | 71 |
| Figure 6.4: A three-dimensional view cell efficiency for the 56D (3E). | 72 |
| Figure 6.5: Cell efficiencies of 56D (3E) and 56B (2E) sensors at 5-degree rotation. | 72 |
| Figure 6.6: The charge distribution for the 56D (3E) and 56B (2E) sensors are shown. The bias voltage for both distributions is 40V and the 0-degree rotation angle. | 73 |
| Figure 6.7: The cluster size distribution at 0-degree rotation angle and bias voltage of 10V..... | 74 |
| Figure 6.8: "Cluster size vs. angle for a bias voltage of 30V"..... | 75 |
| Figure 6. 9: Y residual cluster size 1 for 56D(3E). | 76 |
| Figure 6. 10: X residual cluster size of 2: Left is 56D (3E) and right is 56B (2E). | 77 |
| Figure 6.11: Y residual cluster size of 2: Left is 56D (3E) and right is 56B (2E). | 77 |

Chapter 1

Introduction

Physics is considered mother of all sciences and encompasses the study of the structure of matter and the interactions between the fundamental constituents of the observable universe at both, macroscopic and submicroscopic levels. It reflects human curiosity to find a unified set of laws governing matter, motion, and energy at all levels: small subatomic distances, human scale of everyday life, and out to the largest distances (galactic scale).

Particle physics is a branch of physics that studies elementary constituents of matter and radiation, and the interactions between them. It aims to answer the fundamental questions of the nature of mass, energy, and matter, and their relations to the cosmological history of the Universe. All the particles and their interactions observed to date can be described by a theory called the Standard Model which is a combination of Quantum Mechanics and Special Theory of Relativity. The Standard Model has 40 types of elementary particles [1] divided into two main categories: fermions (quarks, leptons, antiquarks, and antileptons), which generally are "matter particles" and "antimatter particles", and bosons (gauge bosons and the Higgs boson [2]), which generally are "force particles" that mediate interactions among fermions. A particle containing two or more elementary particles is a composite particle. The fundamental forces [3] causing interactions between them are: Electromagnetic, Strong, Weak, and Gravitational.

Particle Physics is also called "High Energy Physics (HEP)", since most elementary particles do not occur under normal circumstances in nature, but can be created and detected during energetic collisions of other particles, as is done in particle accelerators like at Large Hadron Collider (LHC) at CERN which is trying to find answers to questions like origin of mass, neutrino oscillations, matter–antimatter asymmetry, and the nature of dark matter and dark energy.

1.1 The Large Hadron Collider (LHC)

The LHC [4] is the most powerful accelerator in the world. It accelerates two proton beams each up to an energy 7 TeV. The proton beams travel in opposite directions in separate beam pipes, which are maintained at ultrahigh vacuum. The two proton beams travel close to the speed of light accelerated in a 27-kilometer-long tunnel lined up with a ring of superconducting magnets that accelerate and guide the beams of particles along the ring. The tunnel is 100 meters below the ground situated at the Conseil Européen pour la Recherche Nucléaire (CERN) or also known as European Organization for Nuclear Research on the French-Swiss border, north of Geneva. The superconducting magnets conduct the electricity without resistance or loss of energy, so it is required to keep these cold at a temperature of liquid helium: -271.3°C . For this reason, the accelerator is connected to a distribution system of liquid helium.

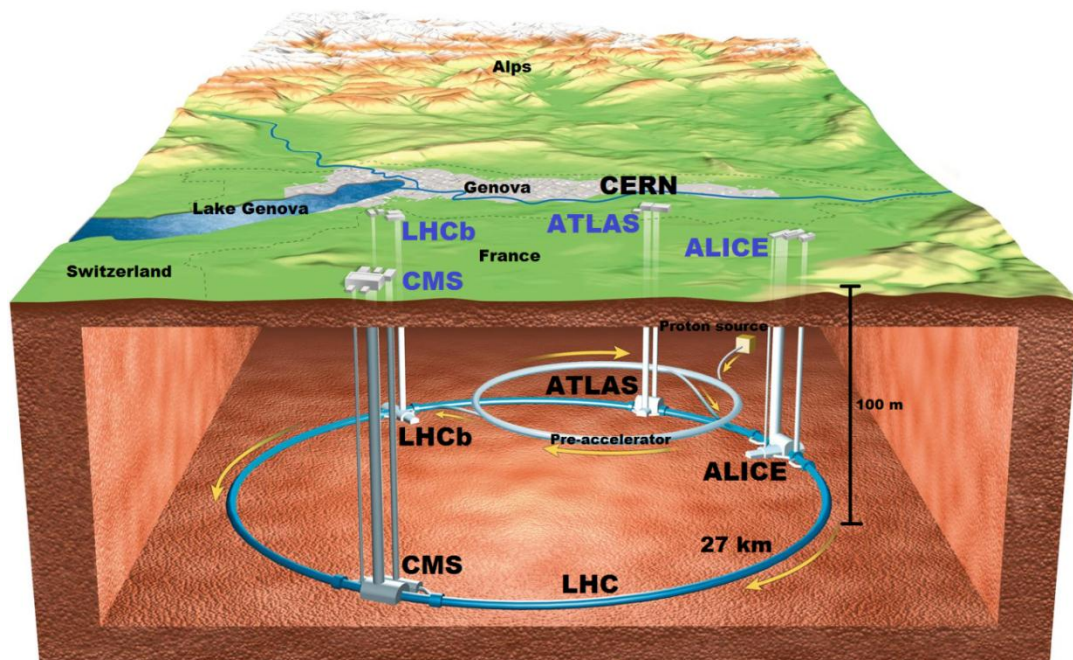


Figure 1.1: It is shown four main detectors that are 100 metres below the ground at the CERN on the French-Swiss border, north of Geneva.

Seven detectors have been constructed at the LHC, which are ATLAS, Compact Muon Solenoid (CMS), ALICE, LHC beauty-quark (LHCb), Total Cross Section, Elastic Scattering and Diffraction Dissociation (TOTEM), Monopole and Exotics Detector at the LHC (MoDEL) and LHC-forward (LHCf). The first four are the main detectors, placed around the interaction points along the LHC ring, shown in Figure 1.1. The CMS and ATLAS are both built to search and study the Higgs boson and new Physics **Beyond the Standard Model** but have different features; while ALICE is studying a fluid form of matter called quark-gluon plasma that existed shortly after the Big Bang. TOTEM, MoDEL and LHCf are very much smaller and are for very specialized research.

1.2 Physics Beyond Standard Model

Standard Model is not the ultimate theory of elementary particles and their interactions. Though it agrees very well with experimental observations, many important questions remain unanswered: What is the origin of particle masses and are they due to a Higgs boson? How does one understand the number of species of matter particles and how do they mix? What is the origin of the difference between matter and antimatter, and is it related to the origin of the matter in the Universe? What does the dark matter consist of [5]? How does one unify the fundamental interactions? How does one quantize gravity [6]? The Physics Beyond Standard Model (BSM) refers to the development of a set of new theories to answer the above deficiencies of the Standard Model. Some of the popular ones are: Supersymmetry, Composite Higgs, Extra Dimensions, Hidden Valley, String Theory.

1.2.1 Discovery of Higgs Boson

One of the major components of the Standard Model framework is the quantum field, called Higgs field, which is supposed to be responsible for giving mass to fundamental particles. All quantum fields have a fundamental particle associated with them. The particle associated with the Higgs field is called the Higgs boson. In 1964, three groups

of researchers independently published papers showing that conditions for electroweak symmetry would be "broken" if an unusual type of field existed throughout the universe and result in some fundamental particles acquiring mass. The field required for this to happen is called Higgs field (after Peter Higgs, one of the theory proponents) and the mechanism by which it led to symmetry breaking, is known as the Brout-Englert-Higgs mechanism. A key feature of the necessary field is that it would take less energy for the field to have a non-zero value than a zero value, unlike all other known fields, therefore, the Higgs field has a non-zero value (or vacuum expectation) everywhere.

On 4 July 2012, the ATLAS and CMS experiments at CERN's Large Hadron Collider announced the observation of a new particle in the mass region around 125 GeV. This particle is consistent with the Higgs boson predicted by the Standard Model. Consequently, the Nobel Prize in Physics 2013 was awarded jointly to François Englert and Peter W. Higgs based on discovery by the ATLAS and CMS experiments. Other types of Higgs bosons are predicted by other theories that go beyond the Standard Model. The Pixel Detector due to its highly granular nature and ability to identify vertices close to the interaction point play a central role in identifying the decay processes that lead to the detection of Higgs boson.

1.2.2 Supersymmetry Searches

After the discovery of a boson with properties consistent with the SM Higgs at the LHC attention has shifted to searches for new physics to explain the fine-tuned cancellation of large quantum corrections required to stabilize the Higgs boson at a light mass of 125 GeV. Supersymmetry (SUSY) is a new symmetry beyond the SM that provides a suitable and elegant mechanism to mitigate this hierarchy problem. SUSY proposes a super-partner for each SM particle with the same quantum numbers except for spin, which differs by a half-integer unit. The loop corrections to the Higgs boson mass due to these sparticles are opposite in sign to those of the SM particles predicting a finite value for the Higgs boson mass. This behavior can survive the breaking of SUSY, which is necessary to explain the non-observation of superpartners with the same mass as their SM counterparts, provided that the superpartners are not themselves too heavy.

In addition to solving the problem of radiative stability, some SUSY models are attractive since they also offer a dark matter candidate to explain astrophysical observations. So far, no evidence has been found but with new techniques of deep learning and possible future innovative techniques to reduce background and improving b-quark and top quark tagging especially for boosted heavy objects with Phase-2 Pixel Detector, we may hope to discover SUSY in coming years at the LHC.

1.2.3 Dark Matter

Our universe is made of 68% Dark Energy, 27 % Dark Matter and the rest - everything on Earth, everything ever observed with all our instruments, all normal matter - adds up to less than 5%. Unlike the matter we know, Dark Matter has never been directly observed because it does not emit or interact with electromagnetic radiation, which makes it invisible to the entire electromagnetic spectrum. Deciphering the nature of Dark Matter is one of the major challenges of modern physics though astrophysical observations provide ample evidence for the existence of an invisible and dominant mass component in the observable universe, from the scales of galaxies up to the largest cosmological scales. Dark matter has been identified beyond doubt by its gravitational effect, for example: the motions of visible matter, on galaxies, on the cosmic background, etc. The Dark Matter could be made of new, yet undiscovered elementary particles, with allowed masses and interaction strengths with normal matter spanning an enormous range. Axions, produced non-thermally in the early universe, and weakly interacting massive particles (WIMPs), which froze out of thermal equilibrium with a relic density matching the observations, represent two well-motivated, generic classes of Dark Matter candidates. Dark matter axions could be detected by exploiting their predicted coupling to two photons, where the highest sensitivity is reached by experiments using a microwave cavity permeated by a strong magnetic field. WIMPs could be directly observed via scatters off atomic nuclei in underground, ultra-low-background detectors, or indirectly, via secondary radiation produced when they pair annihilate. They could also be generated at particle colliders such as the LHC, where

associated particles produced in the same process are to be detected by detectors like CMS and ATLAS.

1.3 The LHC proton beam

The LHC accelerator is designed to collide proton-proton at a center-of-mass energy of 14 TeV. In addition, the LHC also collides heavy ions: proton-lead, lead-lead and xenon-xenon for experiments that study heavy ion collisions like LHCb. Protons are accelerated up to 26 GeV through the LINear ACcelerator, the Proton Synchrotron Booster and the Proton Synchrotron. After this stage, protons are injected into the Super Proton Synchrotron and once an energy of 450 GeV is reached they are injected in the LHC rings. The LHC consists of two separate rings in which the protons are accelerated in opposite directions and are brought to collision at fixed interaction points. Accelerated protons are maintained on a circular path using super-conducting dipole magnets, which provide a magnetic field of 8.3 T and operate at a temperature of 1.9 K. High Frequency (HF) cavities are used to accelerate the protons and to compensate for their energy loss in the circular orbit. The oscillation frequency of these cavities is tuned to 400 MHz and protons are required to be synchronized with it to be accelerated. For this reason, protons are grouped in so-called bunches with a designed bunch separation of 25 ns. Quadrupole and sextupole magnets focus the particle beam to increase the interaction probability in the four collision points. Protons are accelerated and brought to the interaction points in 2808 bunches, containing 1011 protons each. The designed luminosity to be delivered to the experiments is $10^{34} \text{ cm}^{-2} \text{ s}^{-1}$.

A schematic overview of the injection chain, the LHC ring and of the experiments is shown in Figure 2.1. The source of protons is a single bottle of hydrogen gas that is replaced every two years to ensure that it always is operating at the correct pressure. Hydrogen atoms stripped of electrons by an electric field to produce protons. The protons are separated into two beam pipes of the LHC. One part of the beam circulates in the clockwise direction while the other circulates in the anticlockwise direction. The time required to fill each LHC ring is 4 minutes and 20 seconds, and it takes exactly 20

minutes for the protons to reach their maximum energy of 6.5 TeV. Beams circulate for many hours in both pipes under normal operating conditions.

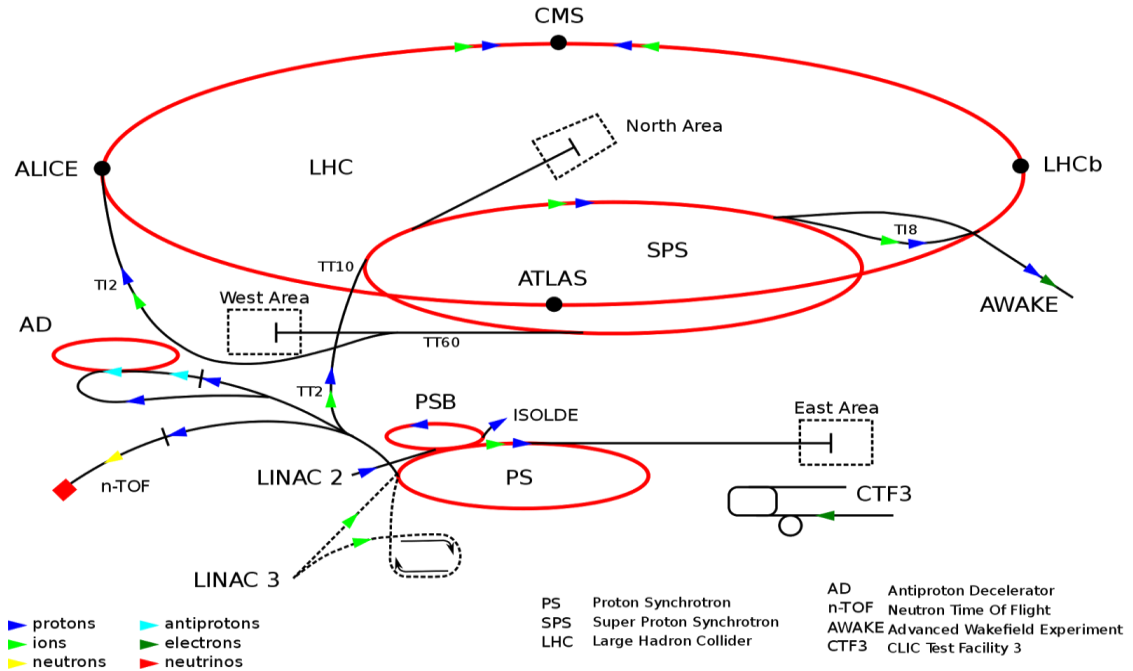


Figure 1.2: CMS, ATLAS, ALICE and LHCb detectors are shown. These are located around 27 kilometers in circumference. The beams of particles formed by protons or lead ions are moved through a succession of machines as: Linac 2, Linac 3, PS, PSB, SPS, etc.

1.4 CMS Experiment

CMS is one of four detectors of the LHC with a broad research program in particle physics of Standard Model precision and searching for physics beyond the Standard Model like Supersymmetry and Dark Matter.

The CMS experiment has 4300 collaborating physicists from 182 institutes in 42 countries. There are also engineers, technicians and students that form part of this research.

1.4.1 CMS Detector

The CMS detector [7] at the LHC accelerator at CERN is a general-purpose detector, designed to study proton – proton (pp) collisions at 14 TeV center of mass energy at a peak luminosity $5 * 10^{34} cm^2 s^{-1}$. The design of the CMS detector is driven by the challenges of a physics experiment in the LHC. The apparatus is 21 m long, 15 m wide, 15 m high and an overall weight of 14000 tons. The different layers are designed to stop, track and measure different types of particles emerging from proton-proton and heavy ion collisions provided by the LHC. The CMS detector is divided into silicon tracking system, an electromagnetic and a hadronic calorimeter and a muon system. A magnetic field of 4 Tesla is provided by a superconducting solenoid magnet. A schematic view of the CMS detector is shown in Figure 1.3.

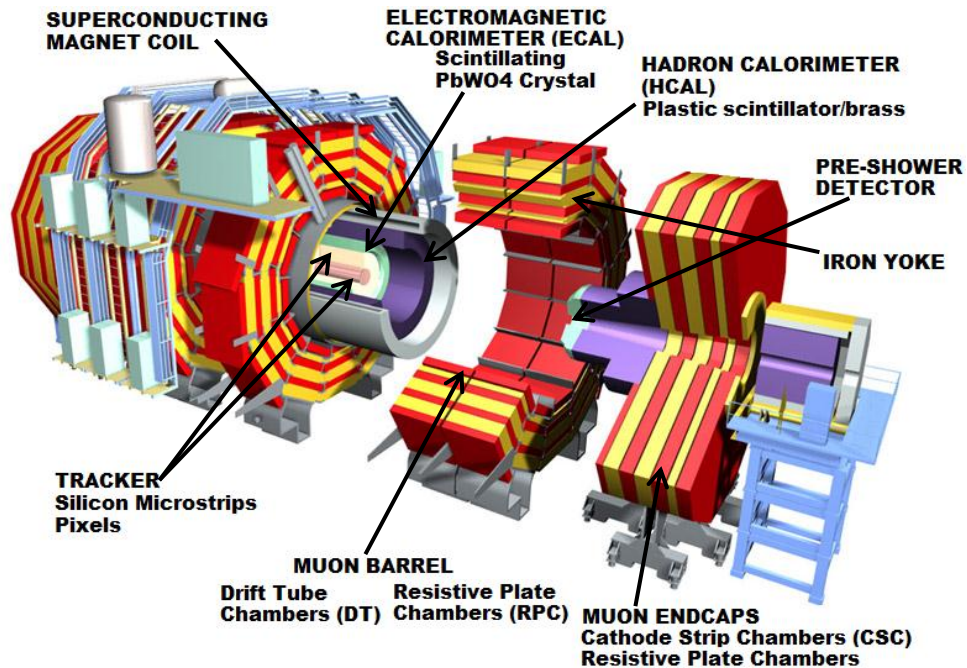


Figure 1.3: The CMS detector at the LHC designed to study proton – proton (pp) collision.

1.4.2 Magnet

The 3.8 Tesla CMS Magnet is a superconducting solenoid and is the central device as almost all the different subdetectors are embedded in it. This magnetic field oriented parallel to the beamline is about 100000 times stronger than the magnetic field of the Earth. Charged particles move in helical trajectories inside the magnetic field. The deflection angle θ of charged particles in the plane transverse to the beamline is given by $\theta = \rho/L$, where ρ is the bending radius and L is the solenoid length. From the curvature, the momentum component P_t perpendicular to the magnetic field B is given as $0.3zB\rho$ assuming a particle of charge ze . The magnetic coil is 13 m long with an inner diameter of 6 m and has a total weight of about 12000 tons. It is considered the largest superconducting magnet in the world today [8].

1.4.3 Muon System

The CMS muon system identifies and measures the momentum of muons and provides a trigger for event selection. The muon system constitutes the outermost subdetector and is placed outside the CMS magnet. It is divided into a barrel region and two endcap parts.

Drift Tubes (DTs) forms the barrel component and covers a pseudorapidity range up to $|\eta| < 1.2$. DT measures muon position in the barrel part of the detector. It contains 4 cm wide tubes with gas content and stretched wires. Each DT chamber has 2 m x 2.5 m in size with 12 aluminum layers, arranged in three groups of four and each contains up to 60 tubes. The choice of DTs as gaseous particle detector is due to the low muon rate, the small neutron induced background, and the uniformity of the magnetic field in this region. DTs give two coordinates for the muon's position, where the mean group measures the coordinates in the direction parallel to the beam while the two outer groups measure the perpendicular coordinate.

Cathode strip chambers (CSC) make the endcap disk and covers a pseudorapidity interval $0.9 < |\eta| < 2.4$. In this part, the muon rate and the neutron induced background are higher and the magnetic field is large and non-uniform. Therefore, a faster response

time, finer segmentation and radiation resistance is required. CSC contains the arrays positively-charged anode wires and negatively charged copper cathode strips in gas volume. When the muons pass through the volume, they knock electrons off the gas atoms which are collected in the anode wire in a high quantity. In contrast the positive ions are directed to the copper cathode, inducing the charges in the orthogonal strips along the wire, which allows obtaining two position coordinates for each passing particle. Each CSC module has six layers that allow to accurately identifying muons. The resolution for single point measurements is about 200 μm for DTs and CSTs.

Resistive plate chambers (RPCs) are placed both in the barrel and endcap regions and cover a pseudorapidity interval $|\eta| < 1.6$. RPCs consist of two parallel plates with positive charge (anode) and negative charge (cathode). Both materials are made of high resistivity plastic and separated by a gas volume. RPCs are used as complementary trigger system and to improve operations at high rates. RPC have coarser position resolution than the DTs or CSCs, but they can be used to resolve ambiguities when reconstructing a track from multiple hits in a chamber.

1.4.4 Calorimeter

The calorimeter measures the energy of particles through their interactions with matter and allows inferring the presence of neutral particles. The calorimeter is divided into Electromagnetic Calorimeter (ECAL) and Hadron Calorimeter (HCAL). In the ECAL the particle energy is measured through electromagnetic showers while in the hadronic part is measured via inelastic scattering. Information from energy deposits in the calorimeter system is used to trigger system.

ECAL of CMS is divided into barrel and endcap detectors and it has been designed to obtain a good invariant mass resolution, through the determination of energy and position, and a fine granularity for photon identification for enhances the sensitivity to the $H \rightarrow \gamma\gamma$ decay. The ECAL uses scintillation crystals made from tungstate (PbWO_4) [9] to measure the energy electromagnetically interacting particles (main electrons and photons) with a large pseudorapidity coverage up to $|\eta| < 3$ [10]. The scintillation light produced in the crystal is read out by avalanche photo diodes (APD) in the barrel and by

vacuum phototriodes (VPT) in the endcaps. The nominal operating temperature of the ECAL is 18°C, and it is provided by a water cooling system and it has a dependence of the crystal light yield.

HCAL [11-13] is formed of 17 layers of brass absorber and scintillator 11 tiles. It is organized into barrel (HB), endcap (HE) and forward (HF) sections. There are 36 barrel "wedges", each weighing 26 tonnes and complemented by an outer barrel (HO) and quartz fiber 12 forward detectors. The Hadron Calorimeter (HCAL) measures the energy of hadrons, particles made of quarks and gluons (protons, neutrons, pions and kaons). It is very important to measure these particles because it gives us information about the formation of new particles such as the Higgs boson or supersymmetric particles.

1.4.5 Tracker

The tracker refers to the innermost system (closest to the beam pipe) of CMS detector that detects and tracks the charged particles. It has a total length of 5.8 m and a diameter of 2.6 m, and it covers η up to 2.5.

Using the solenoid magnet, the tracker records the paths taken by charged particles by finding their position very precisely and allows for momentum measurement and pattern recognition. It reconstructs the paths of high energy muons, electrons and charged hadrons (particles made up of quarks) and identifies primary proton-proton collision and secondary vertices from short lived particles, for example, b-quarks. Reconstruction and identification of b-jets [14], called b-tagging, is the key to discovering physics processes Beyond the Standard Model like Supersymmetry extra dimensions, and extra gauge bosons.

B-hadrons that contain bottom quarks have lifetimes of the order of the picosecond, and during this time they can travel several millimeters from the primary vertex (PV). The b-quark then decay into spray of particles whose trajectories (tracks) emanate from a secondary vertex displaced from the primary interaction vertex. A reconstructed track is therefore a key to b-tagging, Therefore the tracker must have a good resolution to identify all the b quarks vertices.

The tracker builds traces that leave the particles accurately using only a few measuring points (each measurement is accurate to $10\ \mu\text{m}$, a fraction of the width of a human hair). As it is the innermost layer of the detector, it receives the highest radiation due to the large volume of particles generated by the collision of the proton beams.

The tracker features silicon pixels (Pixel Detector) and microstrip (Silicon Strip Detector). Pixel Detector (Phase-1) is placed closest to the interaction point and constitutes the innermost layer of the tracker. The geometrical layout of the Pixel Detector consists of four cylindrical barrel layers placed at radii of 29, 68, 109, 160 mm and three disks in each of the forward regions placed at a distance from the nominal interaction point of 291, 396 and 516 mm. This layout is optimized to offer full 4-hit tracking coverage η up to of 2.5, with an increased redundancy compared to the present system (Phase 0, three cylindrical barrel layer and two disks in each of the forward regions). Silicon pixel detectors have a spatial resolution of better than $10\ \mu\text{m}$ in the $r - \phi$ plane and of about $20\ \mu\text{m}$ in the z -axis.

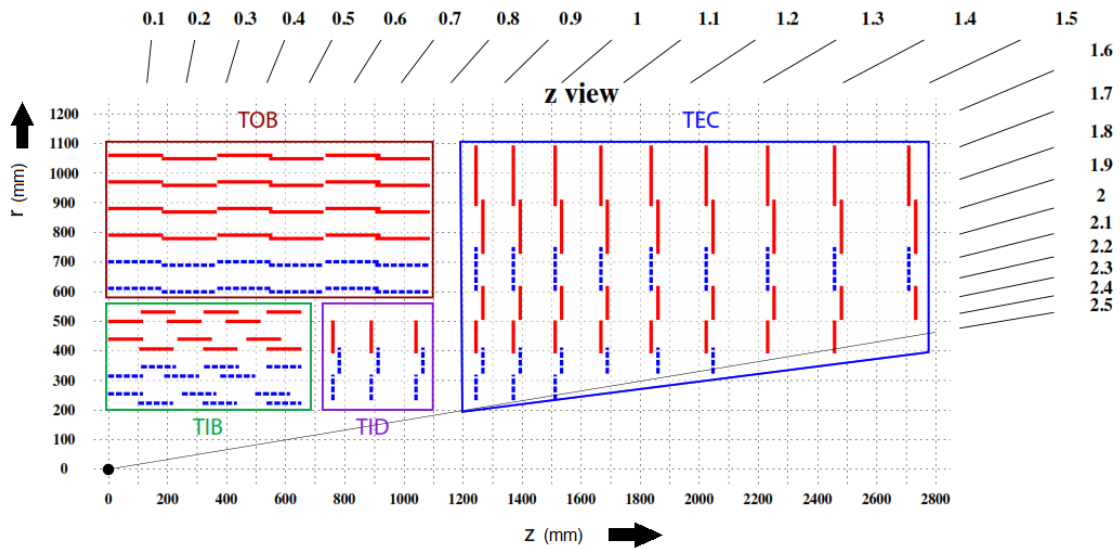


Figure 1.4: The schematic $r - z$ -view of one quarter of the silicon strip tracker is shown. Single sided silicon modules are indicated in red (solid lines) while double sided modules is shown in blue (dashed lines).

Silicon Strip Detector surrounds the pixel detector and are grouped in three larger sub- systems: Tracker Inner Barrel and Disks (TIB/TID), Tracker Outer Barrel (TOB),

and Tracker End Cap (TEC). Silicon microstrips have a resolution between 35 μm and 52 μm depending on the direction. A schematic view of Silicon Strip Detector is shown in Figure 1.4.

Chapter 2

Previous Work

The physics program at the Large Hadron Collider (LHC) began in 2010 with pp collisions at a center of mass (CM) energy of 7 TeV. By the end of 2011, a data sample with integrated luminosity of $6 fb^{-1}$ was collected by CMS. The energy was increased to 8 TeV and in 2012 a further $11 fb^{-1}$ integrated luminosity was delivered, with instantaneous peak luminosities approaching $7 * 10^{33} cm^{-2}s^{-1}$. Throughout this period, the LHC has operated with bunch trains with 50 ns bunch spacing. Throughout this period, the original Pixel Detector (called Phase-0 Pixel Detector) performed excellently and played a crucial role in the discovery of the Higgs boson. The Phase-0 Pixel Detector was installed in CMS apparatus in 2007 and took 10 years to design and build (1997-2007). The original design goal of the LHC was to operate up to $7.5 * 10^{34} cm^{-2}s^{-1}$ with 25 ns bunch spacing, where approximately 25 simultaneous inelastic collisions per crossing (pile-up) occurred. With the upgrade of the LHC accelerators, the luminosity and pile-up doubled. The Phase-0 Pixel Detector was not designed to perform effectively in such a scenario and more so with radiation damage accumulated over 8 years of operation, it was essential to replace this pixel detector. It was replaced in early 2017 by a completely new detector with an improved design and is referred to as Phase-1 Pixel Detector. It maintains the same high efficiency and low fake rate of the Phase-0 Pixel Detector in a higher pile-up scenario of > 20 . In the following section, we describe the design of the original Pixel Detector and the current Phase-1 Pixel Detector.

2.1 The Phase-0 Pixel Detector

This detector is one of the first of its kind ever to be installed in a particle physics detector with a goal to combine robust tracking with a precise vertex reconstruction and a strong magnetic field (4T) to address the full range of physics accessible at this energy. The pixel detector was placed at the core of an all-silicon tracking system [15] which is the innermost component of the CMS detector. The pixel detector consists of two components the barrels and the disks. There are 3 layers of barrels complemented with 2

disks on each side. The disks are called the Forward Pixel detector (FPIX) and the Barrel Pixel detector (BPIX). Innovative techniques of radiation hard technology and bump bonding have been used to meet the challenge of high radiation environment and small space availability. The pixel detector provides a hit resolution of 10 mm in the ($r\phi$) and 17 mm in ($r\eta$) coordinates and remain functional up to a fluence of $6 * 10^{14} n_{eq}/cm^2$.

The barrel layers are located at radii of 4.4, 7.3 and 10.2 cm, respectively from the proton beam direction, whereas end disks lie on each side of the pixel barrel at 34.5 and 46.5 cm from the center of the barrel. The active surface is about one square meter, instrumented with 66 million channels. Figure 2.1 illustrates the three-layer pixel barrel and 2 end disks per side. BPIX is composed of 48 million pixels, i.e., 11520 Readout Chips (ROCs) and 1120 readout links, while the FPIX comprises of 18 million pixels (4320 ROCs and 192 Readout links) [16, 17]. The pseudo-rapidity range covered is $|\eta| < 2.5$, matching the acceptance of the surrounding silicon strip tracker. In order to achieve the optimal vertex position resolution in both the ($r\phi$) and the z coordinates, a design with an almost square pixel shape was adopted. To enhance the spatial resolution by analog signal interpolation, the effect of charge sharing induced by the large Lorentz drift in the 4T magnetic field is used. Hence the detectors are deliberately not tilted in the BPIX, but are tilted in the FPIX resulting in a turbine like geometry. The use of signal interpolation means that full analog information is transferred from each hit pixel. Figures below shows the η -coverage of the pixel detector and the layout of barrel and endcaps.

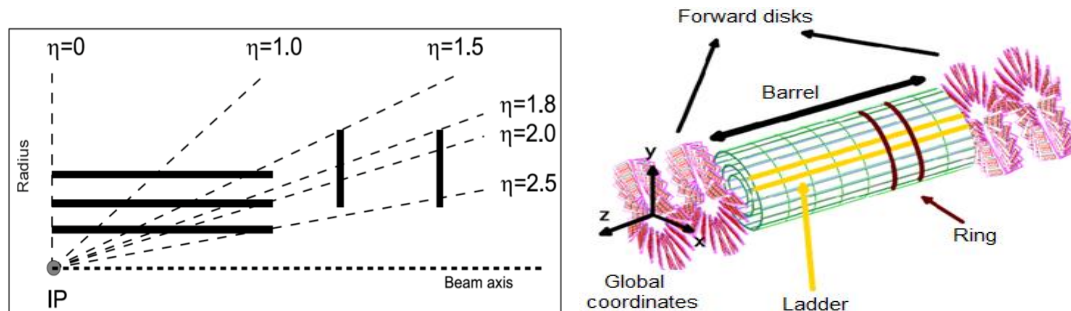


Figure 2.1: The phase-0 of the pixel detector with 3 barrel layers and 4 disks.

2.1.1 Sensor and Readout Chip

Sensor: The sensors used were made SINTEF (company that makes the sensors) and the PSI46V2 Readout Chip was designed by Paul Scherrer Institute (PSI). The CMS pixel sensors are manufactured in the “n-on-n” technique, consisting of n+ structures on n bulk silicon. When a charged particle enters the biased sensor, the electrons and holes created by its passage drift in opposite directions; it is the electrons that are collected and amplified by the readout chip to indicate a hit pixel. Electrons have a higher mobility than holes and this design has the benefit that after radiation causes a sign inversion of the sensor’ charge, the highest electric field is still located closest to the collection electrodes. These sensors can still be operated efficiently after charge inversion, but the pixels need to be isolated from each other. An n-side isolation is implemented between neighboring n+ pixels since the electron accumulation layer induced by oxide charge build up will short the pixels. A “p-stop” technique is used in the endcaps where the n+ pixel is surrounded by a p-stop implant, whereas the barrel pixel sensors use “p-spray” isolation (Figure 2.2). To avoid breakdown, a multi guard-ring is used to control the potential drop at the edge of the sensors to operate up to bias voltages of 600 V before breakdown. Each sensor has a thickness of 285 μm thick with a pixel size of $100 \times 150 \mu\text{m}^2$.

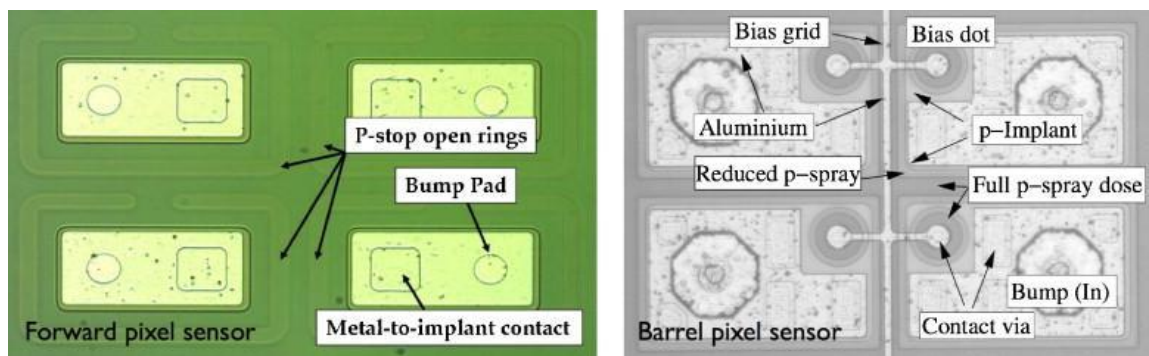


Figure 2.2: Forward and Barrel pixel sensor of the CMS detector.

Readout Chip: The ROC for the pixel detector (called PSI46V2 and designed by engineers and physicists at the Paul Scherrer Institute) is designed to record position and charge for all hit pixels with a time resolution of 25 ns , which is the designed time between two LHC bunch crossings. The ROC has been fabricated in $0.25\ \mu\text{m}$ CMOS technology. This information is stored on-chip during the CMS first level trigger latency of $3.2\ \mu\text{s}$ after which they are either read out, or discarded. The ROCs are read out serially via 40 MHz analog links. The chip integrates 1.3 million transistors in a $7.9\text{ mm} \times 9.8\text{ mm}$ area. It can be divided into three functional blocks: a control and supply block in the chip periphery, an array of PUCs organized in double columns, and the double column peripheries which control readout and trigger validation within double columns. The total number of pixels is 80×52 with a pixel size of $100 \times 150\ \mu\text{m}^2$ (Figure 2.3). The readout chip contains a serial programming interface with I^2C -like protocol and a fast signal encoder. It also has twenty-one 8-bit digital-to-analog converters (DACs), five 4-bit DACs and one 3-bit DAC to adjust offsets, gains, thresholds, supply voltages, timings etc. It consumes a total of about 120 mW (milliwatt) which corresponds to only $29\ \mu\text{W}$ per pixel. The voltage regulators are programmable and hence the voltages can be set for each chip separately. The double column periphery controls the transfer of hit information from the pixels to the storage buffers (column drain mechanism) and performs trigger verification. Each pixel on the sensor is bump-bonded to each pixel on the ROC using either and indium (FPIX) or a solder (Sn) bump (BPIX), as shown below.

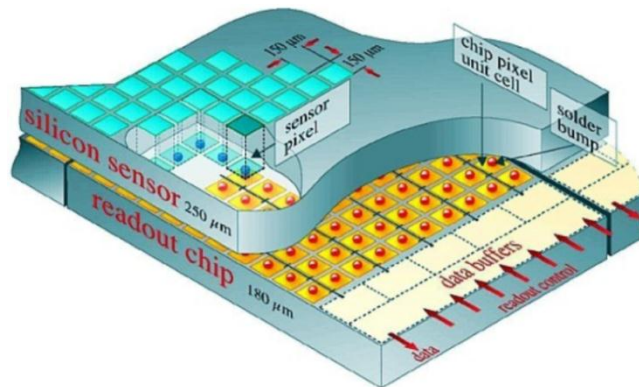


Figure 2.3: The silicon sensor and readout chip of CMS pixel detector-phase-0.

2.1.2 The detector layout

Each layer is made up of ladders, and each ladder is made up of eight modules (6.63 cm in length) with a small gap of 0.04 cm between each module. The effective gap is somewhat larger since the inactive area on the sensors is 0.09 cm, giving a total gap between active areas of 0.22 cm. Each full detector module has dimensions of 1.62 cm x 6.63 cm and is connected to sixteen readout chips (ROC's).

Each FPIX disk consist of 24 double sided blades arranged in a fan-like structure with a 20° tilt to encourage charge sharing between pixels from charged tracks since now, on average, tracks would impinge on the forward disks with a 20° impact angle. Without this tilt, there would be very little charge sharing since the magnetic field of CMS is parallel to the beam axis. Each blade in a disk has four detector modules called plaquettes on the side facing the interaction region, and three plaquettes on the other side, facing away. These plaquettes range in size from two to ten ROC's and are placed so that there is full coverage with the gaps from one side, covered by the plaquettes on the other. The active overlapping area is about 2%. Figure 2.4 illustrates the hit efficiency of the pixel detector, while Figure 2.5 shows the charge distribution in the barrel pixel.

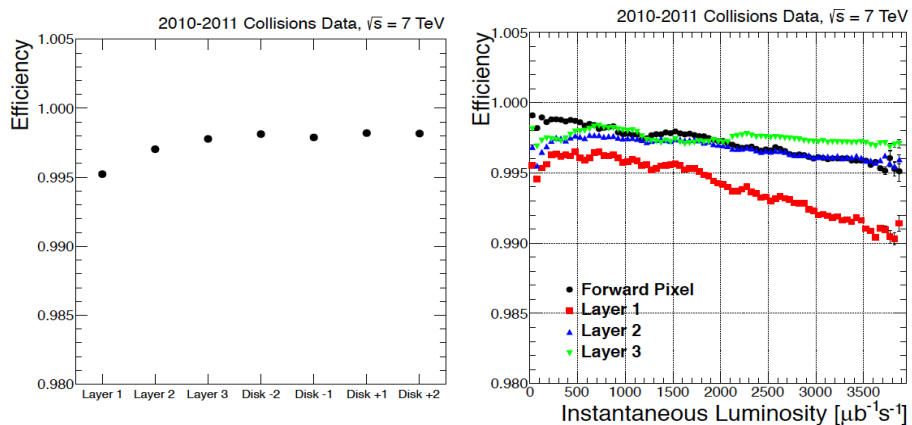


Figure 2.4: Pixel tracking performance measurements from 2010 and 2011 data. Left: Average module hit efficiency per layer/disk in the pixel detector once modules excluded from the readout are excluded from the measurement. Right: Average module hit efficiency as a function of the instantaneous luminosity.

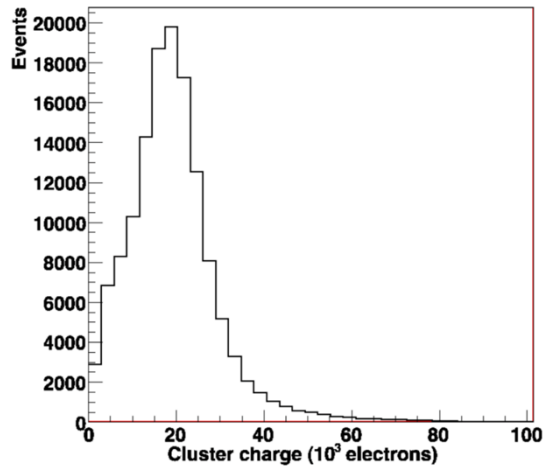


Figure 2.5: Cluster charge distribution in the barrel pixel detector normalized to a 285 μm path in silicon. The distribution shows the Landau like shape and peaks at about 21000 electrons as expected for full charge collection.

2.2 Phase-1 upgrade of Pixel Detector

The Phase-1 upgrade [18] is designed to meet the challenges posed by the excellent performance of the LHC with higher luminosity and integrated doses, and to mitigate many weaknesses that have been identified with the Phase-0.

The Phase-0 Pixel Detector was designed to efficiently record the first three space-points near the interaction region, out to $|\eta|$ up to 2.5, with a high precision in operating conditions up to the nominal instantaneous luminosity of $1 * 10^{34} \text{cm}^{-2} \text{s}^{-1}$ and a colliding bunch spacing of 25 ns. Under these conditions, an average of about 25 pile-ups is expected per bunch crossing. The performance was excellent with 95% channels functional. It played a crucial role in forming high quality seeds for the track reconstruction algorithm offline, fast tracking online in the high-level trigger (HLT) for primary vertex reconstruction, electron/photon identification, muon reconstruction, tau identification and b-tagging. However, a replacement of this detector is crucial for the reasons cited below to fulfill the physics goals of CMS and demands imposed by LHC beam.

1. The dynamic inefficiency increases with instantaneous luminosity and trigger rate due to limits in the internal readout chip buffers. The next main effect arises from single event upsets which cause the temporary loss of a module. These dynamic inefficiencies become significant for the inner layers when pile-up reaches 50 or more.

2. There is a significant portion of passive material in the overlap region between the BPIX and FPIX near $\eta \sim 1.5$, which degrades the impact parameter resolution of intermediate momenta tracks. This material is moved further out in the longitudinal direction outside the active tracking volume in the Phase-1 design.

3. The Phase-0 Pixel readout electronics is designed and optimized for the data rates and pixel occupancies expected up to the LHC design luminosity of $1 * 10^{34} cm^{-2} s^{-1}$ with a 25 ns bunch spacing. There will be a dynamic inefficiency of about 4% from the current readout chip PSI46v2 at this luminosity in the innermost barrel layer. At the nominal Level-1 trigger accept rate of 100 kHz, the data loss will increase to 16% in the innermost layer as the luminosity goes up by a factor of two (for 25 ns bunch crossing) to $2 * 10^{34} cm^{-2} s^{-1}$. The current readout chip is not able to cope with these rates in the innermost layers of the pixel detector.

Improvements due to Phase-0 Pixel Detector: The improvements from the Phase-1 detector are characterized by higher efficiencies, lower fake rates, lower dead-time/data-loss, and an extended lifetime of the detector. This leads to better muon ID, b-tagging, photon/electron ID, and tau reconstruction, both offline and in the HLT, improved particle flow leading to better estimation of missing energy. Good track reconstruction is key to future physics analyses. Figure 2.6 shows the expected tracking efficiency and fake rate of the Phase-1 detector in various pile-up scenarios (PU = 0, 50 and 100) in simulated tt events. The very large losses in efficiency with the current detector at high luminosities have largely been recovered, as shown in Figure 2.7. This leads to improvements in higher-level reconstructed objects like b-tagged jets. In addition to the gains in offline reconstruction, improvements in single track reconstruction play a beneficial role in the high-level trigger, when Level-1 objects are reconfirmed by tracks made from pixel hits alone. Finally, besides improving pattern recognition, increasing efficiencies and lowering fake rates, the addition of the fourth outer layer of the new

pixel detector plays another role. In case the inner layers of the TIB are compromised, the fourth layer largely offsets such losses, especially at high pile-up.

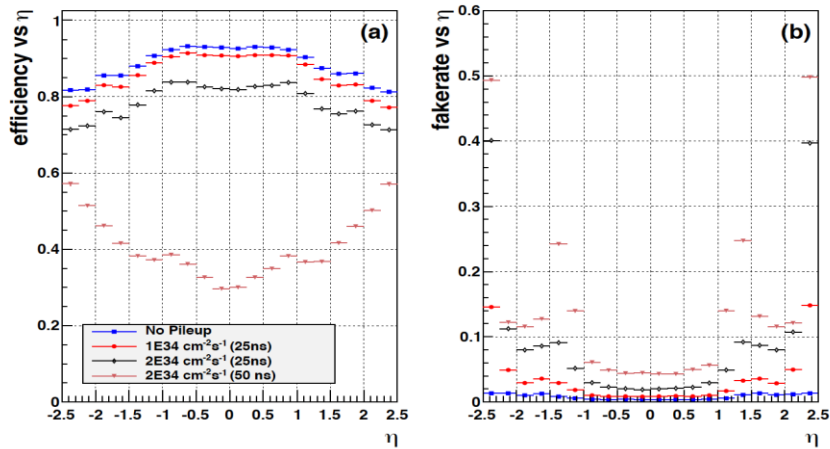


Figure 2.6: Performance of the Phase-0 pixel detector in simulated $t\bar{t}$ events: a) efficiency; b) fake rate.

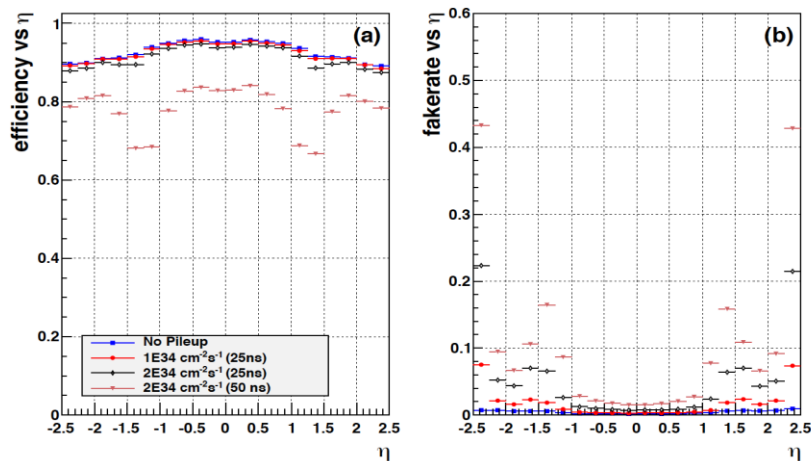


Figure 2.7: Performance of the phase-1 Pixel detector in simulated $t\bar{t}$ events: a) efficiency, b) fake rate. Results are shown for the upgraded pixel detector with zero pile-up (blue squares), an average pile-up of 25 (red dots), an average pile-up of 50 (black diamonds), and an average pile-up of 100 (magenta triangles).

Due to moving of services outside the pixel region there is a substantial improvement in mitigating the effect of the material budget as can be seen in Figure 2.8.

In order to observe more events in the decay of particles, it is necessary to increase the luminosity. The current pixel detector shall not be able to withstand the large occupancy resulting from the upgrade of the luminosity from $1 * 10^{34} cm^{-2} s^{-1}$ to $2 * 10^{34} cm^{-2} s^{-1}$. The increase in the luminosity will produce data readout inefficiencies.

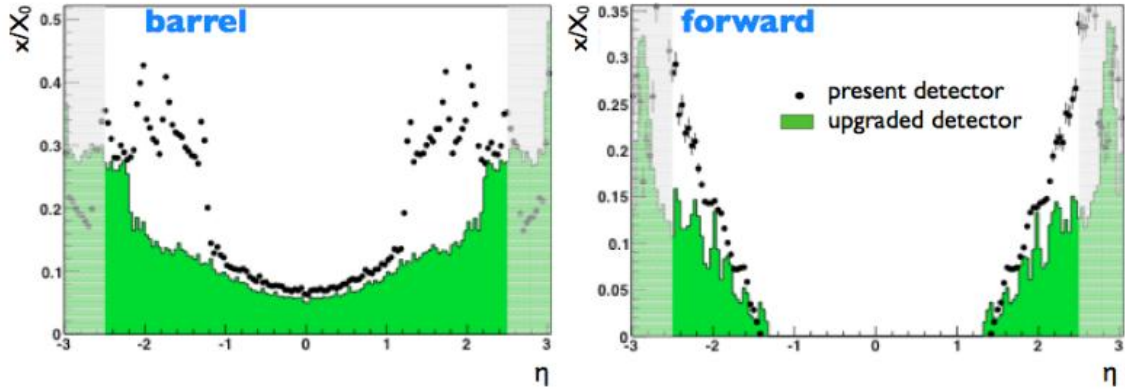


Figure 2.8: The amount of material in the pixel detector shown in units of radiation length (left), and in units of nuclear interaction length (right) as a function of η is given for the Phase-0 (green histogram), and the Phase-1 upgrade detector (black point). The shaded region at high $|\eta|$ is outside the region for track reconstruction.

2.2.1 Sensor and Readout Chip

Sensor: The sensor and ROC technology, as well as the pixel size remain unchanged compared to Phase-0. The silicon sensor is $285 \mu m$ thick and segmented with a cell size of $100 \times 150 \mu m^2$. The sensors are n+-in-n as in the Phase-0 pixels. The collection of electrons is advantageous because of their higher mobility compared to holes, which causes a larger Lorentz drift of the signal charges. This drift leads to charge sharing between neighboring pixels and thus improves the spatial resolution. Furthermore, the higher mobility of electrons makes them less prone to trapping, leading to a higher signal charge after high fluences of charged particles. After irradiation-induced space charge sign inversion, the highest electric field in the sensor is located close to the n+-electrodes used to collect the charge, which is also an advantage.

Readout Chip: The Phase-1 ROC, named PSI46dig, is an evolution of the present architecture manufactured in the same 250 nm CMOS process, where the core of the architecture is maintained, while achieving an enhancement in its performance. To increase the readout link speed, a change in signaling is needed. The Phase-0 readout protocol relies on linear data links where pixel addresses are encoded in 6 different analog levels. Furthermore, the analog pulse height information is transmitted. This system reached its limit in terms of speed. The Phase-1 ROC uses a 160 Mbit/sec LVDS data link. PSI46dig has 24-time stamp buffer cells (12 for the PSI46v2) and 80 data buffer cells (32 for PSI46v2). The data loss due to buffer overflows at fluences up to $600 \text{ MPix/sec/cm}^2$ is less than 0.5%. The operational charge threshold has also been reduced from 3500 electrons to 2800 electrons. Each ROC contains 80×52 pixels. Figure 2.9 shows the current pixel and upgrade pixel both in 3D and 2D.

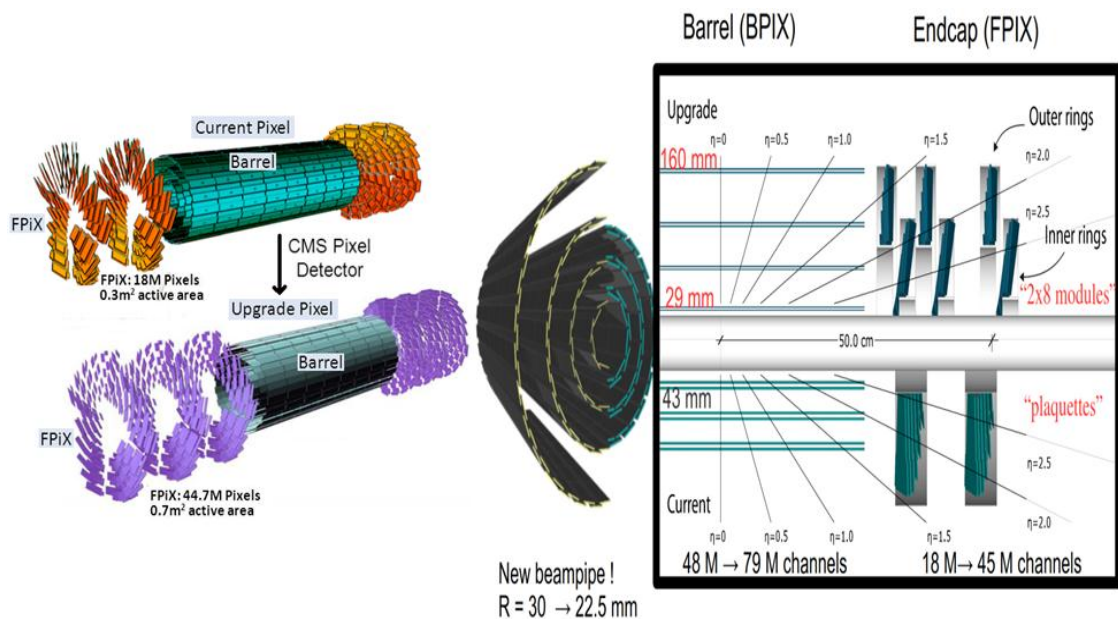


Figure 2.9: A comparison of layout of Phase-1 and Phase-0 Pixel Detector Layout.

The Module: The pixel module is the smallest subunit of the pixel detector and consists of several discrete components. An exploded view of module is shown in Figure 2.10. All components are carefully tested before being used in the module assembly. The

sensitive element of the silicon sensor has a dimension of $67 \times 18.6 \text{ mm}^2$ and a thickness of $285 \mu\text{m}$. It has 66560 pixels with a size of $100 \times 150 \mu\text{m}^2$ each. An array of 8×2 ROCs is connected via bump bonding to the silicon sensor. This structure is called Bare Module. The sensor leakage current as a function of bias voltage is tested on wafer level and bare module level. All ROCs are tested at the wafer-level to identify chips that are fully functional. Once they are loaded on a bare module, tests are performed to verify that the ROCs are still functional and measure the bump bonding yield. This is achieved using internal calibration signals that are injected capacitively into the silicon sensor. ROCs are connected and powered through a high-density interconnect (HDI) flex circuit. It is equipped with the passive elements (capacitors and resistors) and tested by the vendor. A token bit manager chip (TBM), that controls the readout of the ROCs and distributes clock, trigger and reset signals is mounted on top of the HDI at module production centers. The power and control signals are distributed to the HDI by a single micro twisted pair cable.

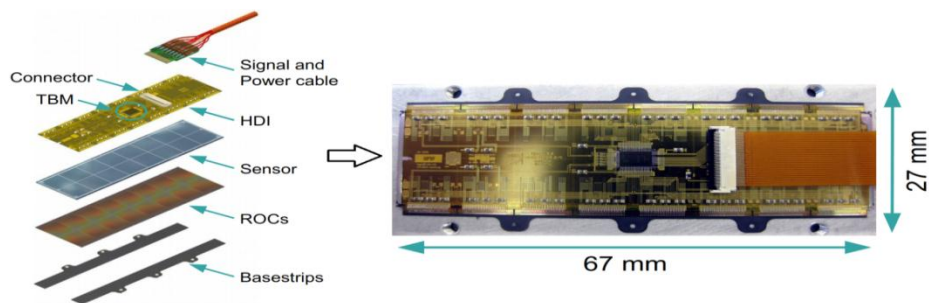


Figure 2.10: The pixel module for the CMS phase-I upgrade. All the surface components are mounted at Fermilab (FNAL) at the Silicon Detector Laboratory (SiDet).

Figure 2.11 shows a module placed on the FPIX disk. The disk has inner and an outer ring. Each disk has 56 modules (22 inner and 34 outer). Each pair of modules is attached to one blade (11 inner and 17 outer).

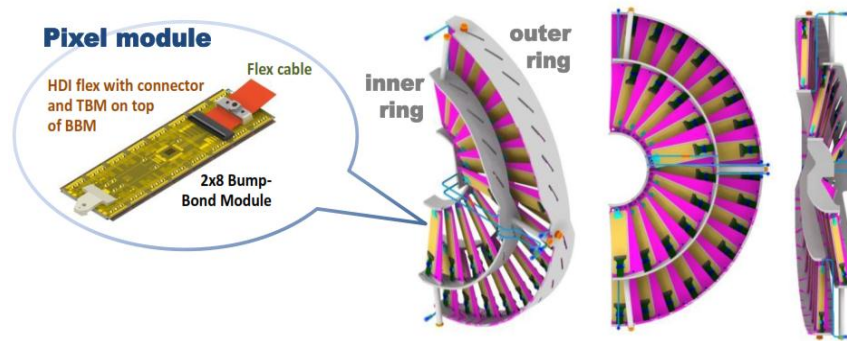


Figure 2.11: The upgrade detector of the 3 disks of FPIX module construction.

Pixel Unit Cell: The silicon sensor is the active unit of the module, converting energy deposited by incident particles into an electrical signal. Each sensor has 16 ROCs and each ROC covers an array of 80x52 pixels (4160 pixels); therefore, each sensor contains 66560 individual pixels.

The bulk of module testing concerns the pixel unit cell (PUC) of the ROC. The function of the comparator in the pixel unit cell is very important, because many analyses depend on this information to process the data correctly. When the particles pass through the silicon sensor, electrical charges are generated and their flow produces an analog signal as the current. Bump bonded or flip-chip bonded allows an electrical connection between detector and electronics. The connection procedure is performed through a special under-bump metallization. Lithography steps open holes to make the connections between these devices, as can be seen in Figure 2.12.

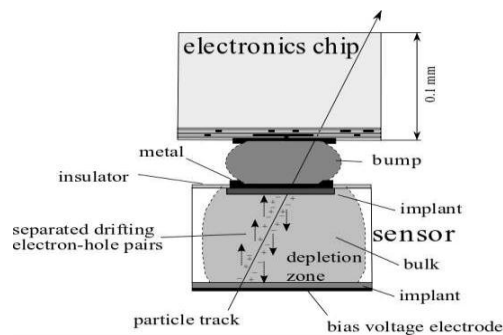


Figure 2.12: The bump bonded between sensor and electronic chip are illustrated.

The signal processing within the PUC begins with an amplifier and shaper that convert the incident current into a voltage signal, as is illustrated in Figure 2.13. The signal is then fed into a voltage comparator, the threshold of which is controlled by *VthrComp* with optional additional inputs from *Vtrim* and the Trim bits. If the input signal is greater than the comparator's threshold, the signal is automatically stored for readout and the pixel detects the logic at the periphery of the double column as a hit, which is transferred to the data buffer at the periphery. This allows starting the double column drain mechanism, transferring pulse height (PH) values from any pixel position with a hit registered.

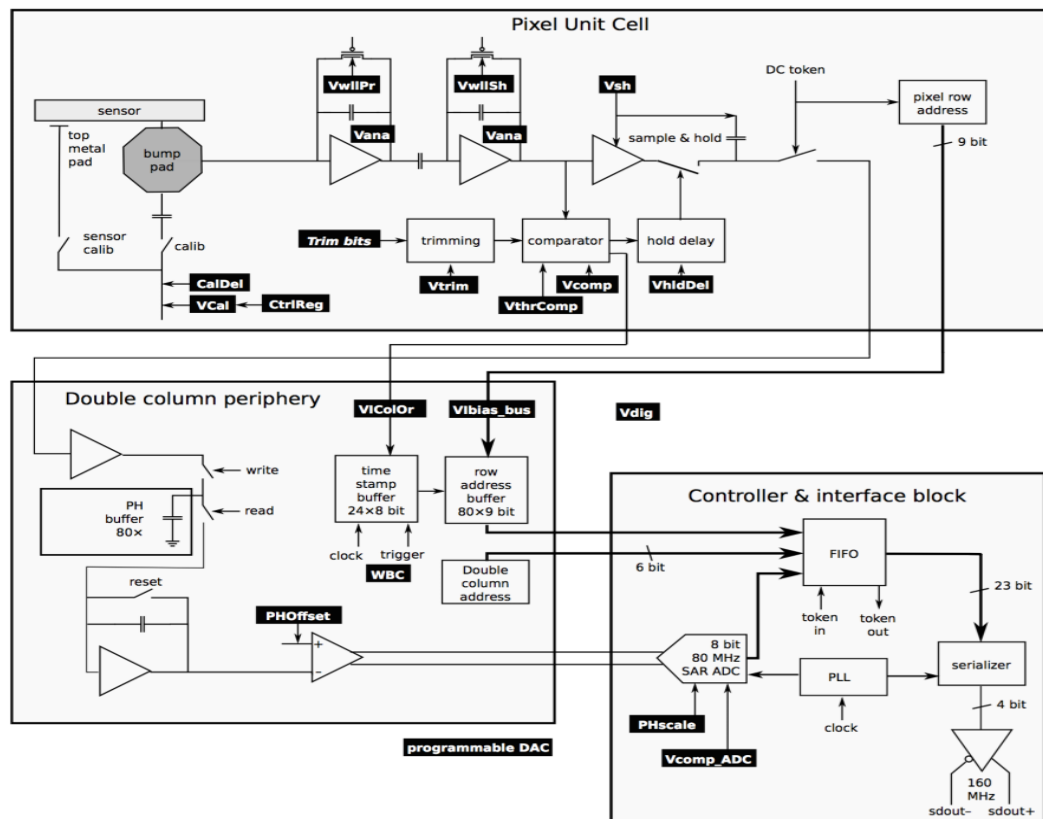


Figure 2.13: The pixel unit cell (PUC) of the ROC and the chip pixel cell.

Chapter 3

Objectives (Current Work)

The collision rate of pp collisions at the LHC has steadily increased since 2010 starting with instantaneous luminosities of up to $2.1 \times 10^{32} \text{ cm}^{-2}\text{s}^{-1}$ to $1.5 \times 10^{34} \text{ cm}^{-2}\text{s}^{-1}$ in 2016, exceeding the LHC design value of $1.0 \times 10^{34} \text{ cm}^{-2}\text{s}^{-1}$. It has resulted in some of the most exciting results and explored a wide range of physics; including the newly-discovered Higgs boson, top quarks [19], electro-weak bosons [20], quark gluon plasma studies [21], standard model and forward physics, as well as searches for new physics in which Phase-0 Pixel Detector has played crucial role till its replacement in early 2017 by Phase-1 Pixel Detector. The present data taking period, called Run 2, will continue until the end of 2018, followed a schedule gap of two years from 2024 to mid-2026, called shutdown, followed by another period of data taking called Run 3. It is expected that about 300 fb^{-1} will be collected by 2024 where the Phase-1 Pixel Detector would play a pivotal role in possible BSM discoveries and subsequently replaced by an upgraded detector called Phase-2 Pixel Detector. The shutdown will give opportunity to prepare the accelerator and CMS experiment for the High Luminosity phase of the LHC (called HL-LHC). Though upgrades on many parts of CMS apparatus are planned, our focus is only Pixel Detector.

The HL-LHC conditions of instantaneous peak luminosities up to $7.5 \times 10^{34} \text{ cm}^{-2}\text{s}^{-1}$ and an integrated luminosity of the order of $300 \text{ fb}^{-1}/\text{year}$ would result in 1 MeV neutron equivalent fluence of $2.3 \times 10^{16} \text{ n}_{eq}/\text{cm}^2$ (Figure 3.1) and a total ionizing dose (TID) of 12 MGy (1.2 Grad) at the center of CMS, where its innermost component, the Phase-2 Pixel Detector will be installed. The detector should survive the above radiation dose, handle projected hit rates of $3 \text{ GHz}/\text{cm}^2$ at lowest radius, be able to separate and identify particles in extremely dense collision debris, deal with a pileup of 140-200 collisions per bunch crossing and have high impact parameter resolution. This translates into requiring a detector design that is more highly granular, has thinner sensors and smaller pixels, and a faster and radiation hard electronics compared to Phase-1 counterpart. The selection of interesting physics events at the Level-1 (L1) trigger and

inefficiency of selection algorithms in high pileup conditions further require Tracker (of which Pixel Detector is a part) to be included in this trigger stage which would help reduce the event rate from 40 MHz rate to 7.5 kHz. The physics goals also require an increase in Pixel Detector coverage to $|\eta| = 4.0$ which improves the Missing Energy (MET) resolution and particle-flow event reconstruction by providing transverse momentum measurements and trajectories for charged particles entering the calorimeters. MET resolution is an essential performance parameter for many BSM physics searches including SUSY and extra dimension models, where particles escape undetected from the detector space. The smaller pixel size will further improve b-tagging as well as hadronic reconstruction and track reconstruction efficiencies within boosted jets. The boosted jets can be produced from new heavy objects decaying to Higgs, Z bosons, or top quarks - all heavy probes can be exploited for new physics searches. An improved b-tagging impacts most of future physics analysis that use top quark decays.

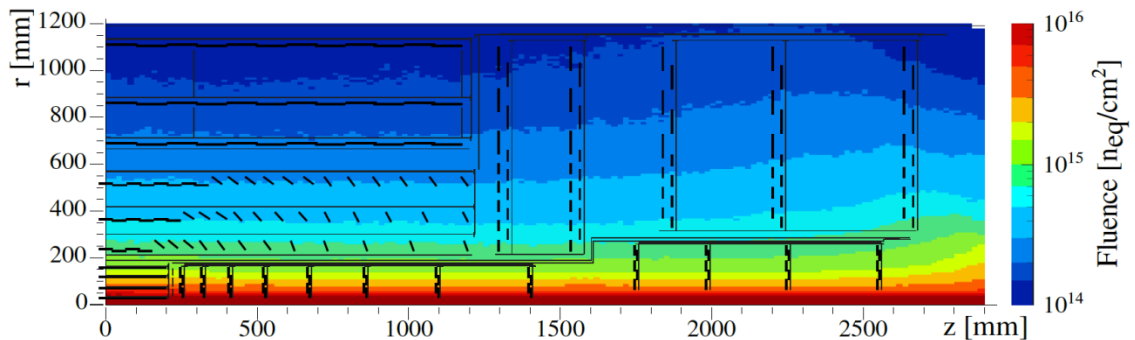


Figure 3.1: Integrated particle fluence in 1MeV neutron equivalent per cm^2 , for the Phase-2 tracker. The estimates shown correspond of pp collisions $\sqrt{s} = 14TeV$ and to a total integrated luminosity of $3000 fb^{-1}$.

3.1 Requirements for the Phase-2 Pixel Detector

The following requirements have been considered for the design of the Pixel Detector:

- The upgraded tracker must be fully efficient up to a target integrated luminosity of 3000 fb^{-1} , with appropriate margin.
- Narrower pitch than the present pixel detector, which features a pixel size of $100 \times 150 \mu\text{m}^2$, for better transverse and longitudinal impact parameter resolution.
- Increased granularity to limit the occupancy to the per mil level under high pile-up conditions and to improve track separation in jets.
- Capability to withstand the demanding hit rates and radiation environment with negligible inefficiencies.
- Geometrical coverage up to $|\eta| \sim 4$ to provide large forward acceptance and to mitigate pileup (particularly in the endcap calorimeters). Figure 3.2 shows one quarter of the pixel detector layout in the $r - z$ view.
- Simple installation and removal to allow for a potential replacement of inefficient parts.
- Capability to contribute to the real-time instantaneous luminosity measurement by hit counting or simple track counting.

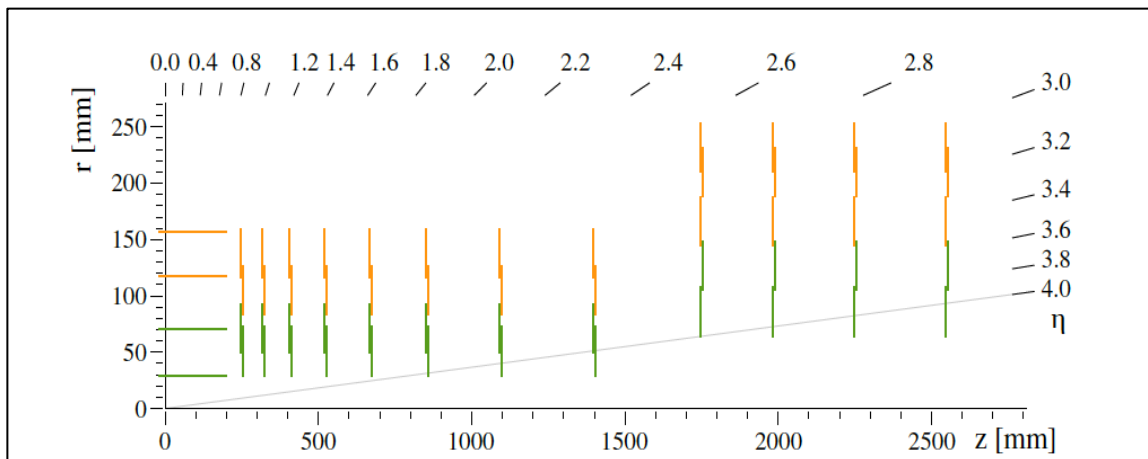


Figure 3.2: Sketch of one quarter of the pixel detector layout in the $r-z$ view. Green lines correspond to modules made of two readout chips and orange lines represent larger modules with four chips.

3.2 Detector Layout

The detector consists of a barrel part with four layers (referred to as Tracker Barrel Pixel Detector, TBPX), eight small double-discs per side (referred to as Tracker Forward Pixel Detector, TFPX) and four large double-discs per side (referred to as Tracker Endcap Pixel Detector, TEPX) as shown in Figure 3.3. In the TBPX the pixel modules are arranged in “ladders”. In each layer, neighboring ladders are mounted staggered in radius, so that $r-\phi$ overlap between ladders is achieved. The modules on a ladder do not overlap in z . A projective gap at $\eta = 0$ is avoided by mounting an odd number of modules along z , and by splitting the barrel mechanics in z into slightly asymmetric halves. In TFPX and TEPX the modules are arranged in concentric rings. Each double-disc is physically made of two discs, which facilitates to mount modules onto four planes, with overlaps in r as well as $r - \phi$. Each disc is split into two halves, and these D-shaped structures are referred to as “dees”. The TEPX will provide the required luminosity measurement capability by an appropriate implementation of the readout architecture. In total, the pixel detector will have an active surface of approximately 4.9 m^2 .

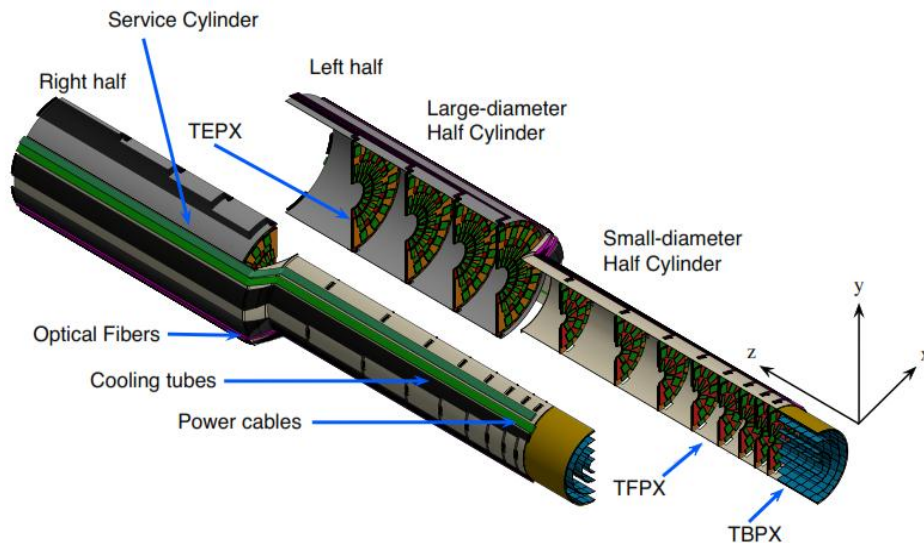


Figure 3.3: Phase-2 Pixel Detector Layout is shown.

A total power of about 50 kW feeds the active detector volume. As serial powering approach is used to minimize the material of the cables carrying the current. The approximate $1W/cm^2$ of power dissipated by the Readout Chips will be removed by a network of low mass cooling pipes fed by the common CO_2 cooling system. Bidirectional data transfer is implemented using low mass electrical links to connect the front-end to Low-power Gigabit Transceivers (LpGBTs) [22] on the IT support cylinder, while the LpGBTs are connected via optical fibres with the back-end electronics in the service cavern. Power, cooling, and data transmission services are carried on a cylindrical shell enclosing the pixel detector.

3.2.1 The Pixel modules

A pixel module is a basic unit of the detector comprised of a pixel sensor, several Readout Chips, a flex circuit, and a mechanical support. The sensors are *bump bonded* to the Readout Chips. A flex circuit, called high density interconnect, is glued onto the sensor and wire bonded to the readout Chips. It provides the data out, clock, trigger and control signals, as well as power distribution and hosts several passive and active electronic components. Low mass electrical cables connect the pixel modules to the global readout, control and powering systems. Heat generated on the module is removed via a layer of thermally conductive carbon foam to CO_2 cooling pipes, keeping the pixel chips and sensors at an operating temperature of about $-20^{\circ}C$. Modules are made of two and four chips, referred to as 1x2 and 2x2 modules, respectively, as shown in Figure 3.4.

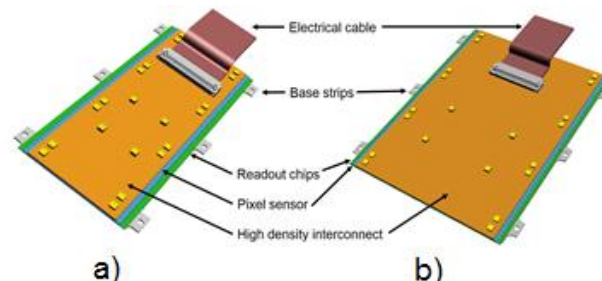


Figure 3.4: a) 1x2 pixel modules, b) 2 x 2 pixel modules for the barrel configuration.

The 1x2 modules populate the inner two layers of TBPX and the inner two rings of TFPX and TEPX, while the 2x2 modules are used in the outer two layers of TBPX and the outer two and three rings of TFPX and TEPX, respectively. These rectangular modules are arranged in the cylindrical geometry of the barrel with overlap of the active sensor areas in $r-\phi$, while no module overlap along z is foreseen. In the disc-like geometry of the endcaps, appropriate overlaps of the active areas are realized both in r and $r - \phi$.

3.2.2 Pixel sensor

HL-LHC entails a demand of very high radiation tolerance for the tracking devices, but also heavily increases the need for devices operating in the fluence range up to $10^{15} n_{eq}/cm^2$, currently covered by hybrid pixel detectors with n^+ -in- n sensors (double sided and used in Phase-0 and Phase-1 Pixel Detector). However, these devices are very expensive and the active area of pixel detector is bigger than ever. A cheaper alternative is a p^+ -in- n sensor, which is single sided, but requires higher post-irradiation full depletion voltage. Thin planar n-in-p type silicon sensors (of thickness 100–150 mm), segmented into pixel sizes of $25 \times 100 mm^2$ (with the long side pointing along z in the barrel and along r in the endcaps) or $50 \times 50 mm^2$, are expected to allow for a good detector resolution that is relatively stable with respect to radiation damage. The resulting reduction in the pixel area by a factor of six (compared to the Phase-0 and Phase-1 pixel detectors) will enable to achieve low occupancy and improved track separation in dense environments like high p_T jets.

3-D detectors, though expensive, are also being pursued as they have shorter charge collection distance which reduces trapping and the voltage needed for full depletion and offer intrinsically higher radiation since the production process is more expensive, and thus, not suitable for large volumes, the use of 3D sensors could be limited to the regions of highest particle fluences [23, 24].

Planar sensor: Planar silicon sensors produced on 6” n-in-p wafers will be used in the outer layers (layers 2–4) and rings (rings 2–4 in TFPX and all rings in TEPX) of the Inner Tracker, and possibly also in the first barrel layer and the first ring of TFPX. The

sensors will be exposed to a fluence of $2.3 \times 10^{16} n_{eq}/cm^2$ in the innermost layer for $3000 fb^{-1}$. The corresponding total ionizing dose (TID) will be about 12MGy (1.2 Grad). Thin sensors are preferred over thick ones since the initial advantage of a larger signal in thicker sensors disappears when severe trapping is present at large fluences. In addition, thinner sensors need smaller operational voltages and produce less leakage current. The active thickness of the planar pixel sensors will be in the range 100–150 mm (for comparison, the active thickness of the Phase-0 and Phase-1 pixel sensors is between 270 and 285 mm). Testing with radiation hard readout chips will indicate if planar pixel sensors can withstand the highest radiation levels, or if an exchange of the inner layer would be necessary. The design of small pixel cells is challenging and needs to be optimized taking the design rules of silicon sensor foundries into account in terms of Pixel bias schemes and pixel isolation. Figure 3.5 shows the layout of two adjacent pixel cells for sensors of the HPK submission with pixel sizes of $25 \times 100 mm^2$ and $50 \times 50 mm^2$.

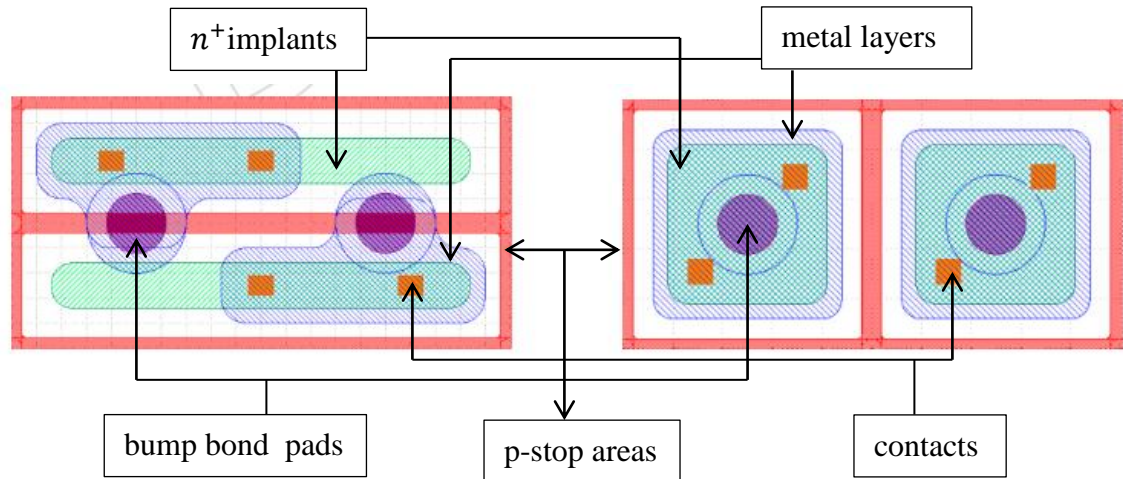


Figure 3.5: Drawing of two adjacent pixel cells for sensors from the HPK submission with pixel size $25 \times 100 mm^2$ (left) and $50 \times 50 mm^2$ (right). The n+ implants are shown in green, the metal layers in blue, the p-stop areas in red, the contacts in orange, and the bump bond pads in purple.

and a longer trigger latency ($12.5 \mu s$). Hits are stored during the trigger latency in the pixel array within multi-pixel regions (2×2 or 4×4).

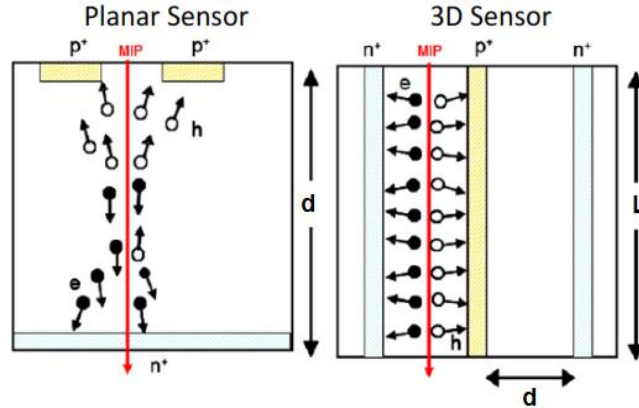


Figure 3. 7: A schematic illustration between planar and 3D sensors, where $L = 130 \mu m$ is the active thickness and $d \approx 50 \mu m$ is the collection distance.

Test Beam: The test beam program for the design of Phase-2 Pixel Detector is centered around testing several options for the 3D and planar pixel sensors from different vendors that are each bump bonded to a variety of Readout Chips (to make test module pairs that are characterized in a particle beam. The current vendors for planar (n+-in--p) sensors are: HPK (Japan), FBK (Italy) and SINTEF (Norway) and for 3D: FBK and CNM (Spain). Different ROC options available are PROC600, ROC4Sens (developed by PSI), FCP130 (developed by Fermilab) and RD53A (developed by CERN). However, at the time of writing this thesis, only PSI46dig ROC (used for Phase-1 Pixel Detector) is available to be bonded to sensors and this limits the radiation exposure of sensors to a factor of 10 lower than what is expected at the HL-LHC. The test beam facilities used for this purpose are located at DESY, Fermilab, and CERN SPS. In the near future, non-irradiated assemblies of 3D and planar sensors bump bonded to PROC600, PSI46, and FCP130 and irradiated 3D will become available for test-beam studies at Fermilab. In a further future RD53A and ROC4sens assemblies would also be available.

3.2.3 3D Sensors studied for characterization

In this thesis, a study of the two non-irradiated sensors (named 56B(2E) and 56D(3E)) at the Fermilab Test-Beam Facility (FTBF) is presented using 3D sensors from FBK (Fondazione Bruno Kessler, Trento, Italy). These are single sided n-in-p processes that include sensors made with Deep Reactive Ion Etching (DRIE) technology on 6-inch silicon wafers. These sensors are compatible with the PSI46dig readout chip used for the Phase-2 Pixel Detectors and it is the only suitable readout chip available at the time of this study. The data is collected using 120 GeV proton beams. The active thickness of these sensors is $130\ \mu\text{m}$. However, the effective thickness is estimated to be $120\ \mu\text{m}$, due to Boron diffusion from low resistivity CZ handle. These sensors are bump bonded using bumps made from Indium to the PSI46dig ROC. These sensors consist of two modules with pixels of standard size $100 \times 150\ \mu\text{m}^2$.

Figure 3.8 below shows the layout geometry and fabrication details of thin 3D sensors using of “6” Si-Si wafer. The distances between n and p electrodes are very short, which allows that lateral depletion, carrier drift and charge collections are given in a short time.

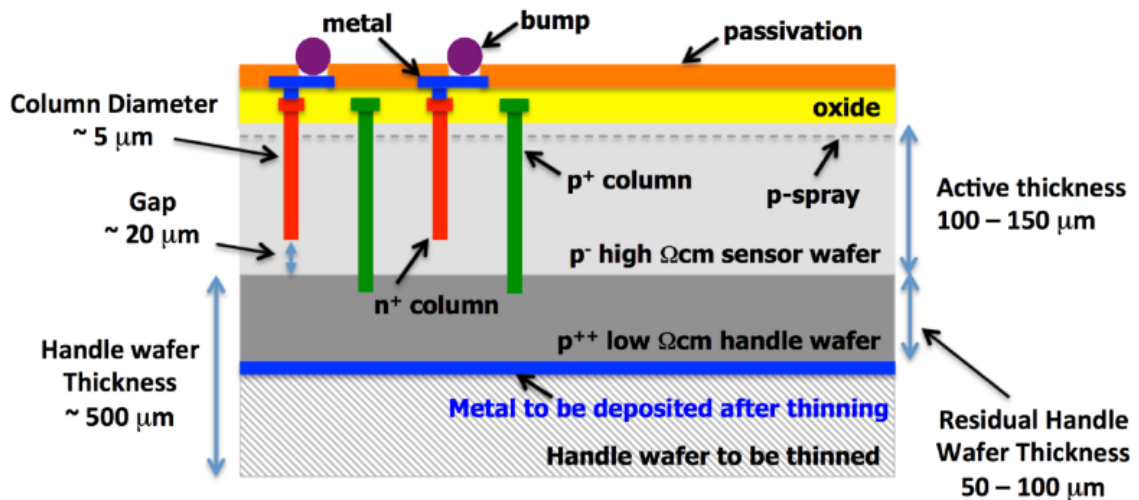


Figure 3.8: Shows the manufacturing details of layout of 3D sensor produced using “6” Si-Si wafer.

Figure 3.9 below shows a 3D sketch of the sensor structure. The rectifying n+ columnar implanter (signal or junction column) and non-rectifying p+ columnar implant (field or ohmic column) are shown in green and red dots, respectively. For each n+ implant there are 4 p+ implants, while for each 2 n+ implants, there are 6 p+ implants, and so on.

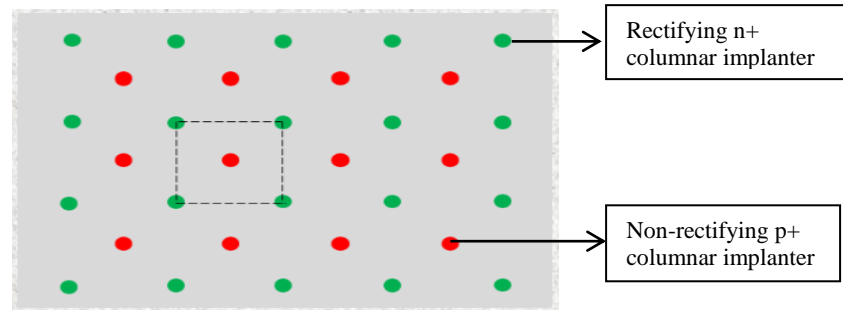


Figure 3.9: The columnar implant n+ and p+ are illustrated both signal and field.

Figure 3.10 illustrates the 2E and 3E module types of standard size ($100\ \mu\text{m} \times 150\ \mu\text{m}$), which form the structure of our sensors 56B(2E) and 56D(3E) under test. Basically, 2E and 3E sensors have cluster sizes of 2 and 3. Other smaller pitch sensor structures like $50\ \mu\text{m} \times 50\ \mu\text{m}$, $25\ \mu\text{m} \times 100\ \mu\text{m}$ were also studied, but do not form part of the work presented here. Whatever the configuration, they are bonded to the Phase-1 PSI46dig ROC. All channels of this ROC are bonded.

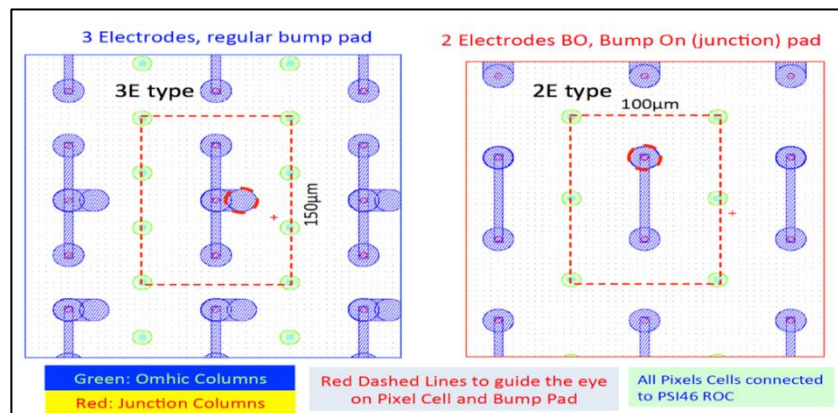


Figure 3.10: 2E and 3E module types of standard size with cluster size of 2 and 3.

3D sensors bump bonded to PSI46dig on beam-line are referred to as Detector Under Test (DUT). These DUT 0 correspond to 56D(3E) and DUT 1 to 56B(2E). More is explained in Chapter 5. A typical 6-inch wafer with different sensor geometries and pitch is shown in Figure 3.11. The PSI46dig marked on the sensor wafer corresponds to several pitches of the 3D sensor including the one studied here $100\ \mu\text{m} \times 150\ \mu\text{m}$.

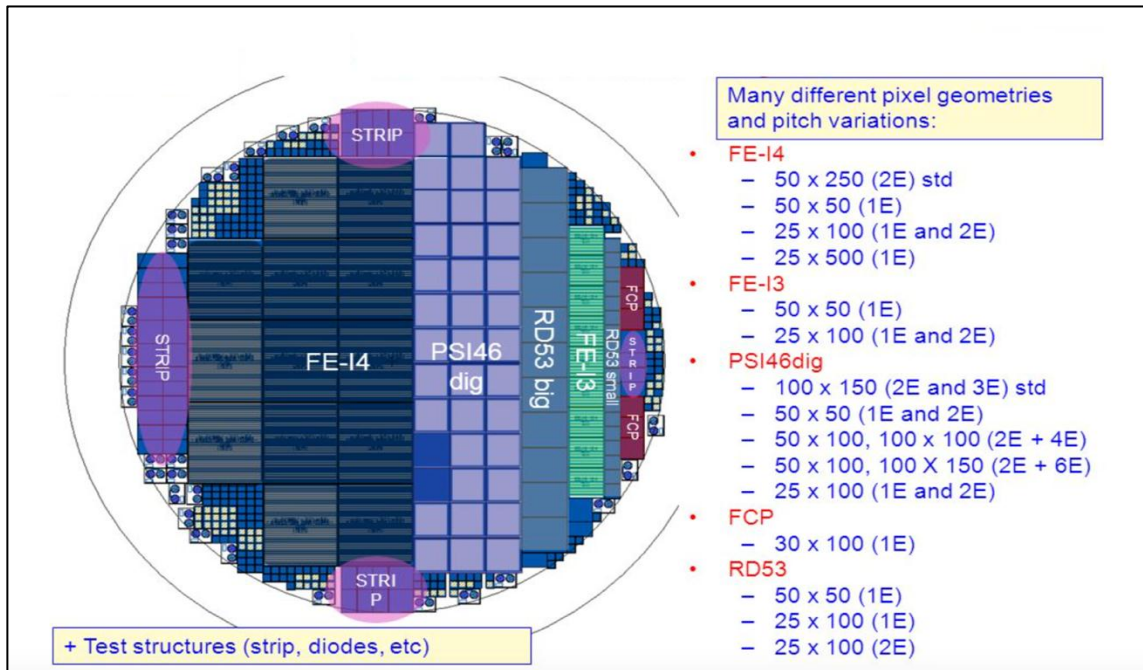


Figure 3.11: 3D Pixel First Batch Wafer Layout.

Chapter 4

Semiconductor detectors

A semiconductor detector in particle physics is a device that uses a semiconductor material to measure the energy of a particle that passes through it. The charged particle ionizes the material and its energy is measured by the number of electrons and holes produced in the detector material.

4.1 Silicon

Silicon [25] is the second most abundant element in the Earth's crust after oxygen. It is used as a semiconductor material by the electronics and microelectronics industry. Modern day integrated circuits are created from silicon wafers using lithography and used in microelectronics circuitry.

4.2 Thermal energy

In a pure silicon crystal at the temperature of 0 K, all valence electrons remain attached via covalent bonds and do not have enough energy to break and escape the bond, as is illustrated in Figure 4.1a. When the temperature increases in the silicon crystal, the amplitude of the atom vibrations around equilibrium position increases and as a result electrons acquire enough energy to break the bond and can move freely through the crystal lattice. This is shown in Figure 4.1b, where an electron breaks loose from a bond and a vacancy is left called a hole.

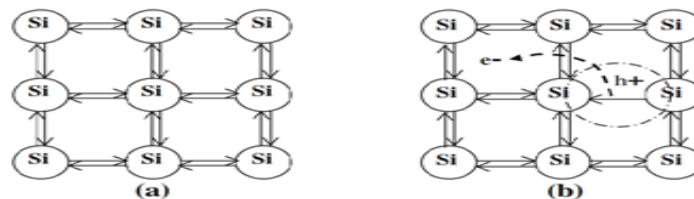


Figure 4.1: Schematic representation of Si bonds a) $T=0\text{K}$, b) thermal generation of electron-hole.

4.2.1 Energy band model

A silicon crystal with N identical lattice atoms has the possibility to exchange all the valence electrons with the remaining $N-1$ atoms. Thus, each energy level of the crystal atoms is split into N energy levels and can be occupied by two electrons of opposite spins. The value of N is on the order of $\sim 10^{23} \text{ cm}^{-3}$.

The width of the energy bands depends on how strongly the electrons are bound to the atom. There are two types of bands, the conduction band and the valence band; these are separated through the energy gap (E_g) (Figure 4.2), which is a function of lattice constant and depends of temperature, pressure, impurities etc.

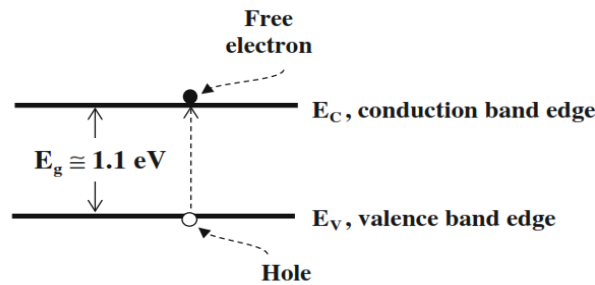


Figure 4.2: The valence band and conduction band separated by the energy gap (E_g).

When the temperature is fixed and uniform in the crystal and there are no external disturbances, it is said to be at thermal equilibrium. This means that for each temperature, there is a fixed number of concentrations of electrons, n and holes, p . For intrinsic silicon: $n = p = n_i \text{ cm}^{-3}$ and $\overline{pn} = n_i^2 \text{ cm}^{-6}$ where n, p and \overline{pn} indicate equilibrium values and n_i is the intrinsic carrier concentration which is the number of electrons in the conduction band (also the number of holes in the valence band) per unit volume in a semiconductor that is completely free of impurities and defects.

At the thermal equilibrium, the probability of an electron to occupy an energy level E (state energy) at temperature T is given by the Fermi-Dirac statistics expressions below.

$$f(E, T) = \frac{1}{1 + e^{(E - E_f)/kT}} \quad (4.1)$$

where $f(E, T)$ is the probability of occupancy that ranges from 0 to 1, k is the Boltzman constant and E_f is the Fermi energy or Fermi level [26, 27]. At thermal equilibrium, the Fermi energy is the same in semiconductors everywhere.

The intrinsic semiconductors are generally non-degenerate, so that the density of electron and hole are applied in these. Non-degenerate semiconductors contain moderate level of doping, where the dopant atoms are well separated from each other in the semiconductor host lattice with negligible interaction. The expression for the intrinsic carrier concentration can be written as:

$$n_i = \bar{n}|_{(E_F-E_i)} = N_c e^{-(E_c-E_i)/kT} \quad (4.2)$$

$$n_i = \bar{p}|_{(E_F-E_i)} = N_v e^{-(E_i-E_v)/kT} \quad (4.3)$$

To eliminate E_i , both equations are multiplied and then the square root is taken. The action law of mass is valid for intrinsic and doped material.

$$\bar{n}\bar{p} = n_i^2 = N_c N_v e^{-(E_g)/kT} \quad (4.4)$$

Where the bandgap energy $E_g = E_c - E_v$

The electron and hole drift velocity can be expressed as:

$$v_{dn} = \mu_n E \quad (4.5)$$

$$v_{dp} = \mu_p E \quad (4.6)$$

where μ_n is called the electron drift mobility and μ_p the hole drift mobility, they are measured in cm/Vs . v_{dn} and v_{dp} represent the average values $\langle v_{dn} \rangle$ and $\langle v_{dp} \rangle$. Physically, the drift mobility is a measure of the ease with which the carriers move in the silicon crystal and characterizes the performance of most semiconductor devices. In the presence of the electric field, electrons and holes move in opposite directions and the sum of the densities or the total current density (j) is given by:

$$j_n + j_p = q(v_{dn}n + v_{dp}p) = qE(\mu_n n + \mu_p p) \quad (4.7)$$

The conductivity of the crystal σ (S/cm) is expressed as:

$$\sigma = \sigma_n + \sigma_p = q(\mu_n n + \mu_p p) \quad (4.8)$$

The intrinsic resistivity is the inverse of the conductivity, and it is defined as:

$$\rho = \frac{1}{\sigma} = \frac{1}{q(\mu_n n + \mu_p p)} \quad (4.9)$$

When only donors (N_D) are present, ρ ($\Omega * cm$) can be approximated as:

$$\rho \cong \frac{1}{q\mu_n N_D} \quad (4.10)$$

In the same way, for only acceptors (N_A)

$$\rho \cong \frac{1}{q\mu_p N_A} \quad (4.11)$$

The intrinsic resistivity for an un-doped silicon material (electron and holes pairs are solely created by thermal energy) is calculated as follows, where $q = 1.6 * 10^{-19}C$, $N_D = 1.45 * 10^{10} cm^{-3}$ at $27^\circ C$, $\mu_n = 1350 cm^2/Vs$.

$$\rho \cong \frac{1}{(1.6 * 10^{-19}c) \left(1350 \frac{cm^2}{Vs}\right) (1.45 * 10^{10} cm^{-3})} = 3.2 * 10^5 \Omega * cm$$

4.3 The \overline{pn} -junction

The intrinsic silicon substrate in a standard silicon sensor has $\sim 10^9$ free charge carriers. When an ionizing particle passes through silicon about $2 * 10^4$ electrons are induced, however, not all of these are recollected, resulting in loss of signal. Lowering of temperature helps in recollection of the electrons. The other alternative is to deplete the silicon volume, using p - and n -type silicon in a \overline{pn} -junction.

Figure 4.3 shows the union of p - and n -type junctions. The first one shows the p - and n -type with the conduction and valence energy levels. In the second one, the electrons move to the lower Fermi energy and the holes move in the opposite direction. This

movement of the majority charge carriers is a consequence of dopant atoms in the semiconductor. In the third case, state of equilibrium is established between electrons and holes due the depletion of semiconductor volume creating space charge region (SCR).

In a semiconductor material, the charge carriers and their transport by diffusion gives rise to diffusion current. The diffusion current density is given by Fick's first law [28] as follows:

$$j_{dif} = -qD\nabla n \quad (4.12)$$

where $q = e = -1.6 \times 10^{-19} C$, D is the electron or hole diffusivity (cm^2/s).

At the $\bar{p}\bar{n}$ -junction diffusion (higher to lower concentration) and recombination (non-equilibrium) produce a charge layer that generates an electric field E , which prevents further diffusion of carriers. When the dynamic equilibrium is achieved, the diffused electrons and holes are gone, leaving behind the charged ions adjacent to the interface in a region with no mobile carriers.

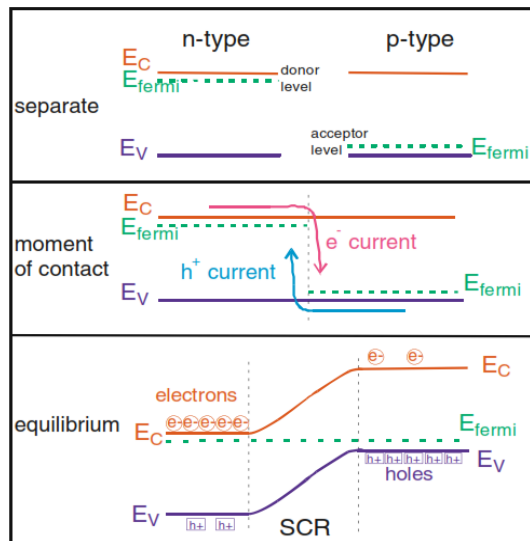


Figure 4.3: The p- and n-type unions with the energy levels of conduction and valence.

The mathematical representation of the semiconductor material can be visualized through diagrams. Figure 4.4a shows the configuration of electrons, holes, ionized donors and ionized acceptors in a $\overline{p}\overline{n}$ -junction.

The Poisson equation [29] can be used to describe the electrostatic potential $\varphi(x)$ as:

$$\frac{\partial^2 \varphi}{\partial x^2} = -\frac{1}{\varepsilon_{SCR}\varepsilon_0} \rho(x) = \frac{\rho(x)}{\varepsilon} \quad (4.13)$$

where $\varepsilon_{SCR} = \varepsilon_r$ is the dielectric constant ($\varepsilon_r = 11.7$), ε_0 is the electric constant ($\varepsilon_0 = 8.85 * 10^{-14} \frac{F}{cm}$), and $\rho(x)$ is the charge carrier density and is described by:

$$\rho(x) = -q[n(x) - p(x) + N_A - N_D] \quad (4.14)$$

where N_A and N_D are the impurity densities, i.e., acceptor and dopant (Figure 4.4b). In the contact region between the n- and p-type silicon, the free charges of the doped semiconductor compensate the charges of ionized and uncompensated impurities. Figure 4.4c shows the mobility charge density of electrons and holes. Figure 4.4d shows the depleted boundary layer ($w = x_p - x_n$), which is an insulating region of the semiconductor material. The only elements remaining in the space charge region (SCR) are ionized donor or acceptor impurities.

The pn depletion approximation are calculated by the integration of the Poisson equation. Figure 4.4e shows that the electric field strength increases linearly in the N-type region ($-x_n \leq x \leq 0$), while it decreases linearly in the P-type region ($0 \leq x \leq x_p$).

$$|E_n(x)| = +\frac{qN_D}{\varepsilon_{SCR}\varepsilon_0}(x + x_n); \quad |E_p(x)| = +\frac{qN_A}{\varepsilon_{SCR}\varepsilon_0}(x + x_p); \quad (4.15)$$

Using the boundary condition $\varphi(x = 0) = 0$, we obtain:

$$\varphi_n(x) = -\frac{1}{2}|E_{max}|x_n \cdot \left[\left(\frac{x}{x_n} \right)^2 + 2 \frac{x}{x_n} \right]; \quad \varphi_p(x) = -\frac{1}{2}|E_{max}|x_p \cdot \left[\left(\frac{x}{x_p} \right)^2 - 2 \frac{x}{x_p} \right] \quad (4.16)$$

The total difference of potential in the SCR gives the diffusion voltage:

$$V_{diffusion} = \varphi_n(+x_p) - \varphi_p(-x_n) = \frac{1}{2} |E_{max}| w = \frac{1}{2\mu\rho\varepsilon} w^2 \quad (4.17)$$

where μ (cm^2/Vs) is the mobility of charge carriers and ρ ($\Omega * cm$) is the specific resistance.

The diffusion voltage is on the order of millivolts in the SCR region (Figure 4.4f). The static charge generated does not contribute to the current because electrons and holes are in equilibrium and the system is externally stable. Therefore, there is an electrostatic potential energy between the p and n region, with a magnitude equal to qU_d (Figure 4.4g).

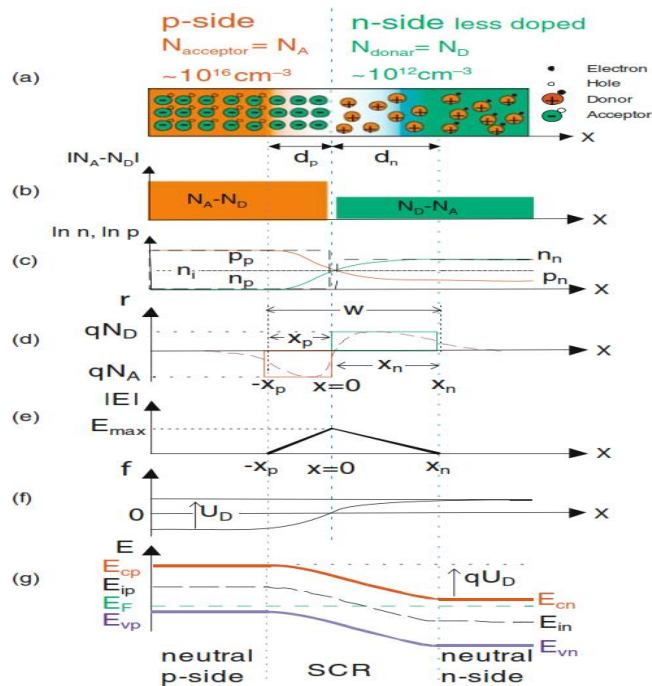


Figure 4.4: The mathematical representations of the semiconductor material under the equilibrium state. There is no external voltage.

When an external voltage is applied, the equilibrium is disturbed. This voltage can increase or decrease the potential barrier of the pn -junction depending on the polarity of applied voltage. For example, in the forward bias voltage ($V > 0$), the depletion width

decreases (Figure 4.5a), while in the reverse bias voltage ($V < 0$), the depletion width increases (Figure 4.5b).

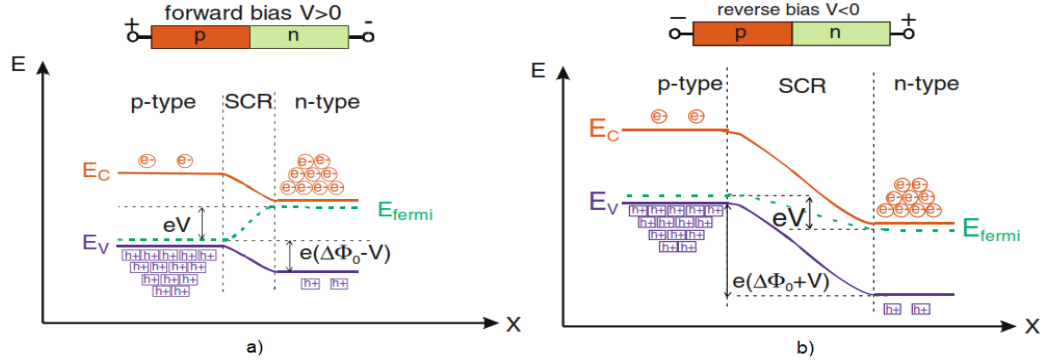


Figure 4. 5: The polarity in the potential barrier of the $\overline{p}\overline{n}$ -junction.

Silicon sensors operate in reverse bias voltage mode. In the silicon sensor, charge created in the SCR is collected at the junction, while charges created in the non-depleted zone recombines with free majority carriers and is lost. If the full volume is depleted, then $V_{external} = V_{bias} \gg V_{diffusion}$. The equation (4.17) can be expressed as:

$$w = \sqrt{2\varepsilon\rho\mu V_{bias}} \quad (4.18)$$

Likewise, with $w = D$ (the full sensor thickness),

$$V_{full\ depletion} = V_{FD} = \frac{D^2}{2\varepsilon\mu\rho} \quad (4.19)$$

Where V_{FD} is called the depletion voltage which is the minimal operation voltage needed to completely deplete the bulk silicon of thickness D . Figure 4.6 shows the electric field configurations for under-depletion, full-depletion, and over-depletion.

As an example, below, we calculate the bias voltage for a planar sensor of thickness $200 - 300 \mu m$ and for a 3D detector with interelectrode distance of $50 \mu m$ thickness. The resistivity is $\rho \cong 3 * 10^3 \Omega cm$, because silicon is doped with phosphorous (group V element) that leads to generation of free electrons [30].

Planar:
$$V_{FD} = \frac{(300\mu m)^2}{2*(11.7)(8.85*10^{-14}\frac{F}{cm})(1350\frac{cm^2}{Vs})(3*10^3\Omega cm)} = 107.3V$$

3D:
$$V_{FD} = \frac{(50\mu m)^2}{2*(11.7)(8.85*10^{-14}\frac{F}{cm})(1350\frac{cm^2}{Vs})(3*10^3\Omega cm)} = 2.98V \cong 3V$$

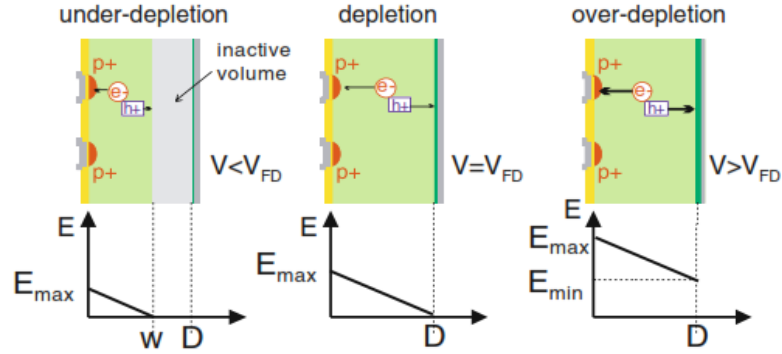


Figure 4.6: Behavior of the electric field in the bulk silicon. The strips and the backplane are on Ground potential and on high voltage potential.

For under-depletion: $V_{bias} < V_{FD}$; $E_{MAX} = \frac{2V}{w}$

For full-depletion: $V_{bias} = V_{FD} = \frac{qN_{eff}}{2\epsilon} D^2$; $E_{MAX} = \frac{2V}{D}$, where N_{eff} is the effective doping concentration in cm^{-3} .

For over-depletion: $V_{bias} > V_{FD}$; $E_{MAX/MIN} = \frac{V \pm V_{FD}}{D}$

When $V_{bias} > V_{FD}$ is established, an electric field disturbs the equilibrium in the SCR region. The thermally generated electron and hole pairs exit the depletion region. This undesired effect gives rise to a reverse current, also called leakage current I_L . The current density out of the depletion region is given by:

$$j_R = eG_{SCR}w = \frac{1}{2}e\frac{n_i}{\tau_L}w = \frac{1}{2}en_i\sigma v_{th}N_t w \quad (4.20)$$

with $G_{SCR} = \frac{1}{2}\frac{n_i}{\tau_L} = \frac{1}{2}n_i\sigma v_{th}N_t$ out of the depletion regions. On the other hand $j_R = \frac{I_L}{A}$, where A is the surface of the junction.

$$I_L = \frac{1}{2}e\frac{n_i}{\tau_L}wA = \frac{1}{2}en_i\sigma v_{th}N_t wA \quad (4.21)$$

The lifetime τ is determined by the impurities of interstitial atoms, $\tau_L = \frac{1}{\sigma v_{th} N_t}$, where N_t is the impurity/trap concentration, v_{th} is the thermal velocity ($\approx 10^7$ m/s) and σ the charge carrier cross section ($\approx 10^{-15}$ cm²). Equation (4.20) shows that the leakage current is completely determined by the effective lifetime τ_L that measures the generation lifetime of minority carriers, namely, the impurity states N_t near mid-gap.

The current increases linearly with depletion width, $w \propto \sqrt{V}$, until the detector is fully depleted. When a high bias voltage is applied, an electrical breakdown occurs and the current starts to increase dramatically even for little changes in the bias voltage. This might be explained by "avalanche breakdown", due to charge multiplication in charge collisions with the lattice or through the "Zener breakdown" based on the quantum mechanical "tunnel effect" [31]. Figure 4.7 illustrates $I \propto \sqrt{V}$ behavior, and breakdown at high voltage.

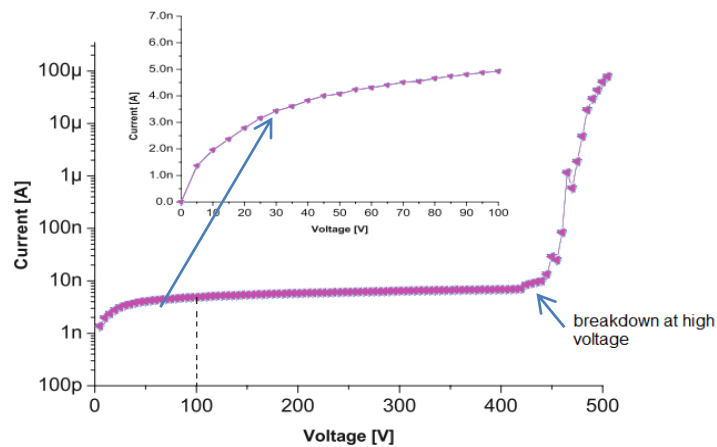


Figure 4.7: The plot shows the current-voltage for a silicon diode in the reverse bias directions. The expanded view between 0 to 100 V shows that $I \propto \sqrt{V}$, while from 0 to 500 V shows the full scan and the breakdown at high voltage.

4.4 Charged particle interaction with silicon

When a charged particle (protons, alpha particles, atomic ions) passes through a semiconductor material, free charges are generated because of ionization. The mean

energy loss per distance travelled by a charged particle in a material medium is described by the Bethe-Bloch formula [32].

$$\frac{dE}{dx} = 4\pi N_A r_e^2 m_e c^2 Z^2 \frac{Z}{A \beta^2} \left[\frac{1}{2} \ln \left(\frac{2m_e c^2 \beta^2 \gamma^2 T_{max}}{I^2} \right) - \beta^2 - \frac{\delta(\gamma)}{2} \right] \quad (4.22)$$

where z is the charge of the incident particle, T_{max} the maximum kinetic energy which can be transferable to a free electron in a single collision, I is the mean excitation energy, which is a characteristic ionization constant depending on the material, Z is the atomic number of absorber, A the atomic mass of absorber, N_A is the Avogadro's number, m_e is the electron mass, c is the speed of light, r_e is the classical electron radius, also known as the Lorentz radius, $\beta = v/c$, v is the speed of the charged particle, $\gamma = \frac{1}{\sqrt{1-\beta^2}}$ is Lorentz factor, and δ the density effect correction to ionization energy loss.

The function of average energy loss for muons (charged particle) traversing in copper is shown in Figure 4.8. The most essential part about the plot is that the minimum ionization takes place at $\beta\gamma$ of approximately 3 or 3.5 MeV which is the minimum deposited energy. This information is very important because every detector must keep the noise well below the energy of the Minimum Ionizing Particles (MIPs). For a MIP the average energy loss at the minimum:

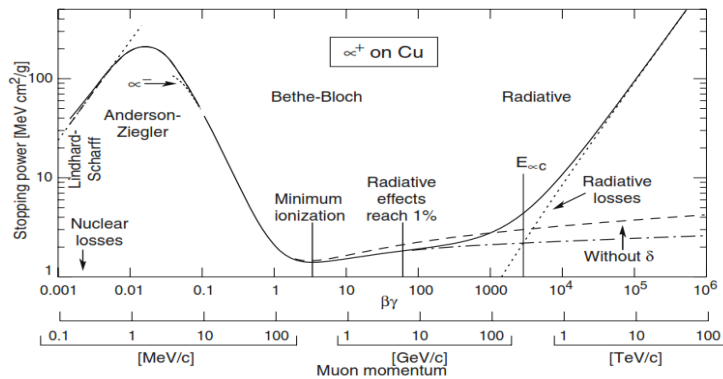


Figure 4. 8: The average stopping power $\langle dE/dx \rangle$ for muons traversing on copper material is shown; likewise, the correction to the Bethe-Bloch formula is illustrated. Therefore, it can be said that is the general principle of all ionizing detectors.

$$\left. \frac{dE}{dx} \right|_{min} = 1.664 \text{ MeV g}^{-1} \text{ cm}^2$$

The fluctuations in the energy loss were investigated in detail by Landau [33]. He found the number of collisions in a material medium, as well as the energy transfer by scattering, vary. The first case can be described through the Poisson distribution, while the second is described by the "straggling function" deduced by Landau. In the δ -rays or δ -electrons, the transferred energy is large, where the δ -electrons are responsible for the asymmetric long tail in the Landau distribution due to the bigger accumulation of charge. Likewise, the most probable value (MPV) of energy transfer is about 30% lower than the average value. In the case of silicon, the average energy required for the creation of electrons and holes pair in the semiconductor is about 3.6 eV, which is three times larger than the silicon crystal band gap of 1.12 eV, the remaining energy is used for the creation of the photon. The MPV in electrons and holes pair creation in 1 μm of silicon is 76, while the mean value is 108. Figure 4.9 shows the Landau distribution for this specific case.

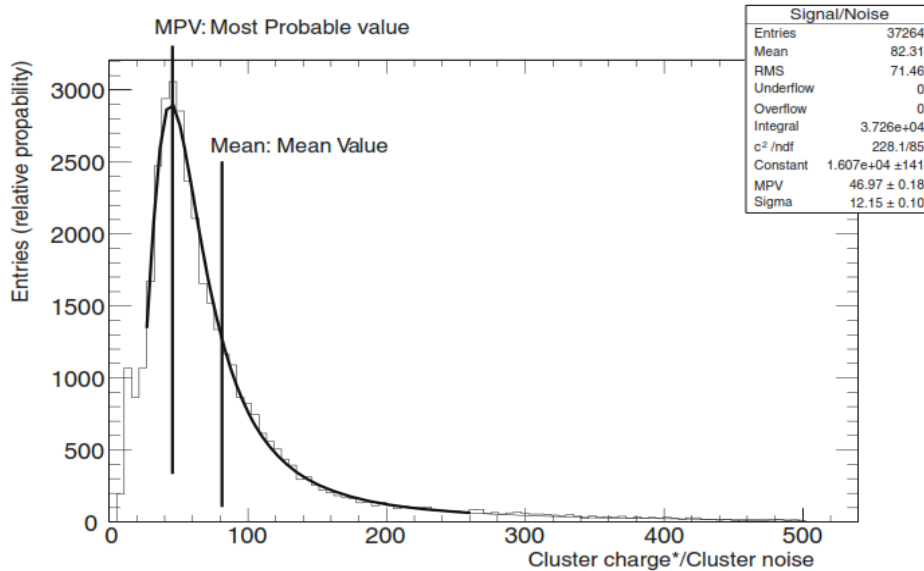


Figure 4.9: The Landau distribution for an ionized charge over 500 μm silicon from a cosmic particle (\sim MIP) arriving at an incident angle with 3.8 T magnetic field.

4.5 Working Principle of an AC – coupled silicon as a Tracking Device

The working principle of an AC-coupled silicon is shown in Figure 4.10. When an ionizing particle crosses through the fully depleted silicon n -doped slice, the holes and electrons generated are drifted in opposite directions due to the presence of the electric field created by the depletion voltage. The holes drift towards the p^+ doped strips, while the electrons towards n^+ backplane [34]. The collected charge on each of doped strips goes via the aluminum readout strips to the charge preamplifier of the readout chip.

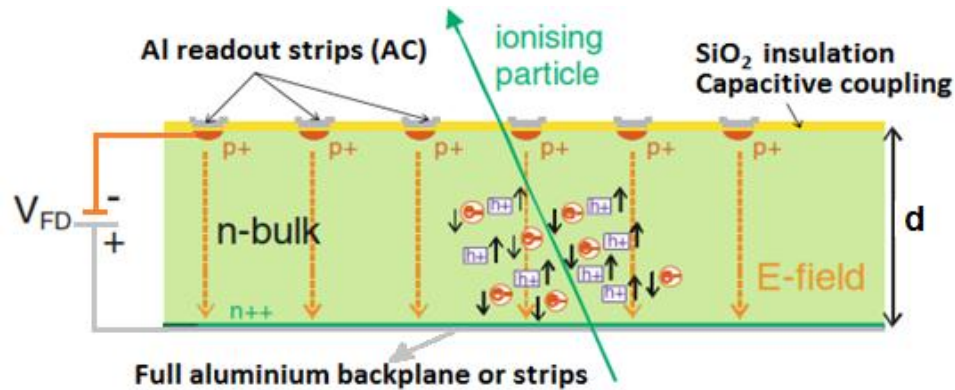


Figure 4.10: The working principle of an AC-coupled silicon microstrip detector. The holes are collected by p^+ strips implants in a n – bulk silicon.

The maximum time available for the lateral drift is the necessary time to travel the full volume, the mathematical expression is: $t_{e,h} = d/v_{e,d} = d/\mu_{e,h}E$. On other hand, the diffusion is calculated as $\sqrt{2Dt}$, where the diffusion constant $D = \mu k_B T/q$. The diffusion constant depends on the temperature. The diffusion of electrons and holes is the same because the parameter μ gets canceled.

The best location for tracks is obtained in the middle of two strip because the charge is shared equally and the effect of noise is small, but the signal of tracks near a strip has low localization properties. This is due to the remaining small signal on the neighboring strips being below the noise level. Additional intermediate implant strips between the readout strips improve the resolution through capacitive coupling, where this technique

helps to have an adequate position resolution. The resolution $\sigma_x \propto \frac{\text{pitch}}{\text{signal/noise}}$. The position resolution is given by:

$$\sigma_x \approx \frac{p}{\sqrt{12}} \quad (4.23)$$

In the silicon detector silicon oxide is used as an insulator. It has high temperature stability (1600 °C) is chemically inert. It has a high dielectric strength or it can be said that is a near-perfect dielectric because it has a relatively wide band gap, which makes it an excellent insulator, and has a high breakdown field strength. The SiO_2 can be used as a blocking material with the aim of making ion implantation or diffusion of unwanted impurities. It is easily deposited for different materials and grown thermally on silicon wafers, making it the most essential in the fabrication of many semiconductor devices.

4.6 Radiation Damage in Silicon Detector Devices

Bulk damage: When a particle traverses on the silicon detector devices, these can ionize the lattice and also interact with the atomic bodies through the electromagnetic and strong forces. Due to these effects, atoms are displaced from their original position, and can create interstitials I , vacancies V , and a lot of complex constructs, di-vacancies V_2 or triple-vacancies V_3 , and di-interstitials I_2 . These defects basically deform the lattice. These defects are shown in Figure 4.11. On the other hand, diffusing silicon atoms or vacancies often combine with impurity atoms; for example, oxygen, phosphorus or carbon [35].

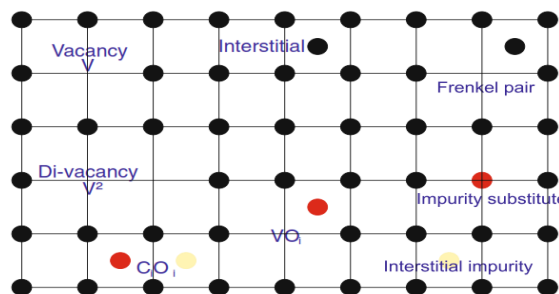


Figure 4.11: Displacements in silicon lattice after collision with traversing particles.

Leakage Currents: Mid gap defects of silicon detectors often occur during radiation. These cause a degradation of lifetime τ of electron and hole pairs and increase the dark current. It has been proved in many experiments that there is a linear behavior of the dark current with the fluence (φ_{eq}) as follows:

$$\frac{\Delta I}{V} = \alpha \varphi_{eq} \quad (4.24)$$

where V normalizes for a given volume, and α is known as the current-related damage rate. The leakage current is also temperature dependent: $I \propto T^2 e^{-\frac{E_g}{2kT}}$, where E_g is the band gap, and k is the Boltzmann constant. The cooling of the irradiated sensor allows to keep the leakage current low. So, irradiated detectors in general should be always operated and stored at low temperatures.

Surface Damage: The surface damage describes all radiation-induced damage in the SiO_2 layer and in the $SiO_2 - Si$ interface. As the crystal structure of SiO_2 is highly irregular the displacement of single atoms due to irradiation does not present macroscopic changes, i.e., the damage is generated by ionization not atomic displacement. In the silicon bulk material, creation of electron and hole pairs are not fully reversible in the insulator, this depends on the quality of the oxide used, where recombination can vary to a greater percent. However, generated charge carriers can be captured by existing defects because the band gaps are larger in oxide and nitride layers.

The main cause of radiation damage in the electronic circuits is the increase of transistor threshold voltage V_{thr} and leakage current. The threshold voltage increment is due to the screening effect of the oxide charge concentration. The shift of V_{thr} is proportional to power n of the oxide thickness, d_{ox} :

$$V_{thr} \propto d_{ox}^n$$

where n depends on the processes used to the grow the oxide and thickness. The measured value of n is in the range of 1 – 3. The increase leakage current is induced by the traps which act as a mid-bandgap level that introduces recombination centers which allows decreasing lifetime.

Chapter 5

Material and Methods

In this chapter, we describe how the data is generated and collected for the purpose of characterizing the 3D sensors under study. The characterization was performed at the Fermilab Test Beam Facility (FTBF) at the Fermi National Accelerator Laboratory using the Silicon Pixel Telescope. The performance of the Detector Under Test (DUT), which in this study are the sensors 56B(2E) and 56D(3E), is measured using a set of well reconstructed beam tracks. The (DUT) is placed in the middle of the pixel-based telescope planes of Silicon Pixel Telescope. The telescope has been designed to achieve an optimal spatial resolution for the reconstructed tracks in order to obtain the best precision of the telescope track projections on the DUTs. For this study, a beam of 120 GeV protons was used. The beam is resonantly extracted in a slow spill for each Fermilab Main Injector cycle delivering a single 4.2-second-long spill per minute. The primary beam (bunched at 53 MHz) consists of high energy protons (120 GeV) at variable intensities between 1 and 300 kHz . The beam can also be targeted to create secondary particle beams of pions, muons or electrons with energies down to about 1 GeV. The proton beam has limited multiple Coulomb scattering effects at 120 GeV and one can determine the precise time localization of the incoming protons. The event time-window is within $\sim 38\text{ nsec}$ and a fast readout system allows to accumulate up to 600,000 beam tracks per minute during 4.2 second spill. One can measure the position and energy of the incident beam using facility instrumentation. Four pre-installed scintillation counters give rough beam position, a lead glass calorimeters measure the beam energy to a precision of $\sim 3\%$, two time-of-flight detectors can be set up for particle identification, and finally a silicon pixel telescope provides a precision position measurement of less than $6\text{ }\mu\text{m}$ using the primary 120 GeV proton beam.

5.1 Silicon Pixel Telescope

The telescope is built from the Phase-0 silicon pixel modules of various types in several planes and provides precision tracking information of particle impact point on a test device (3D sensors for Phase-2 in this case). One can fully characterizing the test devices in terms of parameters like tracking efficiency, charge collection and spatial resolution. The telescope is placed along the beam line and instrumented with eight detector planes encased in a carbon fiber frame. Four of the eight telescope planes use modules composed of six 2x3 Read Out Chips (ROCs). In a 2x3 module, 6 ROCs are bump bonded in 2 rows of 3 ROCs to a single sensor. The ROCs used are PSI46V2 which were used in the Phase-0 Pixel Detector. The other four planes use 2x4 type modules. Each ROC reads an array of 52×80 sensor pixel cells, where each pixel cell size is $100 \times 150 \times 285 \mu\text{m}^3$ where $285 \mu\text{m}$ is the thickness of the sensor pixel. The pixels at the edge columns and upper row have sizes $100 \times 300 \times 285 \mu\text{m}^3$ and $200 \times 150 \times 285 \mu\text{m}^3$, respectively. The total active area for a 2x4 module is $1.62 \times 3.24 \text{ cm}^2$ while the 2x3 module has a total active area of $1.62 \times 2.43 \text{ cm}^2$. The eight planes are arranged in two stations with a section available in between for the DUT. The DUT is considered as a separate third station itself. The telescope frame is covered by a mylar anti-static layer with the aim of keeping the detector dark. Figure 5.1 below shows the three-dimensional schematic view of the geometry of the pixel telescope. Of the three coordinate axes the Y-axis points to the ceiling whereas Z axis is along the beamline.

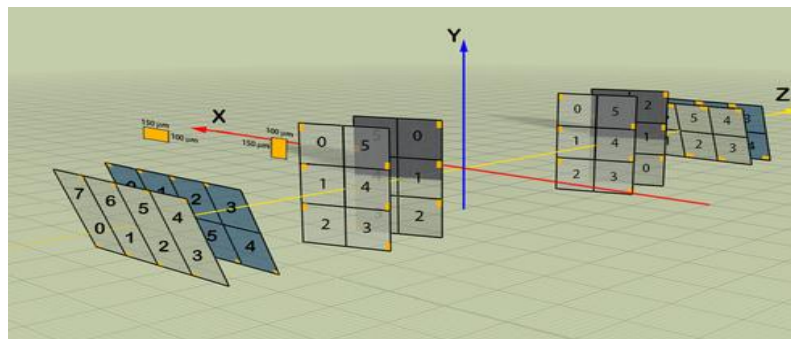


Figure 5.1: 3-dimensional schematic of the pixel telescope.

An improvement in spatial resolution is achieved by tilting the pixel modules by 25° that leads to charge sharing and hence maximizing the charge clusters across two adjacent pixel hits. The four 2×4 planes are tilted around the X axis with the long pixel side oriented in the X direction and the four 2×3 planes are tilted around the Y axis with the long pixel side oriented in the Y direction.

The trigger to read the data out is provided by a coincidence signal generated from three scintillation counters placed behind the telescope. The trigger signal opens a small time window in which the data acquisition system collects and sends data from the detectors to the storage computer. The data from each readout chip are tagged such that the data from all the detectors have the same time stamp. The hits that share the same trigger count are identified as an event. An event may contain hit data associated with one or more particle tracks passing through the telescope. To keep the readout chips clock synchronized with the particle beam, the accelerator clock signal is fed into one of the stations and then redistributed to the other stations. The PSI46v2 ROC is designed to run at a maximum frequency of 40 MHz . However, the Main Injector accelerator frequency is 53 MHz . To allow the detector to work properly and remain synchronized with the beam, the clock distributed to the stations runs at 26.5 MHz (half of the Main Injector frequency). A picture of the test beam apparatus is shown in Figure 5.2

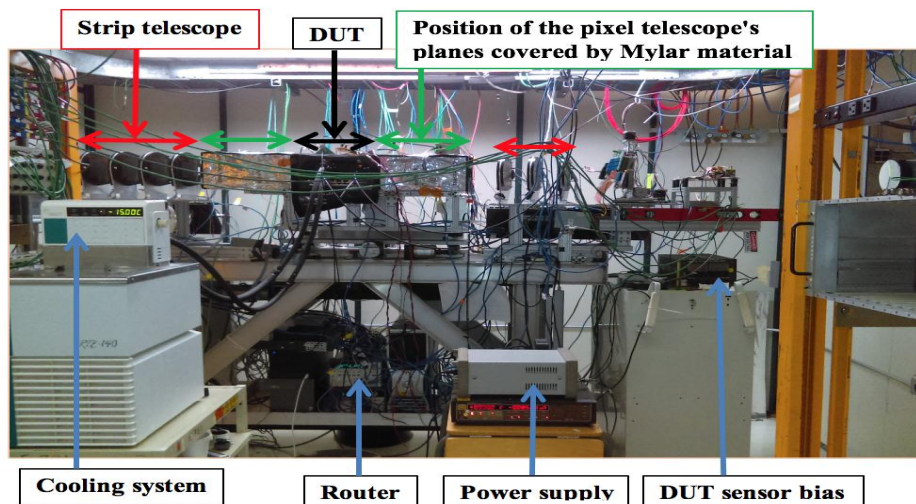


Figure 5.2: The experimental set up at Fermilab.

5.2 Data Acquisition Apparatus

The Data Acquisition (DAQ) hardware is based on the CAPTAN (Compact And Programmable daTa Acquisition Node) [36] system developed at Fermilab. This is a flexible and versatile data acquisition system designed to meet the readout and control demands of a variety of pixel and strip detectors for high energy physics applications. The system consists of three CAPTAN nodes, one for each of three stations used in our setup. The node consists of a stack of different function boards with a vertical bus for high-speed data exchange and features a Gigabit Ethernet Link (GEL) for high-speed communication through. The node is connected to a gigabit Ethernet router which in turn is connected via an Ethernet cable to a computer placed in the control. The telescope apparatus can be controlled remotely via a Graphical User Interface (GUI), on this computer.

The master node in the CAPTAN system connects to the DUTs and receives the accelerator clock and the trigger from the scintillators and redistributes them to the other two nodes after having reduced the clock to half the frequency (26.5 MHz). In each node, the data from ROCs are received by the DCB (Data Conversion Board). The data is then digitized and sent to the FPGA through the vertical bus. The formatted data are then transferred to the control room via gigabit Ethernet connection. A schematic of the DAQ is shown in Figure 5.3.

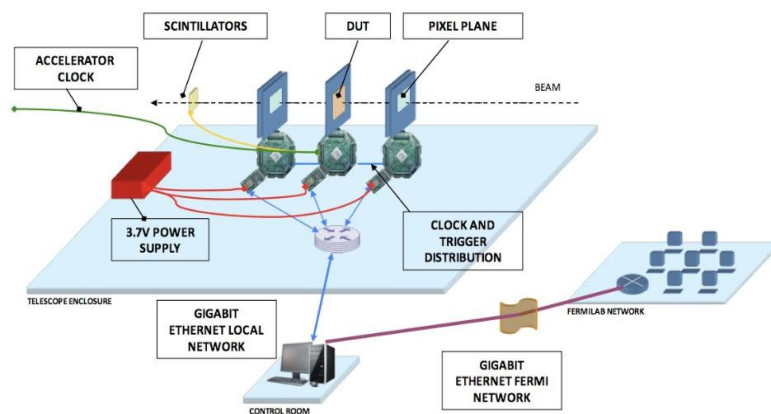


Figure 5.3: The telescope readout system based on CAPTAN hardware.

The data from each node is saved in separate directories for each Run. At the end of a Run, the correlated (marked with the same trigger count) data from every pixel plane is saved and thus forms the data from an event. The data from all events in a run are merged into a single binary and saved to a disk. A GUI allows the user to set up the readout chips, trigger and clock system, run calibration procedures, as well as to start or stop the data acquisition and stores data to disk. A user can also visualize the merged telescope data in three dimensions as shown in Figure 5.4. This is critical for the data acquisition process since it allows the user to quickly check the quality of the data. For example, using this feature one can assess if the beam is properly positioned on the detectors.

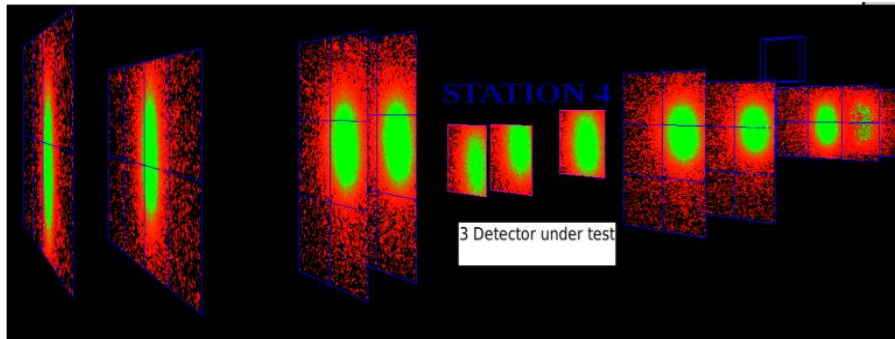


Figure 5.4: Data visualization the telescope.

5.3 Tracking Software

The goal of this work is to characterize the performance of the 3D Detectors (DUTs). The silicon pixel telescope used for this purpose is designed to achieve an optimal spatial resolution for the reconstructed tracks so that one can obtain the best precision of its track projections on the DUTs. A correct track reconstruction requires a suitable alignment of the telescope planes and for this purpose a special C++ software package called **Monicelli** has been designed by the Università degli Studi di Milano-Bicocca (Milan, Italy). It provides an interactive GUI to manually handle an appropriate iterative procedure for alignment producing a large number of distributions to control its progress

and status. The track reconstruction and iterative alignment operations represent the preliminary steps of the subsequent analysis on DUTs and must be performed with carefully. Figure 5.5 illustrates a snapshot of the Graphical User Interface (GUI) with their respective components [37].

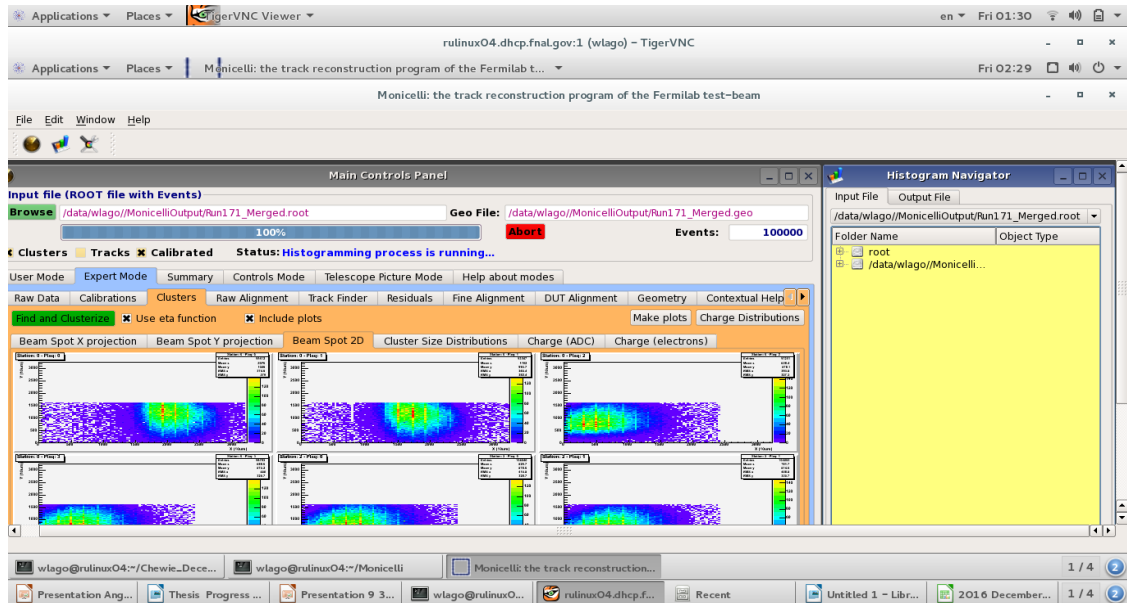


Figure 5.5: Graphical User Interface (GUI) of Monicelli. The left top shows all the components that allows all alignment operations while on the right side shows a histogram navigator used to view the different control histograms created during the alignment phases.

5.3.1 Track reconstruction

The track reconstruction consists of multiple steps described below:

Event reconstruction: This step involves building events from raw binary files. The information contained in the binary files are decoded: for each event, the ADC value of every hit is associated with a row and a column belonging of a detector plane according to the telescope information provided by an XML detector geometry file. Two output files are created on disk: one with decoded events data and the other one with the associated geometry. A set of histograms allow users to cross-check the geometry

information provided to the program as well as to check that the beam is roughly centered on all the detectors planes. Figure 5.6 shows the beam spot on a 2x4 pixel plane (2x4 translates to $2 \times 80 = 160$ rows and $4 \times 52 = 208$ double columns).

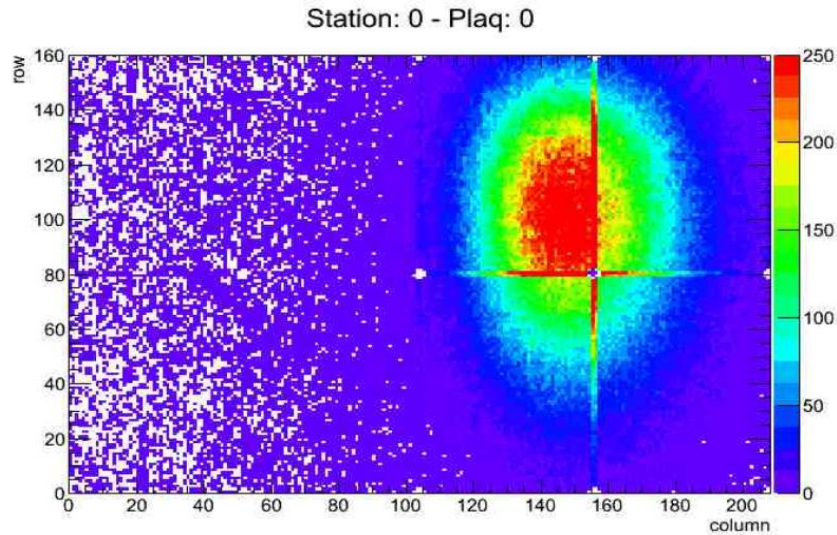


Figure 5.6: Beam spot on 2x4 detector plane of the telescope.

Clusterization: In this step, one computes the space coordinates of all the hits on each detector by organizing the adjacent fired pixels into clusters. The telescope detectors are tilted by 25° around X or Y axis and hits involving one pixel, two adjacent pixels and four adjacent (2×2) are interesting (shown in Fig. 5.7), while some other cluster types arising from a variety of reasons (dead pixels, threshold issues, δ -rays etc.) are considered unsuitable for alignment and analysis. The cluster coordinates are expressed as local coordinates (x, y) , to distinguish them from the laboratory system coordinates X and Y , of the detector plane they belong to.

When only a single pixel is fired, the space coordinates associated with that hit are those of the geometrical center of the cell with a resolution given by $p/\sqrt{12}$ where p is the pixel pitch ($100 \times 150 \mu m^2$). If a cluster with size larger than one is generated, the hit coordinate is determined by weighing the collected charge between the cells considering the expected track impact angle (see reference [17]).

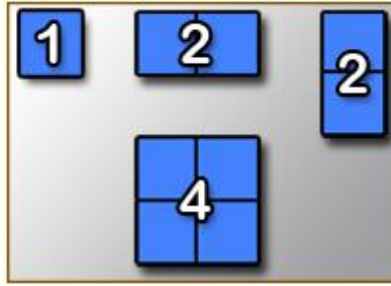


Figure 5.7: The picture below shows the geometrical arrangement of the considered clusters (1, 2, 2x2 pixels).

Track finding: The reconstructed clusters above are next used to find track candidates. Any combination of cluster hits on the first and the last plane of the telescope are joined by a straight line, looking for confirming hits on the intermediate detector planes. The nearest cluster hit to the intersection point of the line with every detector plane within an adjustable window is selected. A minimum of 6 hits is required to define a track candidate. Other track candidates can reuse the clusters during this operation. The hits associated to each track candidate are fitted to a straight line using the least square method. This method is called “road search”. When all track candidates in an event are reconstructed and fitted, they are sorted by total number of hits and χ^2 /DoF. For all the track candidates, starting from the track with the highest number of hits and the lowest χ^2 /DoF, all hits belonging to the track, that have been associated to other track candidates, are removed from them and those tracks are refitted and resorted again. The quality of the reconstruction can be tested by observing the residuals. Residuals are the difference between the measured and the predicted coordinate.

5.3.2 Alignment Procedure and Results

Alignment Concept: The initial physical location of the telescope planes set by the XML geometry is not known to the precision of $\sim \mu m$ and as a result tracks reconstructed above from the data collected are used to measure the plane positions. The alignment method [38] for the telescope planes is based on a standard χ^2 successive-

approximation minimization of the unconstrained residuals on each plane. An unconstrained residual implies that the point considered on the detector plane was not used in track finding. This makes the residual distribution less biased and the error on its position would not affect the track reconstruction. It returns all the six geometrical degrees of freedom of each plane. Only the tracks having hits on all the planes are considered in this process.

Alignment Method: The alignment requires an initial set of track candidates to start with preliminary or raw alignment of the telescope detectors. This first-order approximation is obtained by a relative transverse alignment of the beam profiles on each detector, equalizing the X and Y coordinate of the beam center for all the planes. The X and Y projections of the beam spot are fitted with a Gaussian function to obtain the space coordinates of the beam spot centers on each telescope detector. Then an initial suitable sample of tracks is found through a “road search” as described before, using a large enough window of tolerance $\sim 1000 \mu m$. A finer translation alignment is obtained by looking at the mean values of the X and Y unconstrained residuals on each plane (at this stage they are typically off from zero by a few hundred microns). For each coordinate, the planes are moved at a distance equal to the residuals mean value, to set it at 0 (the direction where the planes are moved to depends upon the sign of the residuals mean value). The X and Y detector positions in the geometry file are automatically updated with the measured translation corrections. Now a new “road search” is performed with a thinner fiducial window (usually $250 \mu m$) and more improved sample of tracks is obtained and the increased track quality can be checked from the χ^2 / DoF , distribution.

Now we apply cuts on this improved sample requiring, for instance: $\chi^2 / DoF < 10$, 8 hits per track (i.e. a hit on every telescope plane) and 1 cluster hit per plane. With these cuts applied one can iterate the finer alignment step as described in previous paragraph to obtain a new sample of tracks. With these new sample an iterative alignment algorithm that exploits least-squares minimization to compute the first order roto-translational corrections is applied. In this algorithm, a sample made of tracks with 8 hits, each of maximum cluster-size 2, is selected to compute and minimize the x and

y (local coordinates) unconstrained residuals on each telescope detector. In this first iterative minimization run, the geometry parameters of the first and the last detector along Z direction are kept fixed. Furthermore, if the angular dispersion of the beam tracks is tiny (~ 0.1 mrad), even the Z positions of the other detectors must be fixed since the fit would be insensitive to any shift in Z (the derivatives of χ^2 with respect to these Z positions would practically be zero). At the end of each iteration, a new “road search” is performed with the updates to provide the next iteration with an improved sample of tracks. Typically, 5 iterations are enough to converge to stable values of the parameters. At the end of this process, pull, unconstrained residuals and correlation distributions are produced to check the alignment progress. Finally, a second iterative minimization run is executed releasing also the geometry parameters of the first and last planes while keeping fixed the Z positions of all the telescope planes. Usually 10 iterations are set with a χ^2 /DoF cut of 10. The resulting updated parameters constitute the final alignment geometry.

Alignment Results: The outcome of the above alignment procedure is shown and discussed in this section. The results shown below are for a given data run. Figure 5.8 shows the x and y unconstrained residual distributions. The unconstrained residual for a detector plane is defined as the distances between the coordinates of the measured hit and the coordinates of the predicted point on that plane obtained by the fit of all other hits associated to that track. Therefore, when computing the residual on a detector, its hit is removed from the track. Figure 5.8a shows the residual spectra for a detector plane along the non-tilted coordinate (pitch = $150 \mu m$) and Figure 5.8b it is wider non-Gaussian type whereas the one along the tilted coordinate (pitch = $100 \mu m$) has a narrow shape. The wider shape is caused by the most probable single-hit events, resulting in distributions with RMS of about $150/\sqrt{12} \mu m$. In the second case the distribution is dominated by charge sharing between adjacent pixels along the coordinate that is measured with the best resolution, resulting in distributions with RMS of about $30 \mu m$. Alignment quality can also be checked from the x and y pull distribution shown in Figure 5.9. The pull ($p_{x,i}, p_{y,i}$) on an ith detector plane is defined as:

$$p_{x,i} = \frac{x_{m,i} - x_{p,i}}{\sqrt{\sigma_{x_{m,i}}^2 + \sigma_{x_{p,i}}^2}}, \quad p_{y,i} = \frac{y_{m,i} - y_{p,i}}{\sqrt{\sigma_{y_{m,i}}^2 + \sigma_{y_{p,i}}^2}}$$

The numerator in above equation is the unconstrained residuals and the denominator is the square-root of the sum of the squared errors associated to the measured hit coordinates $(x_{m,i}, y_{m,i})$ and the squared errors of the impact point $(x_{p,i}, y_{p,i})$ predicted by the track fit obtained excluding the hit on that plane.

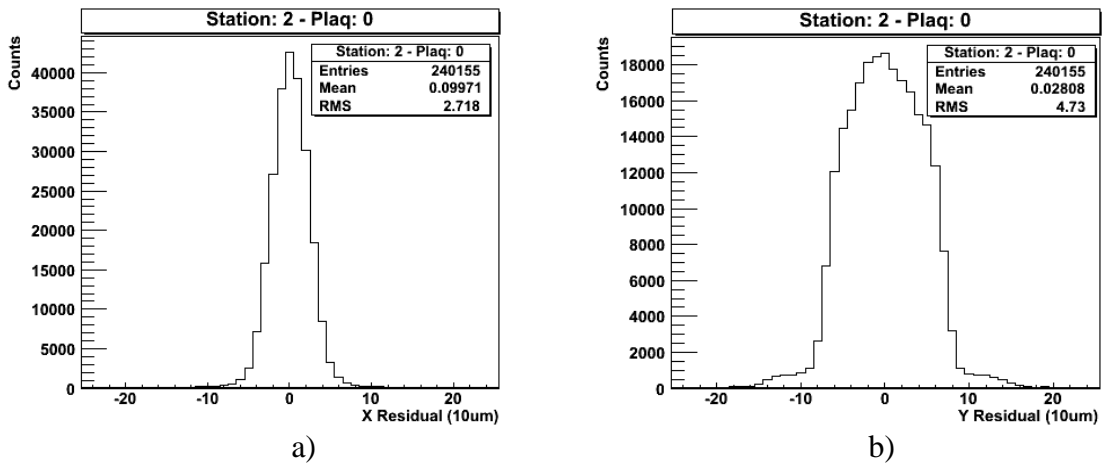


Figure 5.8: The x and y residual distributions of the telescope detector after having obtained a good alignment are shown. a) A narrow shape along the tilted that corresponds to a pitch of $100 \mu\text{m}$. b) A non-Gaussian shape along the non-tilted coordinate for a pitch of $150 \mu\text{m}$.

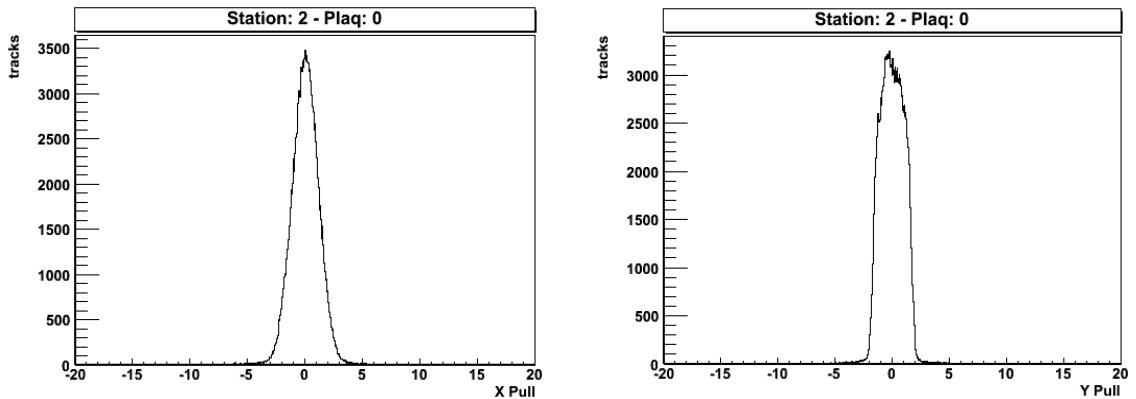


Figure 5.9: The x and y pull distributions for one station and plane of the telescope detectors.

The precision of the alignment is further investigated studying the plots of Figure 5.10 that shows the correlations between the unconstrained residuals and the impact point coordinates on the detector.

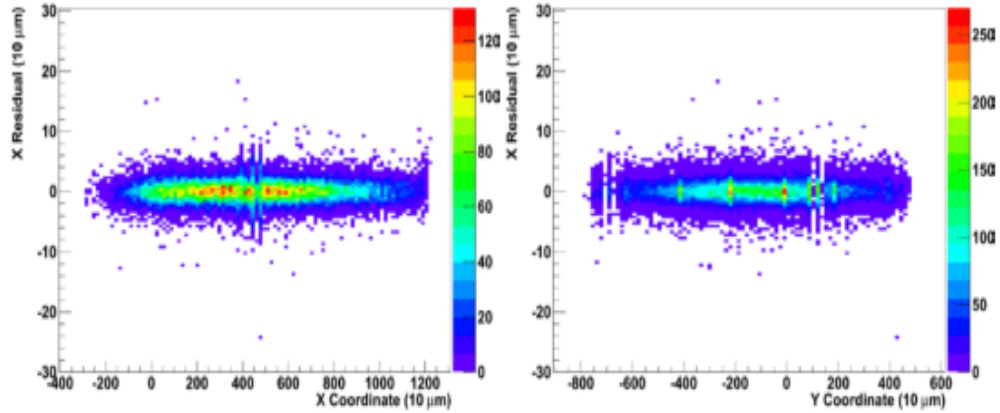


Figure 5.10: It is illustrated for one of the telescope detector the correlation between unconstrained residuals and impact point coordinate in one of the telescope detector.

For instance, the need for a further rotation of a detector around the Z axis should show up as a correlation in the plot of the distributions of the X residuals against the Y associated coordinates. On the other hand, correlations in the distributions of X residuals against X coordinates highlights the need for a further rotation of a detector around the Y . As the alignment procedure goes ahead the correlation plots are flattening and becomes as shown in the figures. The shape of the fitted track χ^2/DoF distribution in Figure 5.11 shows the quality of the tracks reconstructed with this alignment and efficiency of the alignment algorithm.

Figure 5.12 shows the X and Y slope distributions for 120 GeV proton tracks with a small angular dispersion of about 10^{-4} rad , resulting in a low resolving power for the determination of Z position correction. Figure 5.13 illustrates the transverse error on track fit at DUT Z position ($Z \approx 0$) for tracks with 8 hits. The best resolution reached by the telescope on the DUT is $\sim 5.5 \mu\text{m}$ in the X and Y coordinates, however, the bulk of tracks have resolutions greater than $6 \mu\text{m}$.

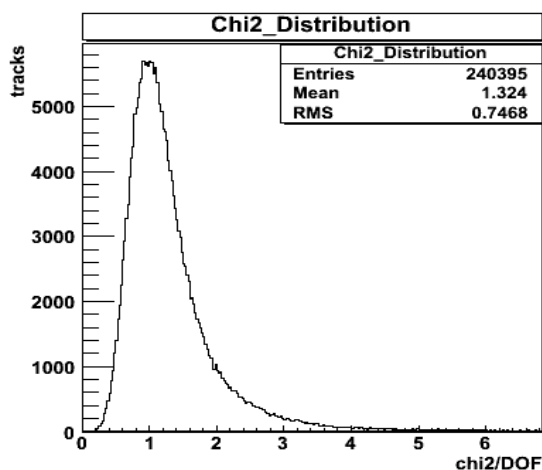


Figure 5.11: χ^2/DoF distribution after performing a complete alignment.

It is important to mention here that the sensor and ROC were bench tested before putting in the test beam. The sensor was characterized for IV curve, breakdown voltage and the ROC was characterized for determine the right values of the DAC registers to get the best voltage operating parameters. But these results are not discussed here and are not the focus of thesis work.

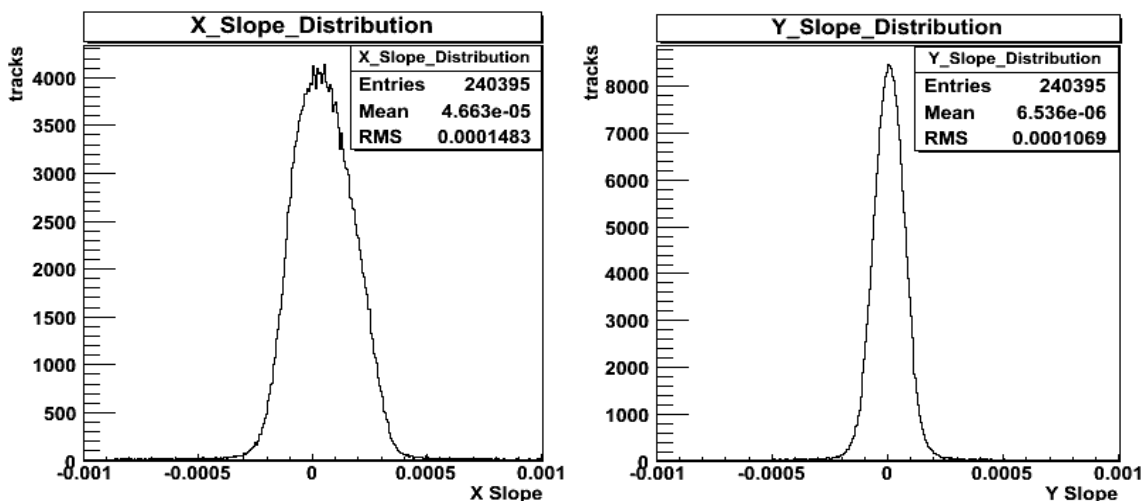


Figure 5.12: The plots show the slope distribution of the 120 GeV proton tracks for a small angular dispersion ($\sim 10^{-4}$ rad).

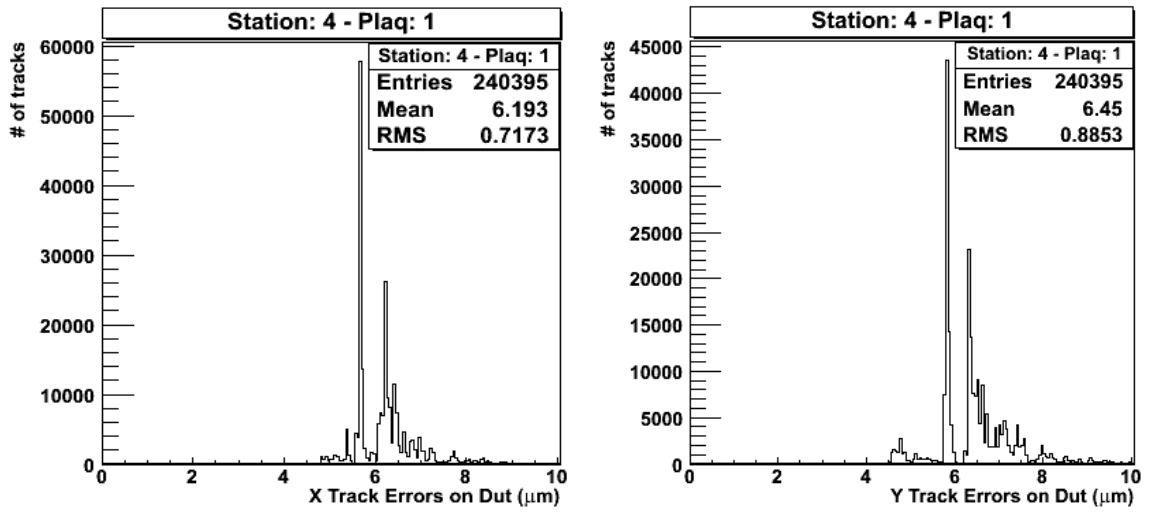


Figure 5.13: It is illustrated the error distribution on track fit at DUT Z position after performing alignment. The discrete peaks are due to the combinations of different hit resolution which may be associated to the tracks.

Chapter 6

Test beam results

In this chapter, results on the characterization of the 3D sensors in the test beam are presented. The detector efficiency, the charge collection properties and spatial resolution are determined. These 3D detectors are un-irradiated sensors. Once the calibration process is completed two very important operating parameters: threshold and bias voltage are optimized. The optimization of these parameters is performed varying them until the sensor detection efficiency is maximized. The efficiency is defined as the ratio between the number of tracks reconstructed by the telescope and having a corresponding hit on the detector and the total number of tracks reconstructed by the telescope and crossing the detector. As a reminder, **Dut0** and **Dut1** in this chapter refers to **56D(3E)** and **56B(2E)** respectively. The rotation angle and bias voltage of the sensor is mentioned in the plots. As was mentioned in Chapter 3, three junction columns in 56(3E) and two junction columns in 56(2E) are shorted together to be able to bump bond to and match the PSI46dig readout chip which was the only one available at the time of this study. This means a cell size of $150 \mu\text{m} \times 100 \mu\text{m}$ in each type of sensor is mated to a channel on the PSI46dig.

6.1 Sensor efficiency

The efficiency is calculated as the number of tracks reconstructed by the telescope and having a corresponding hit on the detector, divided by the total number of tracks reconstructed by the telescope and crossing the detector. To reduce possible sources of inefficiency, that are not related to sensor's problems, it is necessary to introduce some precautions: first, to take into account the error on the track projection, a pixel is considered to be efficient if either the hit is found on the pixel pointed by the track or in one of its eight neighboring pixels; second, if the pixel pointed by the track does not have all the surrounding pixels alive, for example the pixels on the sensor's edge, then this event is excluded from the efficiency calculation. The last criteria are also useful to avoid possible inefficiencies caused by imperfect bonding or failing pixels in the ROC.

The efficiency map is shown in Figure 6.1. The computed efficiency values are very high and equal to 99.42% and 99.43% for 56D(3E) and 56B(2E) respectively. The map corresponds to the size of the sensor mated with one PSI46dig Readout chip. The ROC architecture is divided into 52 double columns and 80 rows of readout channels.

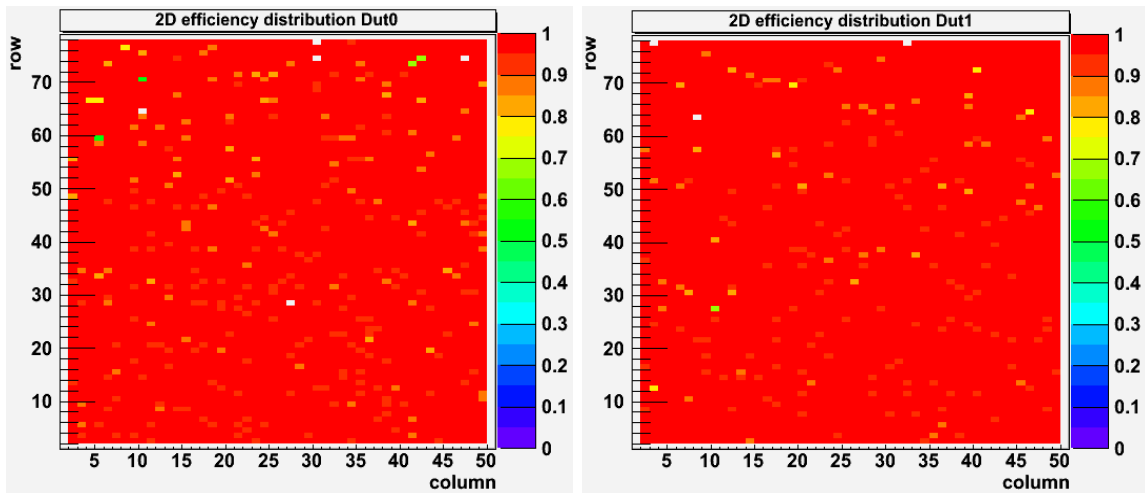


Figure 6.1: The efficiency map of 56D (Dut0, efficiency 99.43%) and 56B (Dut1, efficiency 99.42%) sensors at a 0-degree rotation angle and a bias voltage of 10V.

We also measured the efficiency at different voltages as shown in Figure 6.2. The efficiency is almost constant up to 70 V. Also at 5 V the efficiency is shown to decrease as this value of voltage is at the border line of full depletion of the sensor. Both sensor types are equally efficient.

We also studied the efficiency as a function of rotation angles around the Y-axis for angles of 0, 5 and 10 and found efficiency to be very high. Ability to operating 3D sensors at a lower voltage, as seen in the efficiency map above, is a big advantage compared to planar type. In a 3D sensor, the depletion region grows laterally between the columnar electrodes and, owing to the short inter-electrode spacing; the full depletion voltage is much smaller than that of planar sensors, which depends instead on the sensor thickness.

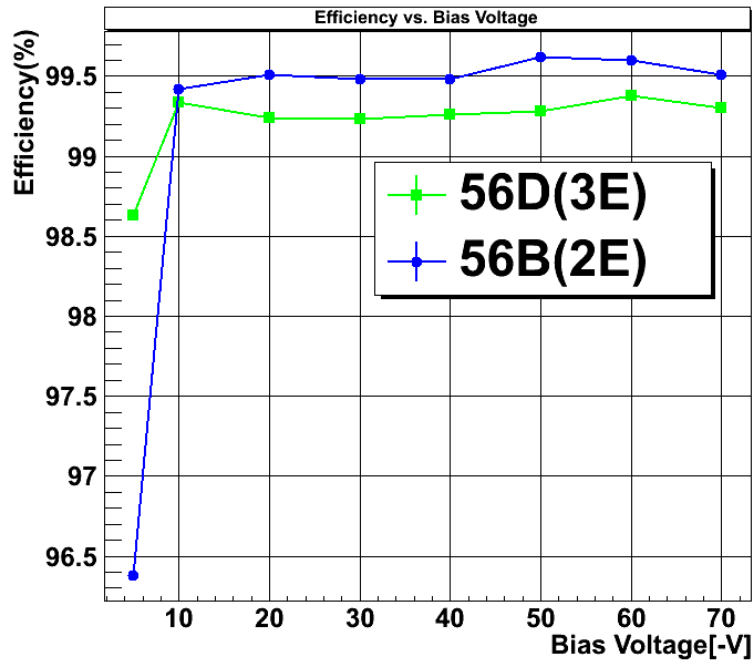


Figure 6.2: Sensor efficiency as a function of the bias voltage at 0-degree rotation.

6.2 Cell efficiency

We measure the cell efficiency of the sensors where cell is an area of size $100 \times 150 \mu\text{m}^2$ on the sensor that is bump bonded to a single readout channel. 3D silicon detectors are fabricated by the Deep Reactive-Ion-Etching (DRIE) technique which allows p- and n-type electrodes to be processed through the entire silicon substrate. Figure 6.3 (Right plots) shows the cell efficiency for both types of sensors. The entire cell area is highly efficient. The small decrease in full efficiency is partially explained by the electrodes being inactive volumes for tracks impinging orthogonal to the detector. The electrodes are $5 \mu\text{m}$ in diameter made of conductive polysilicon material which does not produce e/h pairs making the columns inefficient. This can be seen by comparing the left plots with right plots in Figure 6.3 where structures corresponding to the n+ columns in the middle of the sensor and to the p+ columns on the edges are visible. Figure 6.3 plots are made with sensor at 0-degree rotation and 20 V bias voltage.

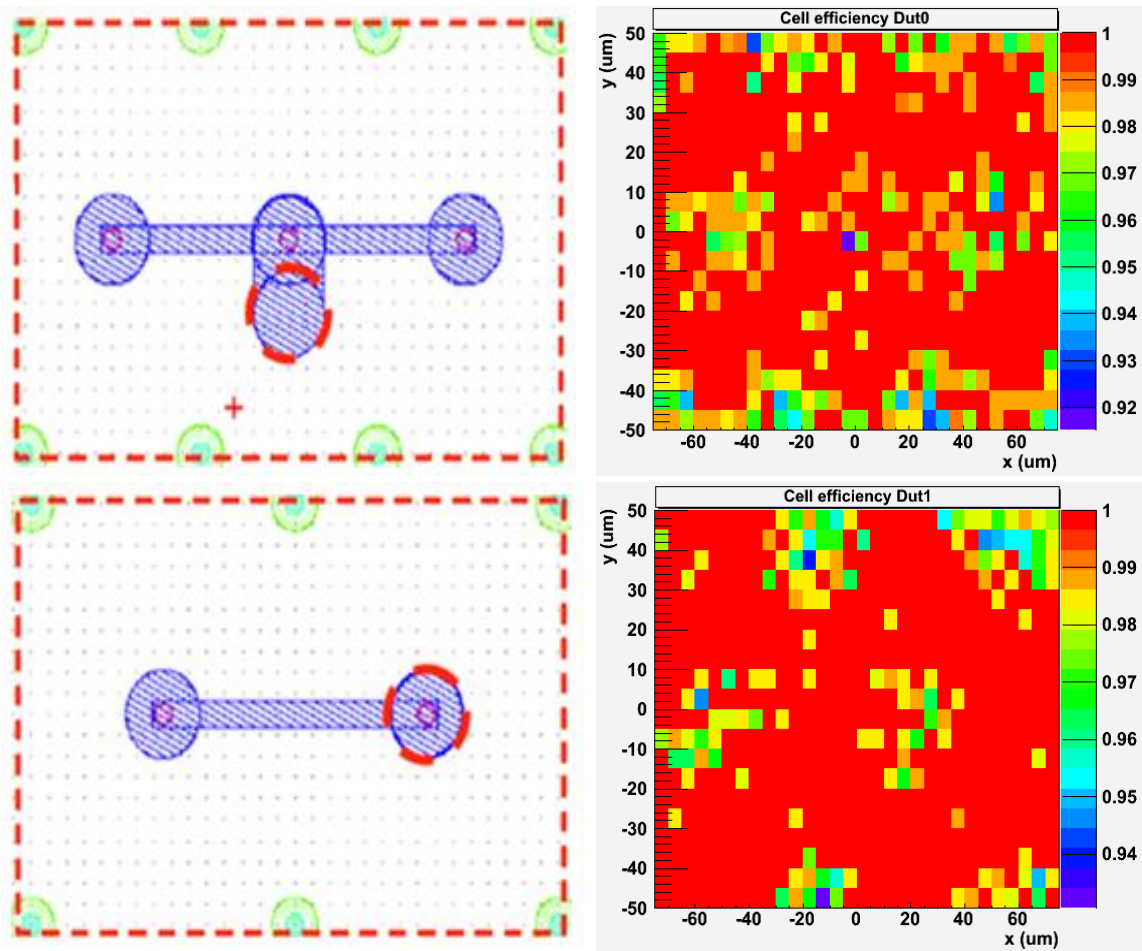


Figure 6.3: Cell efficiency: Top is 56D (3E) and Bottom is 56B(2E) sensors, both at 0-degrees and bias voltage of 20V.

Figure 6.4 shows the cell efficiency for 56D (3E) in a 3-dimensional view. Again, the pattern in the efficiency caused by the electrode inefficiency is clearly visible. When the detector is rotated by 5-degree, the effect of inefficiency for orthogonal tracks disappears due to more angled tracks and hence the electrode structure is not visible in the cell efficiency as can be seen in Figure 6.5.

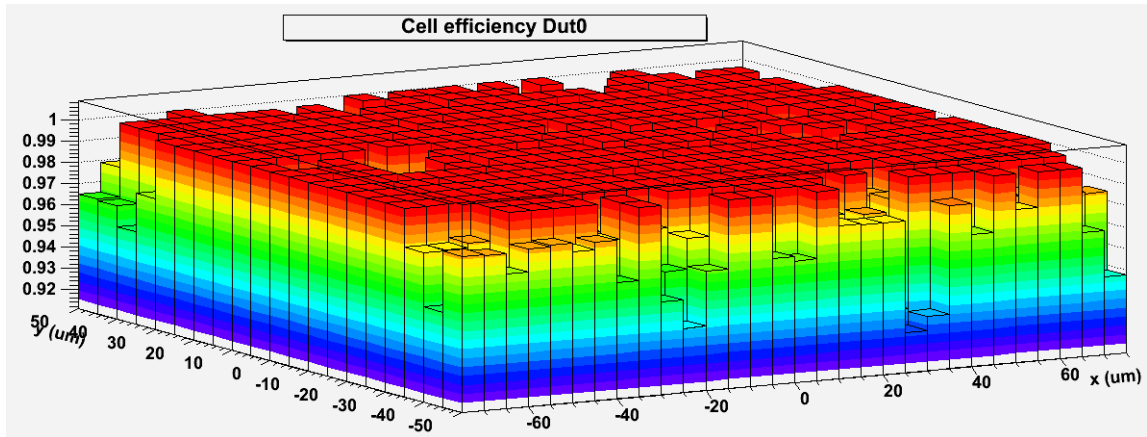


Figure 6.4: A three-dimensional view cell efficiency for the 56D (3E).

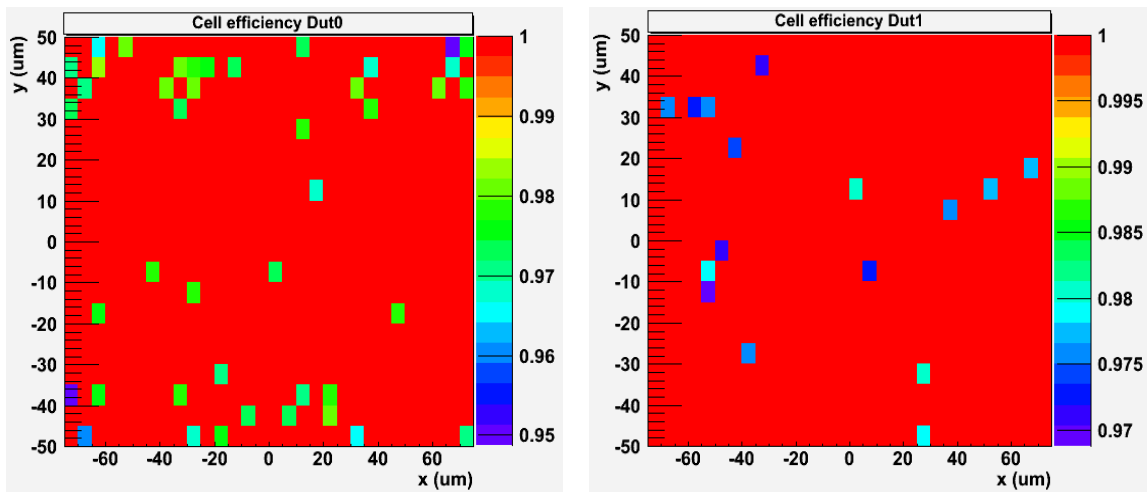


Figure 6.5: Cell efficiencies of 56D (3E) and 56B (2E) sensors at 5-degree rotation.

6.3 Charge collection

The average energy loss of charged particles when travelling through matter is described by the Bethe-Bloch relation and the fluctuations of energy loss by ionization of a charged particle in a thin layer of matter is described by the Landau distribution. It resembles a Gaussian distribution with a long upper tail, resulting from the small number of individual collisions, each with a small probability of transferring

comparatively large amounts of energy. This energy is deposited by a subsequent cascade. Its limit is the long tail, which theoretically extends to infinite energies, while the energy deposited by an incoming particle cannot exceed its own energy. Protons, Pions and other types of charged particles, which are in most cases close to MIPs (Minimum Ionizing Particles), all produce approximately Landau-distributed spectra when traversing the matter (in this case silicon sensor).

We measured the charged collected and its distribution is expected to follow a Landau distribution. Since the most probable number of charge carriers produced by a MIP in μm of silicon is about 70 both for electrons and holes and the sensors useful thickness of 120 microns thick, a Most Probable Value (MPV) of about 8400 electrons is expected.

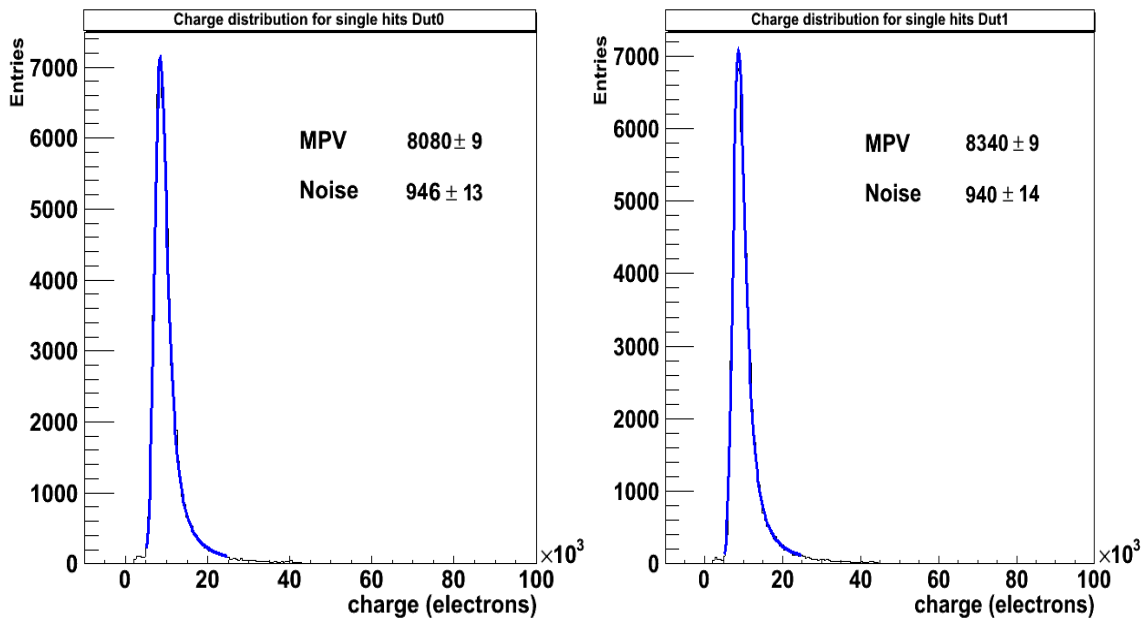


Figure 6.6: The charge distribution for the 56D (3E) and 56B (2E) sensors are shown. The bias voltage for both distributions is 40V and the 0-degree rotation angle.

Fig. 6.6 shows the histograms of the number of electrons (proportional to the charge) collected in single-hit events for sensor 56D (3E) (left plot) and 56B(2E) (right plot). The curves shown in the figures correspond to a fitting function consisting of a Landau

convoluted with a Gaussian. Due to the Landau's long tail, the MPV is a statistically more robust measure of the charge collected. As can be seen, this gives a very good fit to the data. The Gaussian models the noise in the system very well. The MPV is 8340e and 8080e and noise is 940e and 946e for 56B(2E) and 56D(3E), respectively. This gives a Signal/Noise of 8.9 and 8.5 for 56B(2E) and 56D(3E), respectively.

6.4 Cluster size

As mentioned before in 56D(3E) type sensor three electrodes are shorted and bump bonded to a single readout channel of PSI46dig and in 56B(2E) two electrodes are shorted and bump bonded to single readout channel of PSI46dig. This gives rise to a cell size of $100 \times 150 \mu m^2$. If a charge is shared it is shared between two cell sizes. Figure 6.7 shows the cluster size distribution for the two types of sensors.

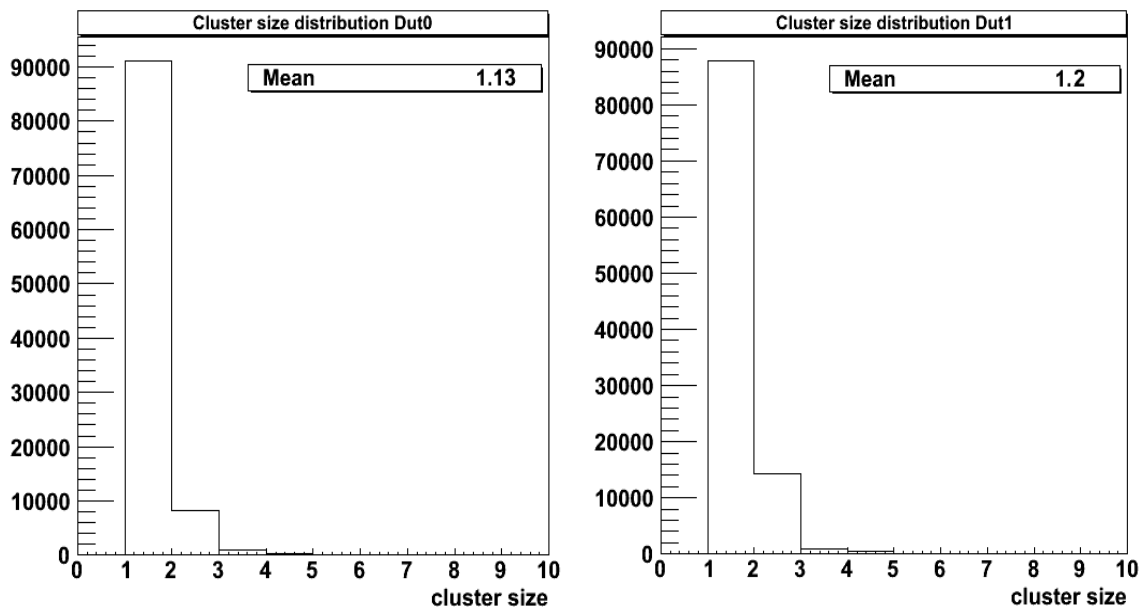


Figure 6.7: The cluster size distribution at 0-degree rotation angle and bias voltage of 10V.

Very few clusters of charge are spread over two or three pixels and the average cluster size is similar for the two sensors. The cluster size, as expected increases slightly with rotation as shown in Figure 6.8.

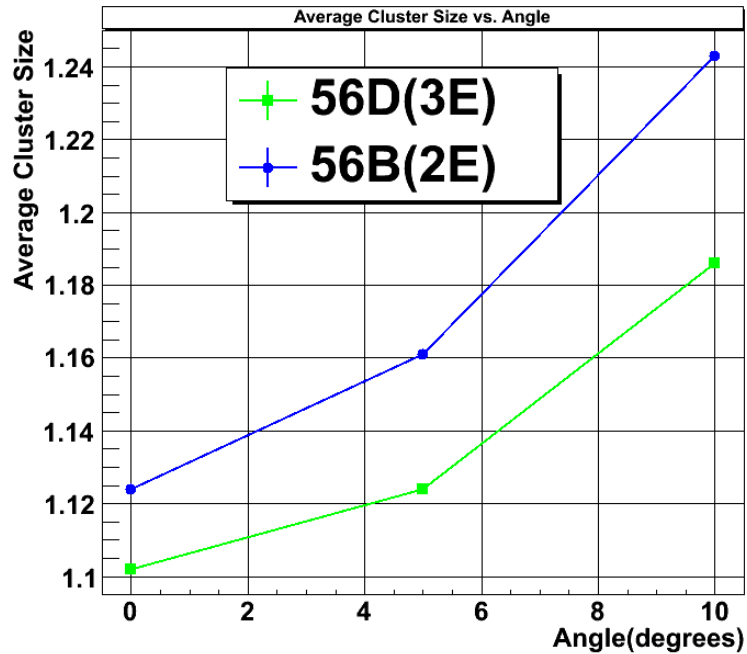


Figure 6.8: “Cluster size vs. angle for a bias voltage of 30V”.

6.5 Spatial Resolution

Determining the spatial resolution of the 3D sensor is the most important part of this study. The resolution should be small enough to sort out the vertices of the charged particle tracks with a Pileup of up to 200 at the HL-LHC by Phase CMS Phase-2 Pixel Detector. Both predicted and measured impact points are obtained for each of the two pixel coordinates. In the local reference frame of a single pixel, the coordinate along the $150 \mu m$ is labeled x and the one along the $100 \mu m$ is labeled y .

Measured Impact Point: It can be obtained using different techniques that are specific to the hit's cluster size. For clusters of size one the measured point is set at the center of the pixel. For example, for the standard pitch of $100 \mu m$, since the impact points are distributed uniformly, we expect the residuals distribution to be flat as shown in Figure 6.9 below. Hence the uncertainty associated should be equal to the pitch divided by $\sqrt{12}$ [see chapter 4].

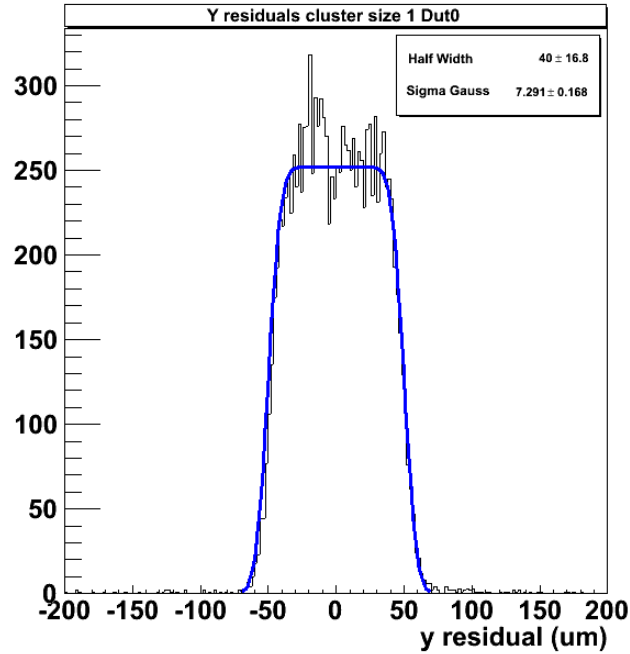


Figure 6. 9: Y residual cluster size 1 for 56D(3E).

For clusters of size two, the measured coordinate is calculated using asymmetry fit method. The charge asymmetry is defined, for clusters of size two, as the difference of the charge in the two pixels of the cluster, divided by the total cluster's charge as follows:

$$\eta = \frac{Q_{down} - Q_{up}}{Q_{down} + Q_{up}}$$

“up” and “down” are used as we are referring to the y coordinate. Asymmetry values are between -1, all the charge collected in the up" pixel, and +1, all the charge collected in the “down" pixel, with $\eta = 0$ meaning that the two pixels have the same amount of charge. The average values of the distance of the track impact point from the boundary of two adjacent pixels is computed for each η and a linear fit is performed and the measured impact point obtained as: $y_m = p_0 + p_1\eta$ where p_0 and p_1 are the intercept and the slope of the linear fit. Residuals based on this method are shown in the Figure 6.10 for cluster size 2 in the x coordinate and Figure 6.11 for y coordinate.

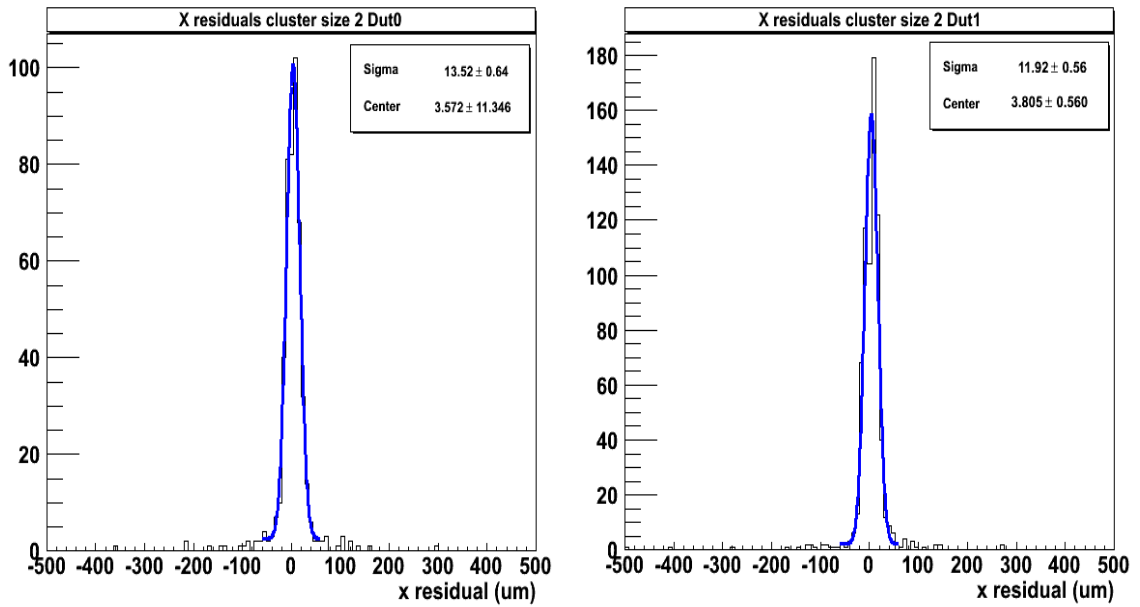


Figure 6. 10: X residual cluster size of 2: Left is 56D (3E) and right is 56B (2E).

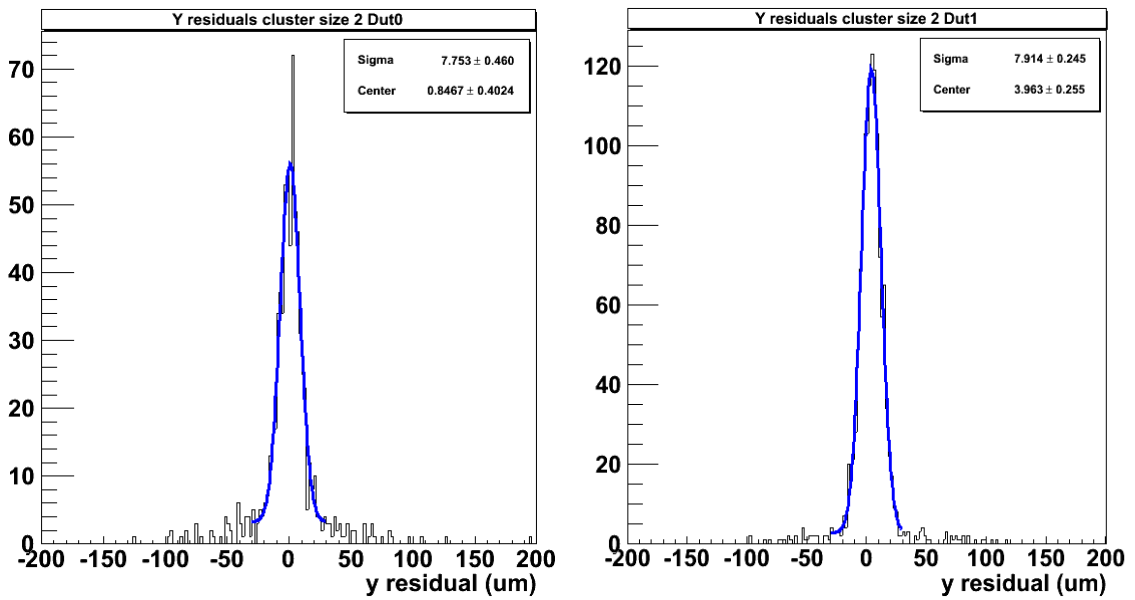


Figure 6.11: Y residual cluster size of 2: Left is 56D (3E) and right is 56B (2E).

Inherent DUT resolution: The telescope extrapolation error is then subtracted in quadrature from the measured DUT resolution to obtain the inherent DUT sensor spatial resolution (σ_{DUT}) using the following equation:

$$\sigma_{DUT} = \sqrt{\sigma_m^2 - \sigma_{TEL}^2}$$

The calculated values of the inherent resolution in x and y direction are shown in the Table 1 below:

Table 1: Resolution for X and Y cluster size 2

| | Resolution for X and Y cluster size 2 | | | | | |
|------------------------------|---------------------------------------|-------------------------------------|----------------|-------------------------|----------------------|-------------------------------|
| | 56D(3E) | | | 56B(2E) | | |
| | Sigma (σ_m) | $\sigma_{Telescope}$ (μm) | σ_{Dut} | Sigma (σ_m) | $\sigma_{Telescope}$ | σ_{Dut} (μm) |
| X residual cluster size 2 | 13.5 | 6.2 | 12.0 | 11.9 | 6.2 | 10.2 |
| Y residual cluster size 2 | 7.8 | 6.2 | 4.4 | 7.9 | 6.2 | 4.9 |

The Y spatial inherent spatial resolution calculated found for 56D(3E) is $4.41 \pm 1.60.4$ μm and for 56B(2E) is $4.91 \pm 1.30.4$ μm . The X inherent spatial resolution calculated for 56D(3E) is 12.0 ± 0.7 μm and for 56B(2E) is 10.9 ± 0.7 μm .

Chapter 7

Conclusions

The thesis work focused on the characterization of 3D silicon pixel sensor prototypes (made by FBK in Italy) designed for the CMS Phase II Tracker Upgrade at the High Luminosity LHC (HL-LHC). The prototype sensors are in two configurations 3E and 2E where 3 or 2 junction columns are joined together and bump bonded to the CMS Phase I Read Out Chip (ROC), the PSI46dig, designed to be bonded to a sensor with the standard geometry of $100 \times 150 \mu\text{m}^2$. The motivation, study and possibility of use 3D sensors for the inner parts of the pixel detector lies in their being radiation hard, shorter drift length, lower operation voltage and higher field for a given bias voltage. The HL-LHC conditions of instantaneous peak luminosities up to $7.5 \times 10^{34} \text{ cm}^{-2} \text{ s}^{-1}$ and an integrated luminosity of the order of $300 \text{ fb}^{-1}/\text{year}$ would result in 1 MeV neutron equivalent fluence of $2.3 \times 10^{16} \text{ n}_{\text{eq}}/\text{cm}^2$ and a total ionizing dose (TID) of 12MGy (1.2 Grad) at the center of CMS, where its innermost component, the Phase-2 Pixel Detector will be installed. The detector should survive the above radiation dose, handle projected hit rates of $3 \text{ GHz}/\text{cm}^2$ at lowest radius, be able to separate and identify particles in extremely dense collision debris, deal with a pileup of 140-200 collisions per bunch crossing and have high impact parameter resolution. This would be key to discover BSM physics that requires increase $|\eta|$ coverage up to 4.0 which improves the Missing Energy (MET) resolution and particle-flow event reconstruction by providing transverse momentum measurements and trajectories for charged particles entering the calorimeters. MET resolution is an essential performance parameter for many BSM physics searches including SUSY and extra dimension models, where particles escape undetected from the detector space. Hence, these detectors (non-irradiated) were carefully calibrated and characterized in a proton beam at the Fermilab Test Beam Facility (FTBF) at Fermilab. The devices under test (DUT) were placed in the middle of a CMS pixel based tracking telescope. A precision alignment of the telescope, with test beam data, was performed using the dedicated software Monicelli, developed by the Milano-Bicocca group. The reconstructed tracks were used to study the detection

efficiency, the charge collection properties and the spatial resolution using a second dedicated software, Chewie. This is the first time that these kind of 3D sensors were studied in a test beam. The detector efficiency is excellent and the Most Probable Values (MPV) of the charge spectra determined are in excellent agreement with the expected values. The sensors have a high signal to noise ratio and excellent spatial resolution making them capable to resolve particle tracks at high pileup. The studies of corresponding irradiated sensors are ongoing. The parameters studied here serve as a reference to the future irradiated sensors studies and as a baseline to compare to in future studies of smaller pixel of sizes $50 \times 50 \mu\text{m}^2$, $100 \times 25 \mu\text{m}^2$ for the design of Phase-2 Pixel Detector.

References

- [1] Nagashima, Y. (2013). *Elementary Particle Physics: Foundations of the Standard Model V2*. Wiley-VCH Verlag GmbH & Co. KGaA, Japan. 646 pp. ISBN: 978-3-527-40966-2
- [2] CMS Collaboration [2012]. Observation of a new boson at a mass of 125 GeV with the CMS experiment at the LHC. *Physics Letters B*. 716 (2012) 30 – 61
- [3] Pillitteri, A. (2017). Fundamental forces and particles. En: Pillitteri, A (ed.). *The Universe Untangled* [online]. Morgan & Claypool Publishers, 40 Oak Drive, San Rafael, CA, 94903 USA. pp. 1-9. ISBN 978-1-6817-4513-8
- [4] Evans L. [2007]. The Large Hadron Collider. *New Journal of physics*. 9 (9), 335-358. DOI: 10.1088/1367-2630/9/9/335
- [5] Baldi, M. (2009). Interactions between Dark Energy and Dark Matter. *der Ludwig-Maximilians-Universität München*. 153 pp. URN: nbn:de:bvb:19-101617
- [6] The Nature of Reality. 2016. *Why Quantize Gravity?*
<http://www.pbs.org/wgbh/nova/blogs/physics/2016/02/why-quantize-gravity/>
- [7] CMS Experiment - <http://cms.web.cern.ch>
- [8] Klioukhine, V. I. et al. 2000. 3D magnetic analysis of the CMS magnet. *IEEE Transactions on Applied Superconductivity*. 10 (1): 428 – 431. DOI: 10.1109/77.828264
- [9] Kim, M. J., Park, H., Kim, H. J. [2016]. Characterization of PbWO₄ crystals for high-energy physics experiments. *Journal of the Korean Physical Society*. 69 (6): 1130 – 1134. <https://doi.org/10.3938/jkps.69.1130>
- [10] Katkov, I., on behalf of the CMS collaboration. [2013]. Characteristics of hadronic interactions in the forward direction. *EDP Sciences, ISVHECRI 2012 – XVII International Symposium on Very High Energy Cosmic Ray Interaction*. 52, 4 pp. <https://doi.org/10.1051/epjconf/20125201003>

- [11] CMS Collaboration. (2010). Commissioning and Performance of the CMS Hadronic Calorimeters in pp Collisions at a Center of Mass Energy of 7 TeV at the Large Hadron Collider. *International conference on high energy physics* 35: 7328-7329. <http://www.ichep2010.fr/>
- [12] Strobbe, N. [2017]. The upgrade of the CMS hadron calorimeter with silicon photomultipliers. *Journal of Instrumentation*. 12 (01): pp. C01080. DOI: 10.1088/1748-0221/12/01/C01080
- [13] CERN, CMS Experiment. (2011). *Hadron Calorimeter*. <http://cms.web.cern.ch/news/hadron-calorimeter>
- [14] Chabert, E. [2015]. b-jet identification at High Level Trigger in CMS. *Journal of Physics: Conference Series*. 608, conference 1: 1-7. doi:10.1088/1742-6596/608/1/012041
- [15] Malik, S. [2006]. The CMS Forward Pixel Detector. CERN Document Server. *Nuclear Instrument Methods Physics Research*. A572: 87 – 89. DOI: 10.1016/j.nima.2006.10.278
- [16] Kästli, H. C. (2006). Design and performance of the CMS pixel detector readout chip. *Nuclear Instruments and Methods*. 565 (1): 188 – 194. <https://doi.org/10.1016/j.nima.2006.05.038>
- [17] Bileia, G. M. et al. [1998]. The CMS silicon tracker at LHC. *Nuclear Instruments and Methods*. 409 (1 -3): 105 -111. [https://doi.org/10.1016/S0168-9002\(97\)01247-3](https://doi.org/10.1016/S0168-9002(97)01247-3)
- [18] CMS Collaboration. *CMS Technical Design Report for the Pixel Detector Upgrade*. <https://cds.cern.ch/record/1481838>
- [19] Wikipedia: The free encyclopedia. (2017). *Top quark*. https://en.wikipedia.org/wiki/Top_quark
- [20] Heavy Ion Physics Lab. (2017). *Electroweak bosons*. <http://www.weizmann.ac.il/particle/atlas/research-activities/electroweak-bosons>

- [21] STAR Collaboration. et al. [2005]. Experimental and theoretical challenges in the search for the quark–gluon plasma: The STAR Collaboration's critical assessment of the evidence from RHIC collisions. *Nuclear Physics A*. 757 (1-2): 102-183. <https://doi.org/10.1016/j.nuclphysa.2005.03.085>
- [22] Moreira, P. (2015). *The LpGBT Project*. <http://slideplayer.com/slide/9319741/>
- [23] Meschin, M. et al. [2016]. The INFN-FBK pixel R&D program for HL-LHC. *Nuclear Instruments and Methods*. 831: 116 – 121. <https://doi.org/10.1016/j.nima.2016.05.009>
- [24] Dalla Beta, G.-F. et al. [2016]. Development of a new generation of 3D pixel sensors for HL-LHC. *Nuclear Instruments and Methods*. 824: 386 – 387. <https://doi.org/10.1016/j.nima.2015.08.032>
- [25] El-Kareh B., Hutter L.N. (2015). Review of Single-Crystal Silicon Properties. En: El-Kareh, B., Hutter, L. N (eds.). *Silicon Analog Components* [online]. Springer, New York, NY, pp. 25 -63. ISBN 978-1-4939-2751-7
- [26] ENEE 313, Spring 2009. *Supplement 1 on carriers, the Fermi level and density of states*. http://www.ece.umd.edu/~dilli/courses/enee313_spr09/
- [27] Srinivasan, G. (2014). Fermi–Dirac Distribution. En: Srinivasan, G (ed.). *Life and Death of the Stars* [online]. Springer, Berlin, Heidelberg, pp. 55 – 66. ISBN 978-3-642-45384-7
- [28] Crank, J. (1975). *The Mathematics of Diffusion*. Copyrighted Material, Oxford University Press, 401 pp. ISBN 0 19 853344 6
- [29] Wikipedia: The free encyclopedia. (2017). *The Poisson's Equation*. https://en.wikipedia.org/wiki/Poisson%27s_equation
- [30] PV EDUCATION.ORG. (2017). *General Properties of Silicon*. <http://www.pveducation.org/pvc/drom/materials/general-properties-of-silicon>
- [31] Sakurai, J. J. (1994). *Modern Quantum Mechanics*. Addison-Wesley Publishing Company, Late, University of California, Los Angeles. 513 pp. ISBN-13: 978-0201539295

- [32] Groom, D. E., and Klein, S. R. [2000]. Passage of particles through matter. En: Groom, D. E., and Klein, S. R (eds.). *The European Physical Journal C* [online]. Springer Berlin Heidelberg, pp. 163 – 173. <https://doi.org/10.1007/BF02683419>
- [33] Stache, J. (2015). *Detectors in Nuclear and Particle Physics*. Department of Physics und Astronomy University of Heidelberg, 98 pp.
- [34] Aspell, P. et al. (2009). “VFAT2: A front-end system on chip providing fast trigger information, digitized data storage and formatting for the charge sensitive readout of multi-channelsilicon and gas particle detectors.” White *Nuclear Science Symposium Conference Record*, 19-25 Oct. 2008, Dresden, Germany, Germany, 6 pp. DOI: 10.1109/NSSMIC.2008.4774696
- [35] Wikipedia: The free encyclopedia. (2017). *Phosphorus*. <https://en.wikipedia.org/wiki/Phosphorus>
- [36] Turqueti, M. [2009]. “CAPTAN: A Hardware Architecture for Integrated Data Acquisition, Control, and Analysis for Detector Development.” White *Nuclear Science Symposium Conference Record*, 19-25 Oct. 2008, 7 pp. DOI: 10.1109/NSSMIC.2008.4775101
- [37] Kwan, S. [2014]. The pixel tracking telescope at the Fermilab Test Beam Facility. *Nuclear Instrumentation and Methods*. A811: 162 -169. DOI: 10.1016/j.nima.2015.12.003
- [38] Zoi. I. (2016). *Silicon pixel detectors for the CMS Tracker upgrade at HL-LHC*. Thesis M.S. Università Degli Studi Firenze, 138 pp.